The chemical evolution of galaxies and nuclear clusters - a synergetic view from cosmological numerical simulations and analytical models

by

Andrew Crombie Mason

A thesis submitted in partial fulfillment of the requirements of
Liverpool John Moores University
for the degree of
Doctor of Philosophy

February 2025

Declaration

The work presented in this thesis was carried out at the Astrophysics Research Institute, Liverpool John Moores University. Unless otherwise stated, it is the original work of the author.

While registered as a candidate for the degree of Doctor of Philosophy, for which submission is now made, the author has not been registered as a candidate for any other award. This thesis has not been submitted in whole, or in part, for any other degree.

Andrew Crombie Mason
Astrophysics Research Institute
Liverpool John Moores University
146 Brownlow Hill
Liverpool
L3 5RF
UK

February 2025

Abstract

Over the past century, grand strides in methods and instrumentation have allowed us to observe the Universe – especially our Local Group of galaxies – in exquisite detail such that we can constrain the assembly of these galaxies by the study of their chemical compositions. Using sophisticated simulations of galaxy formation and evolution, we can also assess how representative the Local Group is today of other systems at $z = 0$. This thesis aims to assess the connection between the assembly of galaxies and star clusters, and the chemical compositions of their stellar populations, using a combination of observational datasets, cosmological numerical simulations, and analytical models of galaxy chemical evolution.

This thesis provides a new interpretation of the formation of the so-called 'α-Fe knee' in nearby galaxies, a feature on the α-Fe planes of galaxies that is thought to arise due to the onset of SN Ia contributing Fe to the ISM. I perform an analysis of the α-abundance patterns of galaxies populating a high-resolution realisation of the EAGLE cosmological numerical simulations. I focus on the cosmic evolution of the abundance ratio [α/Fe] as a function of [Fe/H], with a view to constraining: *i)* the origin by which the α-knee forms in simulated galaxies, *ii)* why the stellar populations of some observed galaxies do not display this feature on the α-Fe plane, and *iii)* if there is a tight scaling relation between stellar mass and the metallicity of the α-knee, as well as what drives the scatter in this relation.

I demonstrate that EAGLE predicts a diversity of possible distributions of stellar particles on the α-Fe plane in simulated galaxies, much like we see in the Local Group. We compare and contrast galaxies that exhibit no α-knee ('single slopes') on the α-Fe plane and those that do ('classical knees'), finding that the former are characterised by

extended histories of roughly constant star formation. The latter exhibit sharp declines in their SFRs after an earlier rise, which is coincident with the formation of the α-knee. This is because a sharp decline in the SFR causes a prompt decrease in enrichment by SN II, leaving the SN Ia from antecedent star formation episodes to dominate the Fe-enrichment. Since single sloped galaxies do not experience a similar drop in star formation, they exhibit gently declining distributions of [α/Fe] vs. [Fe/H] over the whole range of [Fe/H] with no change in slope.

I further demonstrate that the scaling relation between the stellar mass of a galaxy and the metallicity of the α-knee in the simulations is similar to that observed in the Local Group dwarf galaxies, including its scatter. Our analysis shows that the scatter in this relation is caused by variation in the amount of star formation taking place before the peak of the star formation history. As a result, galaxies with low $[\mathrm{Fe/H}]_{\mathrm{knee}}$ at fixed $M_\star$ formed less massive plateaus before the decline in the SFR, and vice versa.

Finally, I compare the typical assumptions of one-zone GCE models regarding the treatment of the star formation efficiency to what is seen in the EAGLE simulations. I find that the star formation efficiency in EAGLE galaxies vary, by an order of magnitude (from low to high) as a function of cosmic time in knees. That is in stark contrast to the constant star formation efficiency typically involved in one-zone GCE models, an assumption which implies the presence of a readily-enriched, low-mass gas reservoir. Instead, the mixing mass in EAGLE galaxies tends to be much higher, and thus SN Ia can still make significant contribution to the enrichment of the plateau. A decline in the star formation rate produces a clear α-knee, consequently.

In the second half of the thesis, I performed a detailed chemical study of the complex Galactic stellar system ω Centauri, a system suspected to be the accreted nuclear star cluster of a dSph galaxy that underwent a merger with the Milky Way at an earlier cosmic epoch. We identified three distict populations in the cluster, which are labelled P1, P2, and IM (for intermediate). We find that the P1 population exhibits field-like abundance patterns, whereas P2 and IM are characterised by the chemical abundance anomalies typical of poulations seen in other Galactic globular clusters.

Using complementary photometric data derived from HST observations, we show that the complexity of the distribution of ω Cen stars in the so-called 'chromosome map' is accounted for by the range of light-element abundances covered by the P1, P2, and IM populations as well as the chemical evolution of P1 and P2. We further hypothesise that the IM population resulted from the inspiral of GCs from ω Cen's progenitor galaxy, which may also have deposited gas in the centre off the cluster. The subsequent star formation episode may then have formed the P2 population, which may also have experienced significant loss of gas or stars during this episode.

The above outlines a new interpretation of the abundance patterns of the Local Group dwarfs and their histories of star formation, as well as a prediction for what could be a useful scaling relation for galaxies in the Local Group. Furthermore, the hypothetical scenario to explain the abundance patterns of ω Cen is one well-motivated by the likely nature of the cluster as a nuclear star cluster (NSC).

Contents

List of Figures

Publications

During the course of the preparation of this thesis, the work with in chapters 2 and 3 originates from the following jointly authored publications, one in-prep:

1. '*Realistic simulated galaxies form [α/Fe]-[Fe/H] knees due to a sustained decline in their star formation rates*' **Mason, Andrew C.**, Crain, Robert A., Schiavon, Ricardo P., Weinberg, David H., Pfeffer, Joel, Schaye, Joop, Schaller, Matthieu, Theuns, Tom, 2024, MNRAS 533, pp184-200

2. *'Chemical tagging with APOGEE, MUSE, and HST: constraints on the formation of ω Centauri'* **Mason, Andrew C.**, Schiavon, Ricardo P., Kamann, Sebastian, *in-prep*

Publication 1 forms the basis of Chapter 2. The high-resolution EAGLE simulations (Schaye et al., 2015; Crain et al., 2015) used in that chapter were presented in Bastian et al. (2020). All analysis and interpretation of the simulations, observational data, and chemical modelling was carried out by A. C. Mason, with input from R. A. Crain, R. P. Schiavon, D. H. Weinberg, J. Pfeffer, J. Schaye, and T. Theuns. The merger trees used in the analysis were produced by J. Pfeffer for use in the analysis. The manuscript was prepared by A. C. Mason, with additions and alterations made following from co-authors, colleagues and the anonymous referee.

Publication 2 forms the basis of Chapter 3, and comprises a thorough analysis of the abundance patterns of the Galactic stellar system ω Centauri. All data analysis and interpretation was carried out by A. C. Mason, with significant intellectual input from R.P. Schiavon and S. Kamann.

Acknowledgements

A huge amount of thanks go to my supervisors, Ricardo and Rob. Ricardo - it's been an absolute pleasure to work with you, from the beginning to the end. I cherish both your mentorship as a supervisor, and the friendship we've developed over the years. Your capabilities as a barbecue chef also bear some comment here, the Picanha you prepared was apotheotic. I am extremely grateful to your efforts, and proud of the work we've done. Rob - I have great admiration for your approach to the work we do at ARI, and your contributions have been immense over the years. Thank you both for being so supportive; it's a testament to this that the work we thought from the outset was going to severely upset some people has been met by some pretty glowing praise. I would also like to heartily thank Sebastian Kamann and Sara Saracino for your friendship and guidance over the course of the project - it's also been great to get you involved with the work concerning ω Cen, and I hope that continues. I'd also like to warmly thank Daisuke Kawata and Andreea Font, who examined this thesis and enabled the viva into an enjoyable and gratifying experienced. Your helpful comments and corrections improved the thesis, and the discussions we had on the day of the viva and after the fact have opened up some intriguing avenues to explore in future work - thank you!

To my colleagues in our little Milky Way working group, it's been a blast. Danny - you've always got great advice and interesting things to say, and I thank you very much for your support, especially during the 'postdoc application phase' of my PhD. Shobhit, my PhD brother, thanks a ton for your support and friendship, especially during the darkest days of the pandemic. We need to get back on the courts and hit those massive forehands again. Michael and Anna - it's been great to see you guys settle into the groove with the group, and I wish you the very best in your future research.

I'd also like to thank my new colleagues at the ISMIB at the University of Liverpool - thanks to Reecha for giving me the opportunity to try my hand at a new project in health data science as part of my CDT adventure and being an incredibly supportive voice throughout, especially as I was wrapping up my PhD. A huge thanks also to Vicky, Caroline, Ana, Pardis, Francesca, Rohan, and Nasri.

To my collaborators, I would like to also give great thanks to folks from APOGEE, the EAGLE team, and invaluable collaborators we made contact with at various conferences. Among these, individual thanks are due to David Weinberg, Joel Pfeffer, Joop Schaye, Matthieu Schaller, and Tom Theuns.

To the 3.18 gang, the *esprit de corps* we have developed has been nothing short of wonderful. Tuts, Flo, Phoebe, Jemima, Sarah, Shobhit, Bethan, Adrian, Elena, Sara, and Kyle - it was a steady trickle of people after the lockdown ended, but it's been an absolute joy to get to know you all whether we were collaborating, confiding in one another, laughing at terrible jokes, and dominating at the pub quiz. It was a truly miserable experience working on this project during the extended lockdown we endured in 2020-21. However, it is always darkest before the dawn, and we did eventually emerge from the lockdown. Getting to share this experience with you guys was sweeter and more glorious than any sunrise.

I would be remiss if I didn't give a further heartfelt thanks to Tuts and Thayse, for being amazing friends and helping me out massively when I was between houses. I certainly wouldn't have made it without your support during that difficult period, and I can't thank you enough for your generosity. Special thanks to Shobhit, Ali, and Harris for helping me move.

Writing this, I have no idea how I'm not going to be reduced to a blubbering mess when it comes to the viva. I'm honoured to have gotten to know everyone at ARI, and I will miss you all dearly. Thank you, again.

ACM is supported by an STFC doctoral studentship within the Liverpool Centre for Doctoral Training for Innovation in Data Intensive Science (LIV.INNO), hosted by

Liverpool John Moores University and the University of Liverpool. Analyses and plots presented in this thesis used IPYTHON and packages in the SCIPY ecosystem (Virtanen et al., 2020; Hunter, 2007; Perez & Granger, 2007; Seabold & Perktold, 2010; van der Walt et al., 2011). The production of the thesis made use of the Prospero high-performance computing facility at Liverpool John Moores University, and the DiRAC Data Centric system at Durham University, operated by the Institute for Computational Cosmology on behalf of the STFC DiRAC HPC Facility (`http://www.dirac.ac.uk/`).

In dark times, should the stars also go out?

Steban, *Disco Elysium*

Chapter 1

Introduction: Scientific Background

The story so far: in the beginning, the Universe was created. This has made a lot of people very angry, and been widely regarded as a bad move.

Douglas Adams

1.1 Preamble

Over the past two centuries, Galactic astronomy has undergone an evolution from a hobby enjoyed by a handful of 'gentleman astronomers' charting the skies to a vibrant field which has produced a fairly comprehensive picture about the formation of the Universe that we see today. Where once observations of the night's sky were seen as a glimpse of the divine, we now understand the position we occupy within a solidly based cosmological paradigm built on a Herculean effort by the community over the course of decades. We now understand that we reside in one of hundreds of billions of galaxies, which formed in a Universe whose mass-energy budget is dominated by dark energy, dark matter, and the baryons that comprise its visible components. The structure of the observable universe is of course traced by its galaxies which comprise gas and stars embedded in dark matter haloes. We now have a solid theoretical understanding that explains the present-day configuration of the Universe in terms of the complex interplay of gravity and electromagnetic radiation. This framework serves as a stepping stone to constraining assembly history of the Galaxy by studying its configuration down to the level of individual stars.

Though it ultimately finds its genesis during the 1960s (Eggen et al., 1962), in recent years a subfield of astronomy has been gaining momentum thanks to a combination of advances in hardware and computing. Galactic (big 'g') archaeology deals with constraining the assembly history of *the* Galaxy by the study of its gas and stellar populations, in the aforementioned cosmological context. We have data for millions of stars in the Milky Way and its satellites thanks to the ongoing era of massive astrometric, photometric, and spectroscopic surveys such as *Gaia* and APOGEE, allowing a truly granular view of the Galaxy and its constituent stellar populations both *in-situ* and *ex-situ*.

Hugely complementary to these efforts, continual advances in high performance computing have enabled astronomers to construct simulations of the co-evolution of dark matter (abbreviated in parts of this thesis as DM) and baryons, modelling galaxy formation and evolution to answer a variety of questions. 'Zoom-in simulations' reveal, at very high resolution, the detailed assembly of galaxies down to the smallest building blocks that can be feasibly resolved. Meanwhile, cosmological volumes, which we shall be focusing on in Chapter 2 offer a representative glimpse of structure formation on Mpc scales, while also featuring the same sophisticated prescriptions for physical processes such as star formation, stellar & AGN feedback, and chemical enrichment. Both methods

have allowed observations of Local Group galaxies to be placed in their cosmological context, as the simulations have the potential to tell us how representative our Galaxy and its neighbours are compared to the galaxy population at large. Furthermore, they shed light on the assembly histories and physical mechanisms that lead to the present-day configuration of the Local Group in terms of the structural parameters of its galaxies and the chemical compositions of their stars.

This further dovetails with the burgeoning field of 'Local Volume archaeology'. Its aim is to push the observational envelope beyond the virial radius of the Milky Way, and out to the edges of the Local Group. With the launch of the James Webb Space Telescope (JWST), and the promise of more advanced instrumentation and telescopes in the future, soon we will be able to probe the fossil records of more of the massive nearby galaxies such as M31 and M33.

The focus of the this thesis is how the chemical abundances of individual stars comprising galaxies directly trace their host's assembly history. Thus, we present:

1. A reinterpretation of the α-abundance patterns of Local Group galaxies, from the Milky Way to the Large Magellanic Cloud (LMC) using the EAGLE simulations and numerical models of galaxy chemical evolution.
2. A thorough exploration of properties of the Galactic stellar cluster ω Centauri using the latest data from the cluster itself and the Milky Way.

This introductory chapter will give a brief accounting of the current theoretical and observational state of play, with a focus on recent results that have arisen due to the efforts of Galactic archaeologists, and how they have revealed crucial details about the assembly history of both our own Galaxy, and its neighbours.

1.2 The Galaxy Population at Large

The Λ-cold dark matter model ('ΛCDM') (White & Rees, 1978) is regarded as the standard model of cosmology due to its high predictive success. In this model large scale cosmic structure, including galaxies, is seeded by primordial density fluctuations in the

Table 1.1: Cosmological parameters according to a *Planck* cosmology (from Planck Collaboration et al., 2016)

Parameter	Value
Ω_m	0.3156
Ω_Λ	0.6844
Ω_b	0.04927
σ_8	0.831
n_s	0.9645

early universe, after a rapid period of inflation shortly after the Big Bang (Guth, 1981). Major accomplishments of the model include strong agreement with modern measurements of the cosmic microwave background (CMB) fluctuations at high redshift from the measurements of *WMAP* (see Dunkley et al., 2009, and references therein), the subsequent *Planck* (Planck Collaboration et al., 2014, 2020a) observations of the temperature and polarization anisotropies of the CMB radiation, and derived measurements of cosmological parameters. In general, modern treatments of a ΛCDM cosmology will call for a *Planck* cosmology with a Hubble parameter of $h = H_0/(100\ \mathrm{kms^{-1}Mpc^{-1}}) = 0.6727$ and cosmological parameters given by Table 1.1. Ω refers to the fraction of the energy density occupied by baryons (Ω_b), matter (Ω_m), and dark energy (Ω_Λ). σ_8 refers to the matter density fluctuations at a distance scale of $8h^{-1}Mpc$, where h is the Hubble constant at $z = 0$ ($h = H_0/(100\ kms^{-1}Mpc^{-1})$). Simply put, σ_8 measures the amplitude of the clustering of matter (in this context, directly measured from fluctuations in the CMB). n_s refers to the scalar index of density fluctuations. The measured value of $n_s < 1$ indicates a 'red-tilted' matter power spectrum, such that the amplitudes of primordial fluctuations are higher at larger characteristic scales and agrees with the inflationary paradigm (Mo et al., 2010).

A major implication of ΛCDM is that the assembly of galaxies happened hierarchically. This is to say that the DM haloes, formed by the infall of dark matter into primordial density fluctuations being stretched to larger scales by the inflation of the early universe, grew by the accretion of smaller haloes. We also can only infer the presence of dark matter from its gravitational interactions with luminous baryonic matter. Thus, currently the study of the baryonic content of galaxies is therefore the only means by which we can trace the history of interaction between DM halos, as it may bear some imprint of halo assembly.

In this vein, Willman & Strader (2012) succinctly defined a galaxy as thus:

> *...a galaxy is a gravitationally bound collection of stars whose properties cannot be explained by a combination of baryons and Newton's laws of gravity.*

The volumetric number density of galaxies per unit stellar mass ($M_\star$) as a function of stellar mass defines what is known as the galaxy stellar mass function (GSMF) (see the results of the Galaxies and Mass Assembly survey, GAMA Baldry et al., 2008). A fundamental prediction of the ΛCDM cosmogony is that the number density of galaxies should increase steeply with decreasing $M_\star$ at $z = 0$ (e.g. White & Rees, 1978). Across the range of stellar masses that defines galaxies, they can broadly be segregated into so-called dwarfs and massive galaxies, respectively. The former span a mass range $M_\star \simeq 10^3 - 10^9$ $M_\odot$ while the latter have $M_\star \geq 10^9 M_\odot$. Furthermore, there is a characteristic mass at which the GSMF turns over precipitously, M^*, which defines another subset of the galaxy population at large - massive galaxies that tend to host active galactic nuclei (AGNs Matthee et al., 2017). Additionally, the volumetric number density of galaxies per unit *luminosity* (L) as a function of luminosity defines the galaxy luminosity function (GLF) (Schechter, 1976). The characteristic turnover luminosity is denoted as L^*.

Across the range of masses galaxies can have, there is great morphological diversity at fixed $M_\star$. Historically, massive galaxies have been classified as being elliptical (E), disks (S) or somewhere between these two morphologies (S0). Elliptical galaxies are superficially featureless (in the optical), possessing minimal visible gas, and their surface brightness profiles generally follow the so-called de Vaucouleurs profile (de Vaucouleurs, 1948). Disk galaxies tend to feature prominent spiral arms, clear evidence of ongoing star formation (HII regions) and have surface brightness profiles which tend to exponentially decline as a function of projected radius.

Fig. 1.1 shows the 'Hubble sequence' (Hubble, 1936), a traditional *qualitative* scheme of classifying galaxies. Images are derived from the DSS2 survey. Otherwise referred to as the 'tuning fork', the handle comprises elliptical and lenticular galaxies (E0-S0) and the prongs unbarred (Sa-Sc) and barred spiral galaxies (SBa-SBc). It was once thought that the sequence could represent the evolution of galaxies with cosmic time, with elliptical galaxies referred to by some as 'early type' galaxies, due to early observational work concluding that their chemical abundances were consistent with early bursts of star formation and subsequent quenching at early cosmic epochs. Just as with the spiral

galaxies, however, elliptical galaxies also exhibit significant diversity (Kormendy et al., 2009).

Furthermore, the sequence itself is constructed in such a way that it does not represent a continuous evolution of galaxy structural parameters (see Kormendy & Bender, 1996; Kennicutt, 1998a, for historical discussion on this subject). Nontheless, it gives a decent *qualitative* classification of the massive galaxy population at large.

Entering the regime of the dwarf galaxies, the diversity increases. Broadly speaking, dwarfs were historically categorised as being either *irregular* (dIrr) or *spheroidal* (dSph). dIrrs, such as the Small Magellanic Cloud (SMC), generally have high gas fractions at $z = 0$ and ongoing star formation. dSphs are thought to have minimal gas fractions and show no evidence of ongoing star formation. Furthermore, dSphs occupying the low-luminosity end of the GLF can be categorised as being 'ultra-faint'. Galaxies with middling gas fractions and decreasing star formation rates are thought to be transitory between dIrr and dSph and are thus categorised as dTrans (Grebel, 2001). Finally, there are the ultra-compact dwarfs (UCDs) which have characteristically high stellar densities confined to very small radii. While these aforementioned categories are endemic to the dwarf population, there are also dwarfs that can be placed on the Hubble sequence such as the dwarf ellipticals (dE) and dwarf spirals (dS).

It was once thought that dwarfs could be easily distinguished from their more massive counterparts on the basis of their physical parameters, in particular their luminosity and size. As pointed out by Tolstoy et al. (2009), classifying galaxies according to morphology *must* incorporate a physical understanding of the processes that led them to manifest in the first place. Weisz et al. (2011) and Weisz et al. (2014) also demonstrated that at fixed $M_\star$ and within the same morphological class, dwarfs have heterogeneous histories of star formation. How these differences relate to their assembly histories and manifest in their chemical evolution are critical albeit unanswered questions in the literature - it is very difficult to measure chemical compositions of stars at such low metallicity as in the regime of dwarf galaxies.

The excellent review of Bullock & Boylan-Kolchin (2017) adopts a straightforward dwarf classification: *bright dwarfs* which have stellar masses $10^7\ \mathrm{M}_\odot < M_\star < 10^9\ \mathrm{M}_\odot$, *classical dwarfs* which have stellar masses $10^5\ \mathrm{M}_\odot < M_\star < 10^7\ \mathrm{M}_\odot$, and *ultra-faint dwarfs* which have $10^2\ \mathrm{M}_\odot < M_\star < 10^5\ \mathrm{M}_\odot$. As pointed out in the review of Mateo (1998), the Local Group currently provides one of the most complete and representative sample of dwarf galaxies at $z = 0$. Thus, in following sections of this chapter, description

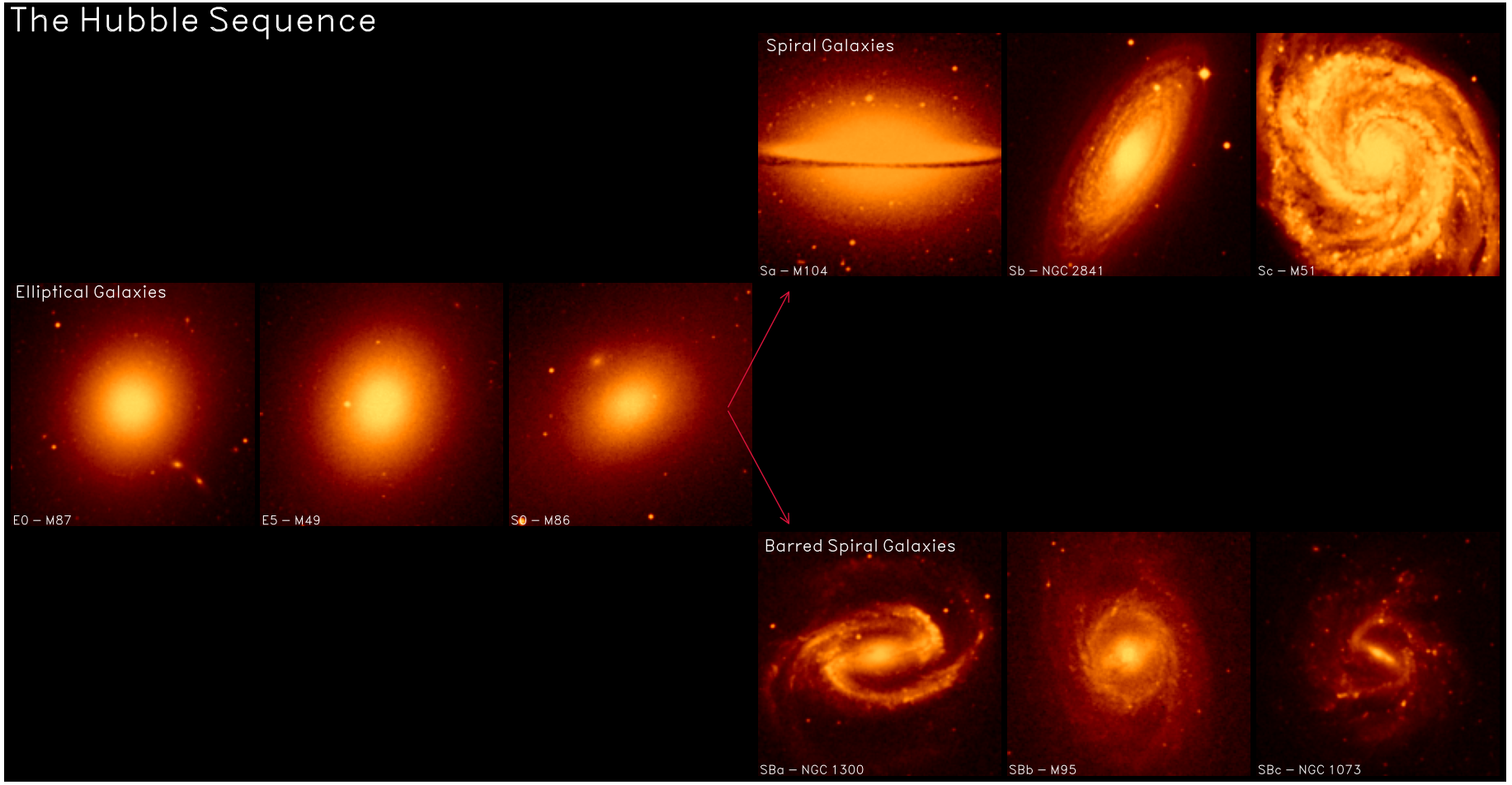

Figure 1.1: Digitised Sky Survey 2 (DSS2) images showing the Hubble morphological sequence, spanning from elliptical galaxies (E0-S0), and splitting at spiral galaxies (S) and barred spiral galaxies (SB). Data are taken from

of the observational state of play will lean heavily towards studies of the Local Group Dwarfs (LGDs) and the Galaxy itself.

With this broad accounting of the galaxy population by mass concluded, we now move on to describe what the chemical compositions of galaxies - their stars and gas - can tell us about their assembly histories.

1.2.1 Star Formation across Cosmic Time, the Baryon Cycle and Galaxy Chemical Evolution

One of the most important determining factors for the compositions of the stars and gas in a galaxy is its history of star formation. In this section, we describe briefly how the regulation of star formation in the interstellar medium of galaxies over cosmic time has affected the galaxy population at large in a process known as the 'baryon cycle'. It is thought that Big Bang nucleosynthesis imprinted a so-called 'primordial' chemical composition upon all the gas in the Universe, characterised by a helium abundance of $Y \simeq 0.248$ (Planck Collaboration et al., 2016). The abundance of elements heavier than He defines the 'metallicity' of a galaxy. Measurements of the metallicities of galaxies alone, in the context of other properties such as mass and star formation rate, encode a wealth of information about their evolution and the processes that drive them.

The electromagnetic spectrum of a galaxy measures the flux originating from its gas and stars, at a given wavelength interval. Limiting the wavelength range to that dominated by young, massive stars ($\lambda = 912 - 2000$Å), it is possible to directly measure the star formation rates and chemical composition of galaxies by relating the flux originating from nascent stellar populations to the overall rate of star formation. The plot of the global co-moving star formation rate density as a function of cosmic time is referred to as the 'Madau plot' (or Lilly-Madau plot, after Lilly et al., 1996; Madau et al., 1996). It tells us that after the epoch of reionisation, the cosmic star formation rate density (SFRD) increased steadily until it peaked at a value of $\sim \log_{10}(\dot{\rho}_\star) = -1$ $M_\odot yr^{-1}Mpc^{-3}$ at $z \simeq 2$, before declining an order of magnitude until today, $z = 0$. This also implies that a vast amount of the metal production in the universe took place around $z \simeq 2$, coinciding with the peak of the SFRD.

Measurements of the ages and stellar metallicities of galaxies as a function of cosmic time place fundamental constraints on the star formation and chemical evolution histories of the universe. Using a sample of Sloan Digital Sky Survey (SDSS) observations

of galaxies in the Local Universe, Gallazzi et al. (2005) directly measured the age-metallicity (AMR) and mass-metallicity (MZR) relations for galaxies populating the GSMF between $10^9 < M_\star\ [\mathrm{M}_\odot] < 10^{12}$. Using the gas-phase oxygen abundance as a tracer of the overall metallicity of these galaxies, they measured a tight (0.1 dex at fixed $M_\star$) mass-metallicity relation for a sample of $z = 0.1$ galaxies. Crucially, as the masses of these galaxies spanned 3 orders of magnitude, this measurement of the MZR encompassed the bright dwarfs as well as the most massive galaxies. Larson (1974) had predicted that the interplay between supernova feedback and galaxy mass would have a significant impact on the shape of the MZR. This is because galaxies with lower masses are less able to retain supernova ejecta in the wake of these explosions due to having shallower potential wells, meaning the ejecta of supernovae ($v_{\mathrm{ej}} \simeq 500\ \mathrm{kms}^{-1}$) can easily exceed the escape velocity of dwarf galaxies (Mac Low & Ferrara, 1999). The measurement of the MZR directly traces this phenomenon - galaxies with lower masses are characterised by lower metallicities as they are less able to retain the ejecta from SNe explosions and incorporate it into successive stellar generations.

The shape of the MZR, as well as its evolution with cosmic time, are now well constrained (Tremonti et al., 2004), and place fundamental constraints on galaxy chemical evolution (referred to hereafter as 'GCE'). There is also the existence of a so-called 'fundamental metallicity relation' (FMR) - which manifests itself at fixed $M_\star$ as an apparent anti-correlation between the SFR and metallicity of galaxies (Mannucci et al., 2010; Bothwell et al., 2013; Salim et al., 2014; Curti et al., 2020). Observations of galaxies and cosmological simulations suggest that the FMR may be driven by ongoing gas accretion (Kacprzak et al., 2016; De Rossi et al., 2017).

The star formation rates of galaxies as a function of cosmic time (the star formation history, SFH) can also be measured by matching observed and synthetic colour magnitude diagrams (CMDs) using stellar evolution codes (a practise originating in the 1990s, from pioneering work by such authors as Tosi et al., 1991; Bertelli et al., 1992). Well-constrained SFHs place huge constraints on predictions for the run of the abundances of various elements as a function of cosmic time provided by galaxy chemical evolution models.

1.3 Stellar nucleosynthesis as a tracer of galaxy formation and evolution

In this section, we discuss another fundamental component of GCE modelling - stellar nucleosynthesis, and the predicted yields of individual elemental species from the canonical nucleosynthetic channels (SN II, SN Ia, and asymptotic giant branch stars). To preface this discussion, when discussing the abundance patterns of Local Group galaxies in the context of Galactic archaeology we adopt the conventional definitions of logarithmic abundance ratios, where the abundance of a given element X is expressed in terms of its ratio to the overall metallicity, relative to that of the Sun. Metallicity is oftentimes traced by the abundance ratio [Fe/H], which has advantages and disadvantages. While Fe lines are easy to measure in stellar spectra, Fe also has multiple nucleosynthetic channels that release it into the interstellar medium (ISM hereafter; SN II, SN Ia, and marginal contribution by asymptotic giant branch, or AGB, stars). The logarithmic abundance is defined such that:

$$[X/Fe] = \log_{10}\left(\frac{n^X}{n^{Fe}}\right) - log_{10}\left(\frac{N_\odot^X}{N_\odot^{Fe}}\right), \tag{1.1}$$

where where n^X denotes the number of atoms of an element X, n^{Fe} denotes the number of atoms of Fe, and $N_\odot^X$ denotes the number of atoms of a given element X of the Sun (the measurements of Asplund et al., 2009 are perhaps the most widely adopted in contemporaneous literature).

In this section, we give a broad overview over the various nucleosynthetic channels that give rise to the abundance patterns seen in the individual stars comprising nearby galaxies. We describe the production of various species within the interiors of stars of different masses and how this varies as a function of overall metallicity as well as the observational state of play prior to the release of *Gaia* data and their combined use with chemical abundance data from massive spectroscopic surveys.

We have established how, via spectroscopy, it is possible to measure the chemical abundances of distant galaxies down to partially resolved scales. Similarly, we can perform spectroscopy on *individual* stars comprising the Local Group galaxies, from *the* Galaxy to its satellites. With a large enough sample of stars, at different metallicities, the chemical compositions of these stars trace the chemical enrichment history of their host galaxies. This is because evolved stars retain the abundance pattern of the gas that

birthed them, and thus the abundances of different species with respect to the overall metallicity traces which progenitors were contributing to the chemical enrichment of individual galaxies as a function of cosmic time.

Generally, the most significant degree of chemical enrichment originates from three main sources, listed below:

Polluters of the ISM and their progenitors

1. Low through intermediate-massed stars ($M_{\star,i} \simeq 0.8 - 8\mathrm{M}_{\odot}$) which, during the asymptotic giant branch (AGB) phase of their stellar evolution, enrich the interstellar medium with material processed by hydrogen and helium burning deep within the star, as well as the neutron capture elements produced by the s-process. At the interface of stellar masses between 'intermediate' and 'high' (usually considered to be the lower limit at which point a star is sufficiently massive to explode as a Type II supernova) there are the so-called 'super AGB' stars.

2. Massive stars ($M_{\star,i} \gtrsim 8\ M_{\odot}$) which are affected by very strong winds over the course of their evolution, ejecting via stellar winds material enriched by hydrogen and helium burning products characteristic of various high temperature processes ($T > 10^6 K$). At the culmination of their evolution, they explode as Type II supernovae (SN II hereafter[1]), which both ejects enriched material from the stellar interior and causes so-called explosive nucleosynthesis.

3. Type Ia supernovae (SN Ia; $M_{\star,i} < 8\ M_{\odot}$) do not occur as a result of 'standard' stellar evolution. Their progenitors are white dwarf (WD) stars which gain sufficient mass to exceed the Chandrasekhar limit, which induces core collapse and a subsequent explosion. There are two popular scenarios for a WD star to accrete enough mass to explode as a Type Ia supernova: single-degenerate and double degenerate models. In the former, a binary system's primary star evolves to become a WD and begins to accrete matter from the secondary star until sufficiently massive to undergo core collapse. In the latter, two white dwarfs in a binary system inspiral and merge which facilitates the core collapse.

All of the elements on the periodic table with mass number A from 12 to 60 form in stellar interiors during quiescent nuclear burning over the course of their stellar

evolution. Across all masses, nucleosynthesis during this phase is initially characterised by the fusion of H into He, and subsequently He into heavier species (up to the Fe-peak elements in massive stars). He is synthesisesd either by proton-proton chain burning, or the CNO cycle depending on the progenitor's stellar mass. At yet higher core temperatures ($T > 10^8$ K), the triple-α reaction transforms ^{4}He to ^{12}C. More advanced He-burning reactions involving O, Ne, and Mg (Pagel, 2009) can take place in layers with $T > 10^9$K.

Elements heavier than ^{12}C are produced by the synthesis of α-particles, and thus dubbed the α-elements (O, Ne, Mg, Si, S, and Ca). The highest temperature reaction in stellar interiors is ^{28}Si burning, which produces the radioactive isotope ^{56}Ni, forming Co and Fe by β-decay.

Finally, there are the *r* and *s*-process elements (A>60). These form by the *r* (rapid) or *s* (slow) neutron capture by heavy seed nuclei, depending on the site. The *s*-process elements form during quiescent He burning, whereas the *r*-process elements form during explosive nucleosynthesis which occurs during SN II explosions.

Fig. 1.2 shows the periodic table of the elements presented in Weinberg et al. (2019), indicating the contribution of different progenitors to the Solar abundances of various elements due to contributions ranging from from Big Bang nucleosynthesis to SN Ia. Many groups have offered sets of nucleosynthetic yields for SN II (Woosley & Weaver, 1995; Portinari et al., 1998a; Chieffi & Limongi, 2004), SN Ia (Thielemann et al., 2003; Iwamoto et al., 1999), and AGB stars (Karakas, 2010; Ventura et al., 2013) based on physical modelling of these systems for the community to utilise.

1.3.1 Chemical enrichment from massive stars vs. SN Ia

Any stellar object which explodes as a core-collapse supernova can be labelled a 'massive star'. The minimum mass of a SN II progenitor depends on how convection is treated in stellar modelling (e.g. Portinari et al., 1998b, who provide chemical yields for supernovae with $M_{\rm i} = 6$ M$_\odot$ for models including convective overshooting). Typically, any star with $M_{\rm i} > 8$ M$_\odot$ is considered to explode as a SN II. They are the dominant source of α-elements in the universe, also producing light elements (e.g. Na, Al), and Fe-peak elements (e.g. Ni, Mn, Fe).

The appearance of a 'knee' in the plot of the abundance ratio [α/Fe] vs. [Fe/H] has long been interpreted as a signature of the onset of SN Ia explosions, which enrich the ISM

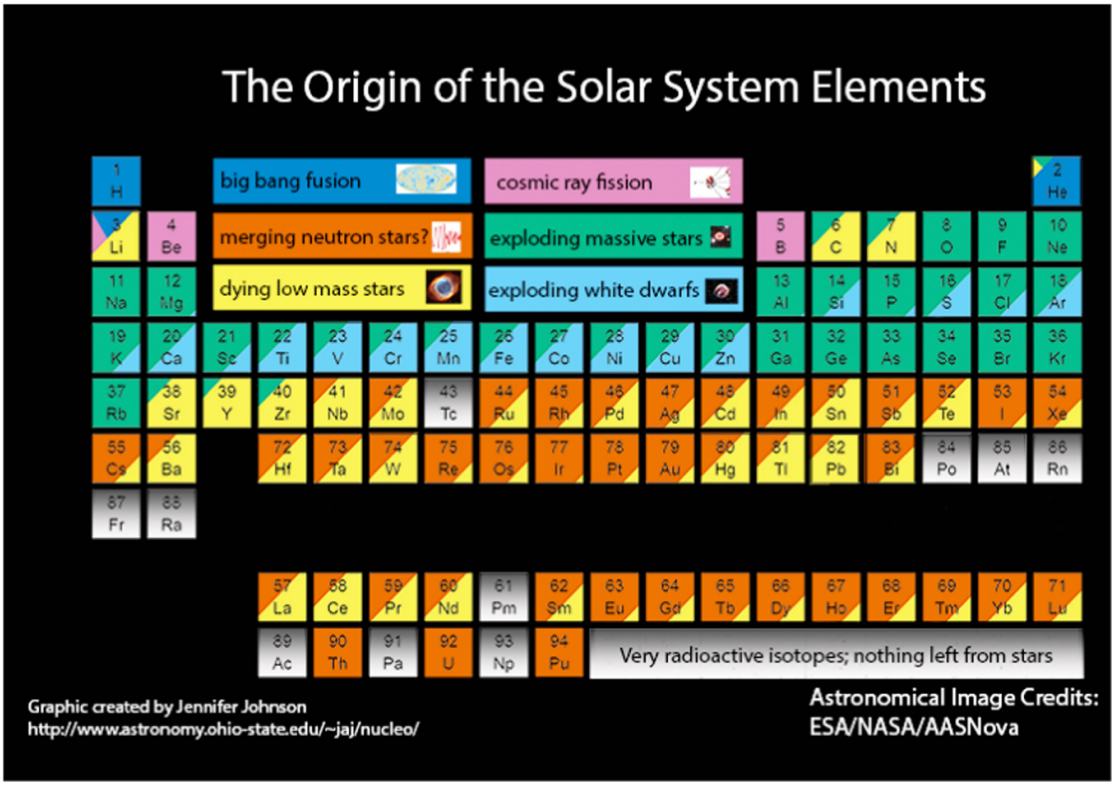

Figure 1.2: A diagram showing the periodic table of elements presented in Weinberg et al. (2019) and the fractional contribution from various nucleosynthetic pathways to the Solar abundances of these elements, made by Jennifer Johnson. It shows an intuitive guide as to the relative importance of different nucleosynthetic channels to the abundances of the Sun and stars in the Solar neighbourhood.

in Fe and other Fe-peak elements but a negligible amount of α-elements. The lifetimes of massive stars are characteristically short ($\tau \simeq 10$ Myr), meaning that the timescale of chemical enrichment by them is correspondingly short, and promptly responds to changes in the star formation rate. Since SN II depend on *ongoing* star formation, they contribute their metals to the ISM over a much shorter timescale than SN Ia. Conversely, the formation channels of SN Ia occur over a much longer timescale, depending on both the timescales of stellar (lifetimes) and binary (dynamical) evolution. It is thought that the delay time distribution (DTD hereafter) of a single stellar population (SSP, defined as a coeval population of stars forming from a single star-forming complex) is characterised by an initial minimum delay time, of the order 40 – 150 Myr Matteucci et al. (2009); Andrews et al. (2017); Maoz & Graur (2017), during which no SN Ia occur following the onset of star formation. After this time, SN Ia begin to contribute their metals (predominantly Fe; Iwamoto et al., 1999; Matteucci et al., 2009; Kobayashi et al., 2006a) to the ISM, a contribution that increases over time, reaches some value, and then begins to decline. Some authors have interpreted the knee as marking the moment at

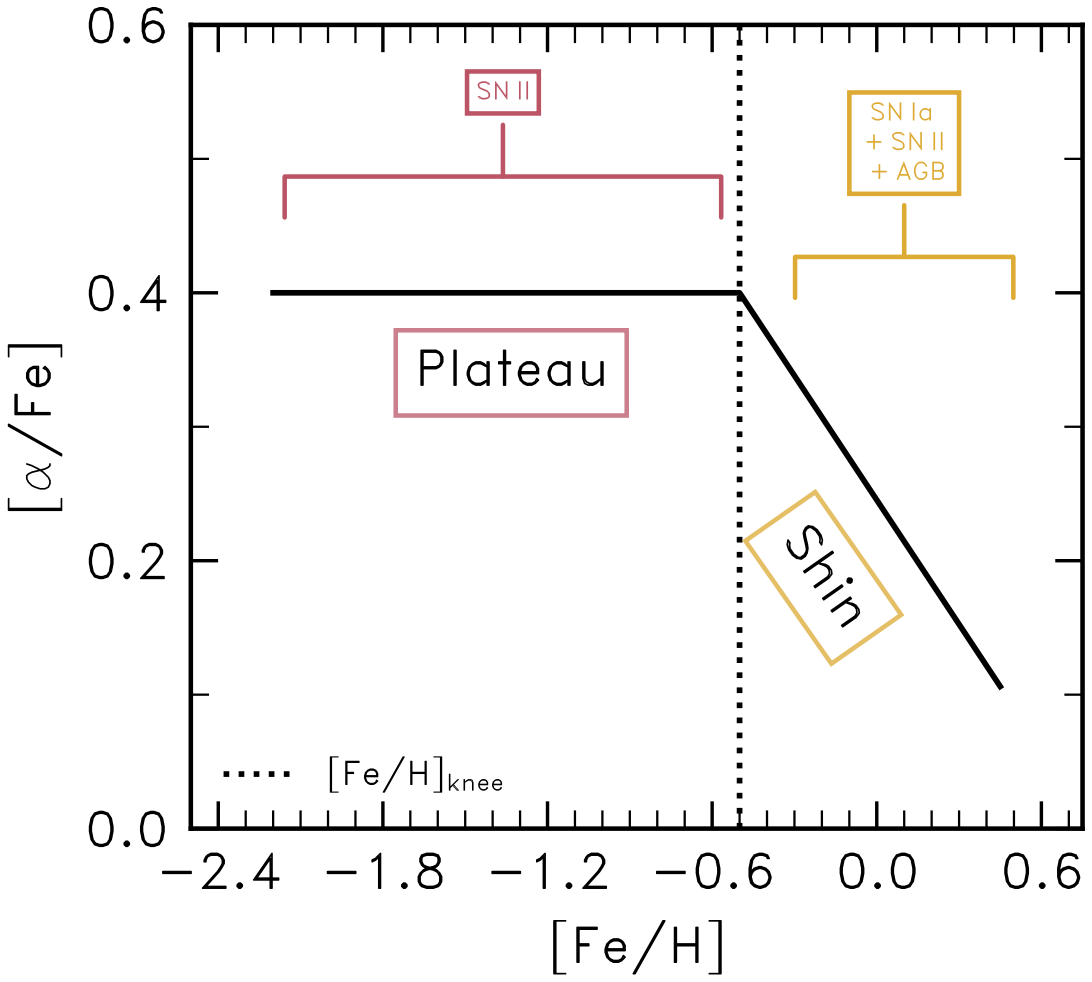

Figure 1.3: A schematic illustration of the typical distribution of a galaxy on the α-Fe plane. The plateau is characterised by an approximately flat trend of [α/Fe] vs. [Fe/H], followed by a shin characterised by declining [α/Fe] with [Fe/H].

which the minimum delay time has elapsed following the onset of star formation, or when the contribution by SN Ia otherwise becomes significant (i.e. when the e-folding timescale has elapsed, for the case of an exponential DTD).

1.3.2 The initial mass function

The initial mass function (IMF) describes the expected number of stars of a given mass that will form in an SSP. Its precise form, and its universality, are a topic of ongoing debate. There are three *widely-used* IMFs - those of Salpeter (1955), Kroupa (2001), and Chabrier (2003). The observations point to an IMF where the numbers of stars decrease with increasing stellar mass, with $\frac{dN}{dm}$ peaking at low m.

Salpeter (1955) found that the IMF was best-described by a one-slope power law:

$$\frac{dN}{dm} = Am^{-(1+x)}, \tag{1.2}$$

with a best-fitting value $x = 1.35$. A is a normalisation constant that ensures $\int_{m_{low}}^{m_{up}} \frac{dN}{dM} dm = 1$. In Kroupa (2001) it was suggested that the IMF of stellar clusters is universal, based on observations in the Milky Way. This universal IMF takes the form of a two-slope power law, with slopes $x_1 = 0.3$ for $0.08 < M/M_\odot \leq 0.5$, and $x_2 = 1.3$ for $M > 0.5\ M_\odot$. This is to say that the IMF peaks at $M = 0.5\ M_\odot$, and declines thereafter.

Chabrier (2003) proposed that the IMF behaves as a log-normal function such that:

$$\frac{dN}{dlog(m)} \propto e^{-(\log m - \log m_c)^2/2\sigma^2}, \tag{1.3}$$

for $M \leq 1\ M_\odot$. Thereafter the IMF behaves as a single-slope power law such that:

$$\frac{dN}{dm} \propto m^{-1.3\pm0.3}. \tag{1.4}$$

Changing the IMF significantly affects the predictions of a given model of galaxy chemical evolution. Depending on the normalisation and slopes, the contribution of stars at given masses will be significantly affected - for IMFs that invoke steeper slopes, the contribution by SNe II increases (a 'top-heavy' IMF), and vice versa (a 'bottom heavy' IMF). Most GCE models adopt either the Kroupa (2001) or Chabrier (2003), and the possible cosmic evolution of the IMF is not typically accounted for, nor entertained (Bastian et al., 2010 and Smith, 2020 can be consulted for contrasting views on this topic, with the former discussing the lack of variation and the latter vice versa). However, a number of works have posited that the IMF may vary strongly as a function of redshift (e.g. van Dokkum & Conroy, 2010). Referring back to Fig. 1.3, a piece of evidence suggesting a time-evolving IMF would be the abundance pattern of the plateau changing at very low metallicity (i.e. [Fe/H]<-2). To date, no compelling evidence attesting to such IMF variation has been identified in nearby stars with low metallicity (Nissen et al., 1994; Gonzalez et al., 2011; de Boer et al., 2014; Hendricks et al., 2014; Hayden et al., 2015; Hasselquist et al., 2017, 2021b; Fernandes et al., 2023a; Horta et al., 2021a).

To finish our IMF discussion, Carlin et al. (2018) recently made the distinction between the hydrostatic (from quiescent nuclear burning; O, Mg) and explosive (from nucleosynthesis during supernovae explosions; Si, Ca, Ti) in their chemical abundance study of stars comprising the Sagittarius (Sgr) stream, a stream of stellar debris left in the

wake of the passage of the Sagittarius dwarf spheroidal (dSph) galaxy. The 'HEx' ratio (hydrostatic-explosive ratio) measures the relative abundance ratio of the hydrostatic to the explosive α-elements.

1.4 Modelling galaxy chemical evolution

Galaxy chemical evolution studies the connection between a galaxy's assembly history and the chemical composition of its gas and stars. After the Big Bang imprinted the 'primordial' abundance patterns of hydrogen, helium and a trace amount of lithium, all other metals were produced subsequently via nuclear fusion over the course of stellar evolution. These elements can be ejected into the interstellar medium (ISM) either due to stellar winds (steady mass loss over the course of a star's lifetime), supernova explosions, or mass loss during the AGB phase of stellar evolution. The yields of these metals and how they change with the properties of their polluters are determined by the conditions in the interiors of stars of various masses, as well as the laws of nuclear physics. Thus, the chemical abundances of most elements in the atmospheres of stars reflect the composition of the interstellar clouds where they were formed (however, this does not apply to elements whose envelope abundances are changed due to various dredge up events during the red giant phase of stellar evolution). Studies of chemical evolution aim to discern the contributions to the chemical compositions of stellar populations by previous generations through the study of the abundances of elements produced by different nucleosynthetic channels.

Broadly speaking, there are four necessary ingredients to model the chemical evolution of galaxies: the initial mass function, the lifetimes of stars of various masses, their nucleosynthetic yields, and the star formation rate.

1.4.1 One-zone models

The most rudimentary model of galaxy chemical evolution is referred to as the 'simple model', a limiting case with an analytical solution by Schmidt (1959, 1963). This model assumes that the star forming gas reservoir is 'closed', meaning that there is no gas inflow into the box, nor outflows. The model also assumes that the gas evolves from the primordial chemical composition, an IMF that is invariant with time, and instantaneous mixing between stellar ejecta and the star forming gas. The 'instantaneous recycling

approximation' further assumes that stars above a certain mass immediately explode as supernovae, and thus their lifetimes can be ignored in the model (e.g. Talbot & Arnett, 1971; Searle & Sargent, 1972). Simple model prescriptions fail to reproduce a number of important observables, such as the metallicity distribution function of the Solar neighbourhood, frequently referred to as the 'G-dwarf problem' (van den Bergh, 1962; Schmidt, 1963). The G-dwarf problem refers to the fact that early GCE models failed to reproduce observations of stars in the Solar neighbourhood, over-predicting the number of metal-poor stars significantly, a tension that was eased by Tinsley & Larson (1978) who relaxed the assumption of a closed system, introducing a term representing gas inflow.

More realistic modelling can only be achieved by relaxing the assumptions of the simple model. This has included adding prescriptions for inflows, outflows, variable IMFs, and variable stellar yields. Recently, modelling frameworks that include one-zone prescriptions have become publicly available such as FLEXCE (Andrews et al., 2017), CHEMPY (Philcox & Rybizki, 2019), VICE (Johnson & Weinberg, 2020; Johnson et al., 2021a; Griffith et al., 2021), and FANCE (Marcelina Gountanis et al., 2024). Combined with chemical abundance data from the massive spectroscopic surveys, such as APOGEE (Majewski et al., 2017a), GALAH (De Silva et al., 2015; Martell et al., 2017), and H3 (Conroy et al., 2019a) they have been used to place constraints on the histories of chemical evolution for a number of the Local Group dwarf galaxies (e.g. Nidever et al., 2020a; Hasselquist et al., 2017, 2021b; Johnson et al., 2023).

1.4.2 Multi-zone models

Multi-zone models are an extension of the single-zone approximation, where individual one-zone models can experience the inflow of enriched gas from adjacent zones. Early multi-zone models implemented each zone as concentric annuli (Larson, 1976; Chiosi, 1980; Wyse & Silk, 1989; Matteucci & Francois, 1989; Prantzos & Aubert, 1995) with no mixing between zones. Radial gas flows have become a common feature in these models now, such that enriched material outflowing from one annulus may be transported to adjacent zones (Johnson et al., 2021b).

Observations of the Milky Way and other galaxies show compelling evidence that the properties of stellar orbits may vary with time. There is an intrinsic scatter in the age-metallicity relation in the Milky Way, speculated to be driven by the radial migration of different stellar populations across kpc distances (Edvardsson et al., 1993). This is

part of the motivation in the construction of multi-zone models, especially for more massive systems where the assumptions of one-zone models cannot broadly reproduce the observed properties of a galaxy.

1.4.3 Chemodynamical models

Chemodynamical models (Samland et al., 1997; Boissier & Prantzos, 1999; Kawata & Gibson, 2003; Khoperskov et al., 2021) differ greatly to single and multi-zone models in that they explicitly model stellar nucleosynthesis and lifetimes, the multiphase ISM (McKee & Ostriker, 1977), and dynamical interactions between stars and gas. They start from the collapse of a primordial gaseous halo due energy dissipation as a result of cloud collisions and radiation. Though cosmological hydrodynamical simulations are often referred to in the same breath as 'chemodynamical simulations', this is something of a misnomer. While the schemes and treatments utilised by chemodynamical models for the distribution and transportation of elements synthesised by SSPs are implemented in a largely identical fashion in cosmological simulations, systems in chemodynamical models do not *typically* form in a cosmological volume or context.

1.5 Pre-*Gaia* Galactic Archaeology: insights into the Chemical evolution of *the* Galaxy and its Satellite Population

In this section, we present results concerning the chemical abundances of stars comprising the Galaxy and its satellite populations, with an emphasis on what their implications are for our understanding of the formation and assembly of these systems over cosmic time.

1.5.1 The Milky Way

We give a brief description of the properties of the Milky Way at $z = 0$, in terms of its mass and structural parameters. The Milky Way is a typical barred spiral galaxy

(SB/c; Hodge, 1983), comprising a stellar disc, a central pseudo-bulge[2], and an old stellar halo. The stellar disk has a bar, and spiral arms but also comprises two distinct disc components: the thin and thick disks.

The Sun is situated within the disc of the Milky Way, within the Solar neighbourhood, defined as the region of the Galaxy at a galactocentric radius of $R \simeq 8$ kpc within $\simeq$ 100pc of the Sun, and at a scale height relative to the disc plane of $z \simeq 0.02$ kpc. Kinematically, it has a velocity in the direction of Galactic rotation of $(U, V, W)_{\odot} = (11.1, 12.24, 7.25)\ kms^{-1}$ (Schönrich et al., 2010). Residing in the disk, it has been historically difficult to estimate the structural parameters, and integrated properties of the Milky Way so as to place it on various canonical scaling relations that have been presented in the literature, such as the mass-metallicity relation (Tremonti et al., 2004; Gallazzi et al., 2005) and the Tully-Fisher relation (Tully & Fisher, 1977).

1.5.2 The Formation of the Milky Way

As we have described, a more granular view of the chemical evolution of galaxies can be provided by abundance analysis of resolved, individual stars comprising their field populations. The Milky Way and its satellites make appealing targets, by virtue of being some of the only resolved nearby galaxies. This is one of the primary tools of Galactic archaeologists, who use such data in combination with kinematics and ages (where available) to study 'fossil populations' residing in the Milky Way.

Eggen et al. (1962) speculated as to the origin of the Milky Way using chemistry and kinematic data available for 221 field dwarf stars in the Solar Neighbourhood. Under the assumption of a static, axisymmetric Galactic potential they integrated the stellar orbits of the stars comprising their samples and derived integrals of motion. Most significantly, they found a strong correlation between ultraviolet excess (a metallicity tracer) and orbital eccentricity which they suggested was indicative of the Milky Way's disk forming by rapid monolithic collapse of the star-forming gas $\simeq$ 10 Gyr ago, reaching dynamical equilibrium on a timescale of the order 10 Myr.

Searle & Zinn (1978a) presented results from analysis of a sample of red giants in Galactic globular clusters to measure the metallicity gradient of the Milky Way by considering the behaviour of [Fe/H] with galactocentric radius. There is a notable discontinuity

[2] A bulge is the classical definition of the bright central region of a disc galaxy. Where classical bulges are characterised by broad velocity dispersions, pseudobulges differ in that they have disc-like kinematics (Kormendy & Kennicutt, 2004).

in the radial metallicity gradient in the outer halo ($R > 8$ kpc) compared to the inner halo, an observation which is partially at odds with the scenario of Eggen et al. (1962). This is because the monolithic collapse from a proto-galaxy envisioned by Eggen et al. (1962) should produce a metallicity gradient out to the farthest galactocentric distances. This discontinuity was speculated to have arisen due to the merging of many smaller protogalaxies to form the stellar halo over several Gyr. In this scenario, then, the Galaxy formed by a combination of *in-situ* star formation and by the accretion of smaller systems which are most evident in the outer halo, rather than solely *in-situ* star formation. This scenario is also closer to what is predicted under the current cosmological paradigm, with galaxies assembling by the accretion of smaller so-called 'building blocks'.

1.5.3 The peculiar chemistry of the Milky Way Disk(s)

At the turn of the Millennium, a number of spectroscopic studies had derived spectroscopic abundances for stars in the Solar neighbourhood (Fuhrmann, 1998; Prochaska et al., 2000; Gratton et al., 2000; Bensby et al., 2003; Venn et al., 2004; Bensby et al., 2005; Nidever et al., 2014), revealing a significant spread, even bimodality, in [α/Fe] and other elements at fixed [Fe/H] in stars comprising the disk(s) of the Milky Way. Nissen & Schuster (2010, 2011) also revealed such a bimodality in [α/Fe] at fixed [Fe/H] for halo stars. The α-enhanced ([α/Fe]$\simeq$ 0.4) stars are distributed over larger distances from the plane of the Milky Way than those with [α/Fe]$\simeq$ 0. Moreover, they largely comprise the thick disk. The high-α stars also exhibit the knee at [Fe/H]$\simeq -0.5$. The stars with roughly Solar α-abundances are associated with the thin disk. However, it bears pointing out that there is significant spatial overlap between the high and low-α disk populations Mackereth et al. (2017).

The black 2D histogram in Fig. 1.4 shows the distribution of disk stars on the [Mg/Fe]-[Fe/H] plane using data from the APOGEE (Majewski et al., 2017b) survey, where the bimodality is clearly visible.

There are two leading models to explain the observed α-bimodality in the Milky Way disks. The first is the so-called 'two-infall model' (Chiappini et al., 1997; Grisoni et al., 2017) whereby after a period of star formation that formed the thick disk, there was an infall of fresh gas due to a major merger. The subsequent dilution of the star-forming gas reservoir with lower-metallicity gas and burst of star formation that resulted formed the thin, low-α disk. The second explanation is that the α-bimodality arose simply as a

consequence of secular processes involving a combination of chemical enrichment and radial migration, proposed by Schönrich & Binney (2009a,b).

It has been speculated that the Milky Way's α-bimodality may make it rare among disk galaxies at the same stellar/halo mass. Cosmological hydrodynamical simulations have provided a means of testing this hypothesis, though outcomes may vary on a simulation-by-simulation basis. Grand et al. (2018), on the basis of 6 cosmological zoom-in simulations of Milky Way analogues, found that there were two assembly histories that led to an α-bimodality in the Auriga simulations (Grand et al., 2017).

Recently, Nidever et al. (2024) presented α-abundances from a field of stars selected from the Panchromatic Hubble Andromeda Treasury photometric (PHAT) survey (Dalcanton et al., 2012) in M31 and demonstrated that for the sample of stars they observed there is no evident α-bimodality. This has been disputed by other authors (Kobayashi et al., 2023) on the basis of abundances derived from PNe observations, though the situation will undoubtedly become clearer as JWST data is taken in other fields in M31. As it stands, the question regarding α-bimodality being a rare phenomenon remains largely unanswered.

1.5.4 Chemical compositions of the Milky Way's satellite galaxies

The Milky Way's satellite galaxies are those that reside within the DM halo of the Galaxy, within virial radius of $r_{200} \simeq 200$ kpc (as measured by Dehnen et al., 2006). Simulations of structure formation predict that there should be around $\simeq 150$ dwarfs in the Milky Way satellite system (Drlica-Wagner et al., 2015). Detailed chemistry for large stellar samples, with ample sampling of the metallicity distribution function (MDF), is only available for a handful of dwarf galaxies, such as the Sagittarius dSph, the Magellanic Clouds, and Fornax.

The review of Tolstoy et al. (2009) gave a thorough presentation of contemporaneous observations that placed robust constraints on the histories of star formation and chemical evolution of the Local Group Dwarfs (Carina, Sculptor, Fornax, and the Sagittarius dSph). Notably, at the same metallicity ([Fe/H]) as Galactic field stars, the stars of dwarf galaxies tend to exhibit depleted α-element abundances. These galaxies were also demonstrated to have α-knees at different metallicities, all systematically lower than that of the thick disk. Tolstoy et al. (2009) speculated that there was a scaling relation between knee metallicity ($[\mathrm{Fe/H}]_{\mathrm{knee}}$) and $M_\star$ whose origin is similar to the

MZR. Galaxies with higher stellar masses, and thus halo masses, will be more able to retain ejecta from SN II before the onset of chemical enrichment by SN Ia in this picture, thus galaxies with higher $M_\star$ should have higher $[\mathrm{Fe/H}]_{\mathrm{knee}}$.

Furthermore, as previously stated, the diversity of SFHs at fixed $M_\star$ seen in the Milky Way's satellite population (Weisz et al., 2011, 2014; Gallart et al., 2015; Skillman et al., 2017) implies that there should also be a diversity of stellar distributions on the α-Fe plane, at a given stellar mass, and this is in fact what the data show.

The claim is often made that the knee simply marks the instantaneous abundances corresponding to the 'onset' of SNe Ia contributing their Fe to the ISM of a galaxy, whether this is defined as the notional minimum delay time of the observed SNe Ia DTD or its e-folding timescale (if it indeed can be approximated as an exponential function). An alternative hypothesis was suggested in that review, that you can form a knee due to a sudden decline in the SFR whereby the rate of Type II SNe promptly responds, leaving SN Ia to dominate the Fe-enrichment. Maoz & Graur (2017) combined an up-to-date measurement of the SN Ia DTD and nucleosynthetic yields from SN II and SN Ia with the cosmic SFR rate density to produce a model of the cosmic Fe and α accumulation history. They found that instead of the 'knee' in this model merely marking the onset of SN Ia explosions, they found that it coincided with the peak and decline in the star formation rate (when *'SN II kick the bucket'*[sic]), and after a timescale longer than that of the e-folding timescale or minimum delay time for their assumed DTD. In this context, then, there is a sizeable Fe contribution to the gas from which the high-α plateau stars formed.

Hasselquist et al. (2021b) presented an in-depth analysis of the chemical abundance patterns of four of the LGDs, and a substructure detected in the Galactic stellar halo believed to be a dwarf galaxy that was accreted around $z \simeq 2$ (which we discuss in finer detail in §1.7.1). They also resorted to one-zone models of galaxy chemical evolution, including treatments for inflows, outflows, stellar lifetimes, and metallicity-dependent yields. Fig. 1.4 is a recreation, where the same kind of GCE modelling has been performed using the VICE code (Johnson & Weinberg, 2020; Johnson et al., 2021a; Griffith et al., 2021). The most significant component of the modelling presented in Hasselquist et al. (2021a) is that of specifying a temporary, Gaussian increase in the star formation efficiency at some point in cosmic time. This is motivated by the fact that these dwarfs are characterised by a flattening, or even an increase, in [α/Fe] as a function of [Fe/H] which is speculated to arise due to bursts in star formation. Gilmore & Wyse (1991a) used GCE models to demonstrate that sudden increases in the star formation

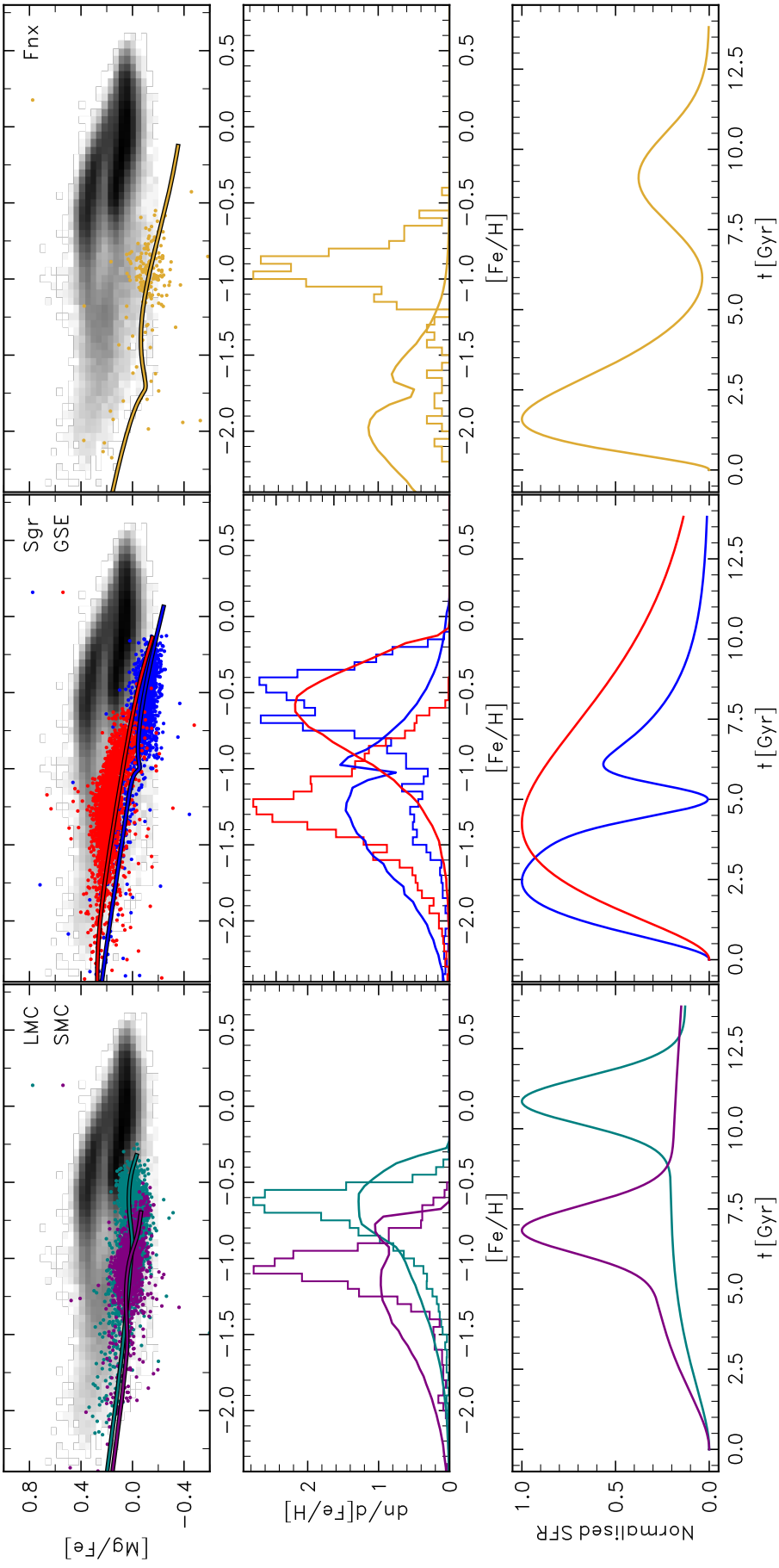

Figure 1.4: Recreation of both Fig. 11 from Tolstoy et al. (2009) and Fig. 9 from Hasselquist et al. (2021a), showing models instantiated with the same parameters using the VICE GCE modelling code. It shows the α-Fe (with Si as the representative element) planes for the same LGDs present in the APOGEE DR17 data. Teal, purple, red, blue, and yellow tracks show, respectively, the model [α/Fe](t) vs. [Fe/H](t) tracks for the LMC, SMC, Sgr dSph, Sausage/Gaia Enceladus, and Fornax dSph. The black 2d histogram in the background shows the distribution of stars comprising the halo and disk in APOGEE.

rate of a galaxy, such as by the accretion of fresh gas or an enhancement in the star formation efficiency, can give rise to a temporary enhancement of [α/Fe] as a function of [Fe/H] (also seen in Weinberg et al., 2017a; Hasselquist et al., 2017; Nidever et al., 2020a; Hasselquist et al., 2021b). In the cases of the LMC and the Sgr dSph, these starbursts have been attributed to interactions with the Milky Way.

1.6 The α-Fe knee, and lack thereof, in the Local Group

The position of the α-knee in the plot of [α/Fe] vs. [Fe/H] for a galaxy, as well as the slopes of the distribution before and after the knee, can lend insights about the star formation history that formed that galaxy. Hendricks et al. (2014) (and subsequently Nidever et al., 2020a) showed the scaling relation between $M_{\rm V}$ and [Fe/H]$_{\rm knee}$ for dwarf galaxies in which the presence of an α-knee had been confirmed. It takes the form of a linear relation, with hints of a large amount of scatter at fixed $M_{\rm V}$.

Fig. 1.5 shows the relation between $M_\star$ and [Fe/H]$_{\rm knee}$ for a number of galaxies in the Local Group, ranging several decades in $M_\star$ from the UFD Tucana II (Chiti et al., 2022) to the Galactic thick disk (Abdurro'uf et al., 2022). It shows that the scaling relation is linear and positive, subject to a high ($\simeq$1 dex) scatter at fixed $M_\star$. The origin of this scatter is uncertain, Hendricks et al. (2014) attribute galaxies exhibiting low [Fe/H]$_{\rm knee}$ for their stellar masses to non-uniform histories of star formation.

The formation of α-knees is the focus of §2 of this thesis. We examine the stellar α-Fe distributions of galaxies populating a high-resolution volume of the Evolution and Assembly of Galaxies and their Environments (EAGLE; Schaye et al., 2015; Crain et al., 2015) simulations in order to constrain the mechanism by which the knee forms in the simulation, as well as whether galaxies in the volume exhibit a similar scaling relation between $M_\star$ and [Fe/H]$_{\rm knee}$.

1.7 Galactic Archaeology in the ongoing 'Gaia Revolution'

This section presents an overview of recent results derived by the combination of *Gaia* astrometry and data from spectroscopic surveys concerning the assembly of the Milky

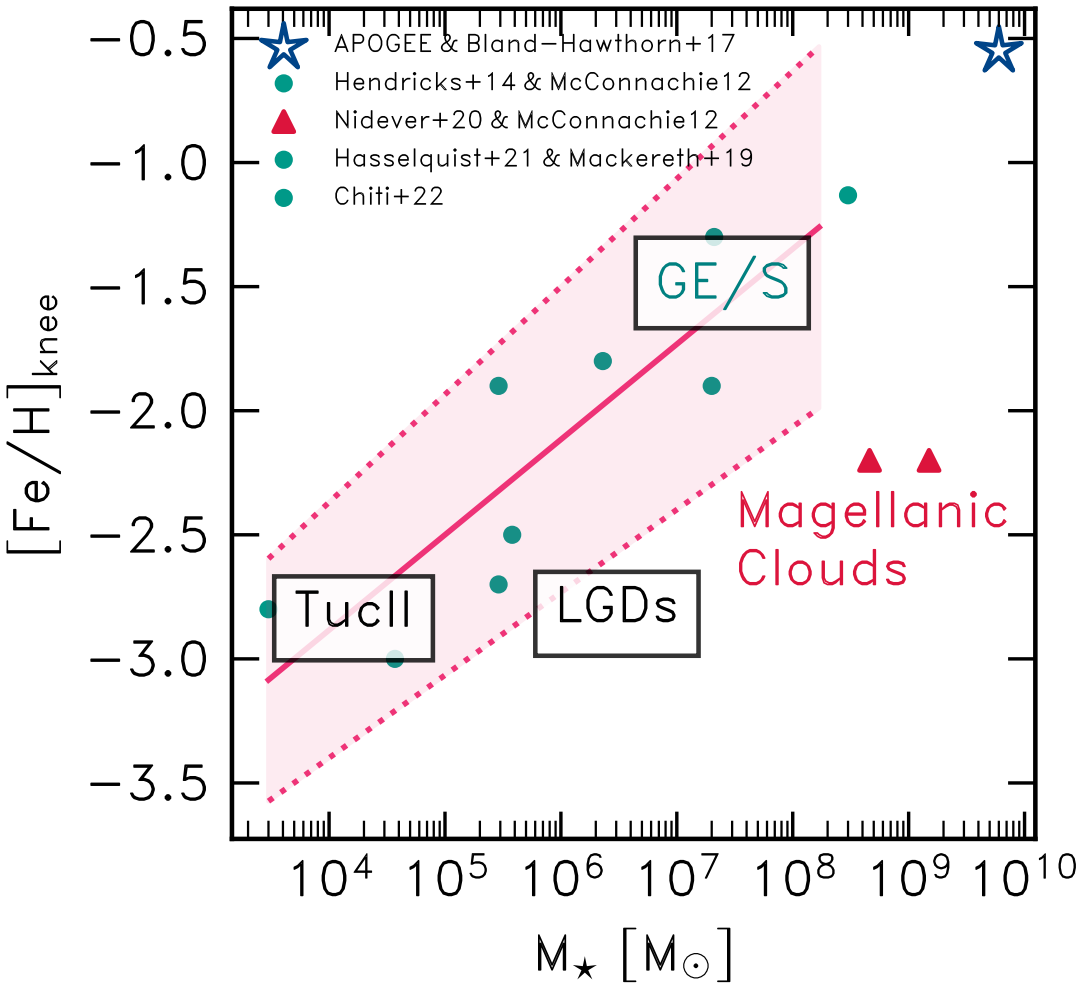

Figure 1.5: The observed scaling relation between $[\mathrm{Fe/H}]_{\mathrm{knee}}$ and $M_\star$ for the LGDs, using a combination of data from Abdurro'uf et al. (2022) and Bland-Hawthorn & Gerhard (2016) for the thick disk; Hendricks et al. (2014) and McConnachie (2012) for dSph data; Mackereth et al. (2019a) and Hasselquist et al. (2021b) for the Sausage/Gaia-Enceladus (see §1.7.1); and Chiti et al. (2022) for the UFD Tucana II. The pink shaded region illustrates a linear fit to the data, omitting the Magellanic clouds on the basis that a clear knee has not been measured in observational data, and the impact of their histories of star formation on their chemical abundances.

Way's disk and stellar halo. We will start by elaborating on why *Gaia* afforded such a granular look into the composition of the Milky Way's stellar halo.

Velocities in 3D space derived from astrometry and spectroscopy alone only afford a glimpse of the state of a star at a given point along its orbit, with no information about its dynamical properties. It is now commonplace to compute estimates of the integrals of motion for individual stars (Binney & Tremaine, 2008), under the assumption that the Milky Way's potential does not change as a function of time, is axisymmetric, and adiabatic (Henon & Heiles, 1964; Ollongren, 1965). Given these assumptions, authors

typically initialise orbits of individual stars with measured 6D phase space coordinates in a model potential representing the Milky Way (two common Milky Way potentials are those of Bovy, 2015; McMillan, 2017). These orbits are then integrated over several Gyr, whereupon the integrals of motion, and other orbital properties can be computed. The former are usually J_R, J_ϕ, and J_z - the radial, tangential, and vertical action, respectively. The latter quantities are the total orbital energy (E), eccentricity (e), etc. These are quantities unaffected by phase mixing of accreted debris into the Galaxy, and so individual stars that may not be spatially close to one another can be seen as distinct overdensities when integrals of motion are plotted alongside one another. Chemical abundances of such substructure detected in the stellar halo then allow us to infer the nature of the building blocks responsible for the buildup of the halo.

1.7.1 The discovery of the Sausage/Gaia Enceladus, and other substructure

Over the past few years, many groups have been leveraging *Gaia* and spectroscopic surveys to identify dynamical substructure in the Milky Way halo. A common thread among such studies has been to connect the existence of a detected substructure to the genesis of various components of the Milky Way, such as the stellar halo, the disks, and the bulge. There have been *many* claimed substructures, so we do not provide an exhaustive list here. We limit ourselves to highlighting key examples, where chemistry has played an important role in constraining the nature of these substructures. A recent review, providing a detailed census of such substructures, can be found in Deason & Belokurov (2024).

1.7.1.1 The Sausage/Gaia-Enceladus and associated substructure

In the pre-*Gaia* era the discovery of the Sagittarius dSph (Ibata et al., 1994a) revealed the ongoing minor merger between the Milky Way and one of its satellites occurring in real time, leaving an enormous tidal stream in its wake. Other authors (e.g. Helmi & de Zeeuw, 2000), made solid predictions regarding the power of massive astrometric surveys to identify systems that were accreted at much earlier cosmic epochs. In recent years, much attention has been drawn to some papers that effectively discovered some prominent substructures that were later revealed, albeit with superior numbers of stars, by *Gaia* (Searle & Zinn, 1978a; Helmi et al., 1999).

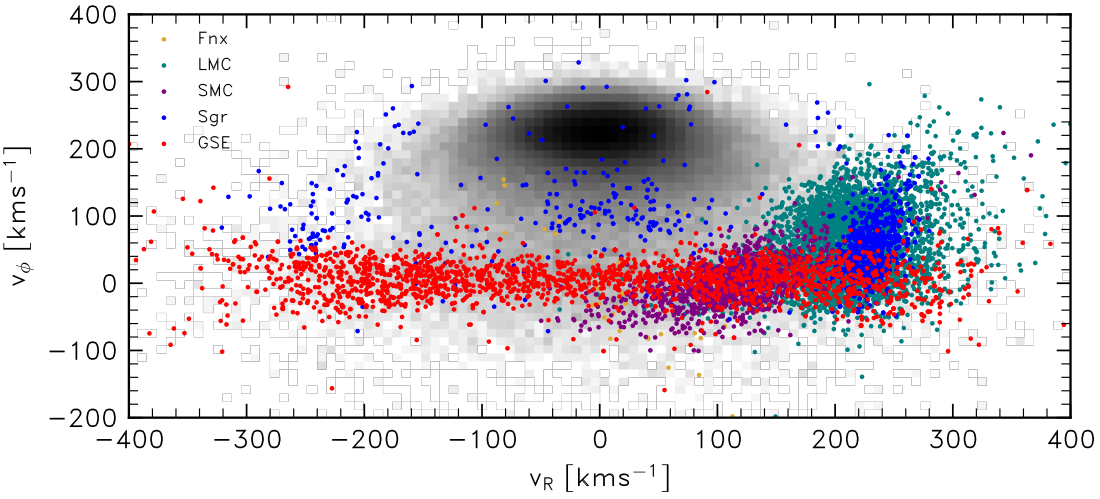

Figure 1.6: A plot of v_ϕ vs. v_R for a sample of APOGEE DR17 stars cross-matched with *Gaia* DR3. Also shown are points representing the galaxies in Hasselquist et al. (2021a). The Sausage/Gaia-Enceladus is clearly visible in this plot as an extended structure of red points, characterised by a huge radial velocity dispersion.

Following the first data release of the *Gaia* survey (Gaia Collaboration et al., 2018), Deason et al. (2018) observed a sudden, sharp decline in the stellar density of the Milky Way's stellar halo that coincided with the apocentre of a population of highly-eccentric stars. Soon thereafter, Helmi et al. (2018) and Belokurov et al. (2018a) reported the discovery of the so-called 'Sausage' (also dubbed 'Gaia Enceladus'). In the *Gaia* data, the thick disk appears as a clear overdensity (see Fig. 1.6) in the plot of tangential velocity as a function of radial velocity characterised by significant rotation ($v_\theta \sim 200$ kms^{-1}), and with a negligible mean radial velocity $v_\mathrm{r} \sim 0$ kms^{-1}. A significant overdensity, characterised by negligible rotation $v_\theta \sim 0$ kms^{-1} and a significant radial velocity dispersion (forming an ellipsoidal shape, hence the term 'sausage'), is clearly visible in their plots of v_θ vs. v_r.

By performing a cross-match between the *Gaia* data and main sequence stars in SDSS DR9 (Ahn et al., 2012), they were able to demonstrate that this overdensity is metal-poor, and that the observed anisotropy as a function of metallicity (at all heights with respect to the disk) was inconsistent with that predicted by cosmological zoom-in simulations of MW-like galaxies whose stellar haloes assembled by the continuous accretion of less-massive satellites ($M < 10^{10}$ M$_\odot$), and instead consistent with a major merger ($M > 10^{10}$ M$_\odot$), coincidental with the epoch during which the disk formed in the MW analogue.

Based on APOGEE data, Helmi et al. (2018) demonstrated that the distribution of the Sausage/Gaia-Enceladus' stars on the α-Fe plane was consistent with the population's

purported accreted origin, resembling that of bright dwarfs in the Local Group. Since this result, there has been an industry producing identifications of substructure in the extant data, regardless of whether they have an *in-situ* or accreted origin. In the following subsection, we provide a quick roundup of some of the more notable identified substructures, and their chemodynamical properties.

The discovery of the Sausage was a potent indicator that, indeed, massive astrometric and spectroscopic datasets are a hugely powerful tool that we can use to reconstruct the assembly history of the Galaxy by looking for accreted substructure, as predicted by theoretical work (Helmi & de Zeeuw, 2000). A number of other substructures have since been identified, both chemically and kinematically, and a coherent picture has emerged concerning the role of accretion in both the buildup of the stellar halo, as well as the formation of the Milky Way disks. What is clear beyond doubt is that around the epoch during which the high-α disk formed, the Milky Way underwent a major merger with another system.

In that context, Belokurov et al. (2020) identified high-eccentricity, high-metallicity stars from a large data set comprising *Gaia* astrometry and photometry; 2MASS (Skrutskie et al., 2006) and PAN-STARRS (Magnier et al., 2013) photometry; and spectroscopic information from APOGEE (Majewski et al., 2017b), LAMOST (Deng et al., 2012), RAVE (Steinmetz et al., 2006), SEGUE (Yanny et al., 2009), and GALAH (De Silva et al., 2015; Martell et al., 2017). They identified a 'splash' population - stars that were originally situated in the proto-disk of the Milky Way and whose orbits were heated by the major merger with the S/GE progenitor.

1.7.1.2 Other substructure

Barbá et al. (2019) identified FSR 1758, a candidate dSph or GC obscured by the bulge on the basis of a sweeping search of *Gaia* DR2, DECam Plane Survey, and Vía Láctea Extended Survey data. It is characterised by a highly eccentric, retrograde orbit. Estimates of its mass and size indicate that it may be as, if not more, massive than ω Centauri. (Myeong et al., 2019) identified that FSR 1758 formed a cluster of other Galactic GCs in action space, and that stars in the halo also occupying this region exhibited different abundance patterns compared to the Sausage/Gaia Enceladus. Thus, it was posited that this population with its stars and associated GCs represented yet another building block of the halo that was accreted at early cosmic time.

Horta et al. (2021a) identified 'Heracles', a substructure confined to the inner region ($R < 4$ kpc) of the Galaxy. Hawkins et al. (2015) and Das et al. (2020) discriminated accreted and *in-situ* populations from one another on the basis of the so-called [Mg/Mn]-[Al/Fe] plane in lieu of the [α/Fe] plane. The adoption of Mn as a metallicity indicator is motivated by the fact that its contribution from SN II is minimal compared to SN Ia, contrasted to the case of Fe (see discussion in Weinberg et al., 2019, although, they adopt Mg as a metallicity indicator). Furthermore, due to the highly metallicity-dependent yields of Al, the [Mg/Mn]-[Al/Fe] plane clearly separates systems with dwarf-like abundance patterns from the locus occupied by stars comprising the disk where [Mg/Fe] vs. [Fe/H] does not. Horta et al. (2021a) found that Heracles exhibits abundance patterns consistent with lying on the 'accreted' locus of this chemical plane, though this is not without some *in-situ* contamination in this region (which is discussed at length in Horta et al., 2021a, in addition to Vasini et al., 2024).

Belokurov & Kravtsov (2022) and Myeong et al. (2022) defined a subsequent substructure, dubbed 'Aurora'. They first separated the APOGEE DR17 (Abdurro'uf et al., 2022) into *in-situ* and accreted components by selecting stars with [Fe/H]< -1.3 and making cuts based on [Al/Fe]. *In-situ* stars are identified as being kinematically hot with an isotropic velocity ellipsoid and some rotation. These stars are hypothesised to represent early *in-situ* halo of the Milky Way. Between [Fe/H]$= -1.3$ and [Fe/H]$= -0.9$, the age-metallicity relation shows a period of rapid chemical enrichment combined with a transition to disky kinematics. In this metallicity range, Conroy et al. (2022a) also presented the [Mg/Fe]-[Fe/H] plane for a sample of *in-situ* stars present in the H3 survey (Conroy et al., 2019b). A 'rise' in [α/Fe] is observed after an initial decline, also purportedly observed by Rix et al. (2022) using a combination of APOGEE and abundance data derived from *Gaia* XP spectra. This is attributed to an enhancement in the star formation efficiency of the high-α disk as it 'span up' and formed.

1.8 Globular clusters in the Galactic Archaeology framework

As was already alluded to by the results of Searle & Zinn (1978b), globular clusters serve as an important tracer of both the assembly and chemical enrichment histories of galaxies (reviews can be found in Brodie & Strader, 2006; Forbes et al., 2018). While a significant fraction of the Galaxy's globular clusters undoubtedly formed by some

in-situ mechanism, it is thought that the building blocks that formed its stellar halo are survived by their own globular clusters at $z = 0$ (Kruijssen et al., 2019b). This is a simple consequence of ΛCDM because hierarchical assembly implies that the globular cluster system of the Milky Way must at least comprise some accreted systems.

The formation mechanism responsible for GCs is debated in the literature, though there are two leading classes of models describing this. The first attests that the formation of GCs was facilitated only by the conditions that existed in the early Universe, forming before or during the epoch of reionisation (Peebles, 1984; Katz & Ricotti, 2014; Trenti et al., 2015; Chiou et al., 2019).

The second class of models suggest that GC formation is simply a component of the secular evolution of galaxies and a natural consequence of star formation (Elmegreen & Efremov, 1997; Muratov & Gnedin, 2010; Kruijssen, 2015; Choksi et al., 2018). Thus, GC ages should peak around the time of the peak in the star formation rate density.

For mono-metallic globular clusters in the Local Group, deep observations down to the main sequence turnoff (MSTO) allow synthetic CMDs to be fit to the data, constraining the ages and metallicities of these systems (Forbes & Bridges, 2010; Leaman et al., 2013; Cassisi & Salaris, 2013; Usher et al., 2019; Kruijssen et al., 2019b). The Galaxy hosts some 175 GCs (Harris, 2010). Ages and metallicities have been measured for the order of $\simeq$ 100 of them. Thus, the AMR of the Milky Way is well-constrained on the basis of GCs. Studies have revealed that it is bifurcated, exhibiting a metal-rich and a metal-poor arm which are considered to be the 'disc' and 'halo' sequences (Leaman et al., 2013).

While GCs were once considered to be the archetypal 'SSPs' (single stellar populations, defined as being coeval, and sharing the same abundance pattern), photometric studies revealed the presence of multiple populations in most GCs. This manifests itself as a significant spreads and anticorrelations in the abundances of light elements (e.g. C, N, O, Na, Mg, Al) at fixed metallicity (the reviews of Gratton et al., 2012; Renzini et al., 2015; Bastian & Lardo, 2018, give a chronology to these observations). This realisation largely came about as a result of the increased capabilities of facilities to extract deep images of the Galactic GCs (in particular, HST observations have played a huge role with the ACS and WFC cameras), as well as multi-object high resolution spectroscopy.

To briefly summarise, the Galactic GCs are roughly characterised by two different stellar populations, referred to as the 'first generation' (1G) stars, and the 'second generation' stars (2G). The stars comprising the 1G population tend to exhibit abundance

patterns at fixed [Fe/H] that are consistent with field populations at the same metallicity. Conversely, the 2G stars exhibit correlations and anti-correlations between different light element abundances that cannot be reconciled with chemical evolution expected from secular galaxy formation. These include *i)* the Na-O anticorrelation, *ii)* the Al-Mg anticorrelation, and *iii)* the C-N anticorrelation. These abundance patterns are seen across stars of all evolutionary types, meaning that the gas reservoir they formed from must have also had this composition. However, there is no agreement on the progenitors responsible for this chemistry (Norris & Da Costa, 1995; Johnson & Pilachowski, 2010; Marino et al., 2011, 2019; Schiavon et al., 2017b; Alvarez Garay et al., 2024; Schiavon et al., 2024)

As we mentioned in §1.3, at sufficient temperatures several nucleosynthetic channels responsible for the production of He can occur in stellar interiors. These are the NeNa and MgAl cycles, which produce the observed anticorrelations due to the destruction of certain species. Thus, the gas reservoir must have comprised material processed by such reactions. A prominent candidate for the polluters is AGB stars (Karakas, 2010; Ventura et al., 2013; Karakas & Lugaro, 2016), since they undergo hot bottom burning in their stellar interiors, and dredge-up can bring the products of these reactions to the stellar surface. These are then removed in the stellar wind, which has a characteristically low velocity (compared to SNe, $v_{\text{wind, AGB}} \simeq 40\text{kms}^{-1}$; Herwig, 2005), which adds further appeal to this scenario as such ejecta are more easily retained by the cluster, whereas the velocity of SN ejecta easily exceeds the escape velocity of GCs. However, models attempting to invoke the formation of 2G stars by AGB enrichment are hindered by the 'mass budget problem', and do not reproduce the full spectrum of abundance anomalies. Briefly, the 'mass budget problem' simply refers to the fact that it is difficult to build up a gas reservoir with sufficient mass to form the 2G stars with AGB ejecta alone, given the typical ratios observed between the enriched and unenriched populations in the Galactic GCs (Bastian & Lardo, 2018).

It is because of these abundance anomalies that the contribution of GCs to the assembly of the halo has been constrained. Since the onset of the MP phenomenon is unique to the formation of GCs, it is possible to identify stars in the field of the Milky Way exhibiting the abundance patterns of 2G stars with a sufficiently large sample (Schiavon et al., 2017a; Belokurov & Kravtsov, 2023a). By looking at the stellar density of former GC stars as a function of galactocentric radius, it is possible to compute the contribution of destroyed GCs to the stellar halo (Horta et al., 2021c).

1.8.1 Accreted NSCs in the stellar halo

Further distinction has been made about the survival of the nuclear star clusters of the building blocks that have been accreted by the Milky Way. NSCs are dense clusters of stars situated at the deepest point of the potential wells of most galaxies (Neumayer et al., 2020).

There are two objects within the virial radius of the Milky Way that we can say with some degree of certainty are the nuclear star clusters of accreted galaxies, M54 and ω Cen. The former is still embedded at or near the centre of the Sagittarius dSph, while the other is situated on a retrograde orbit coplanar with the disk of the Milky Way (Majewski et al., 2000). It is thought that most galaxies host an NSC and that for galaxies with ($M_\star \leq 10^9$ M$_\odot$) they form by the inspiralling of globular clusters into the centre of these systems. At higher masses, both in-situ star formation and inspiralling are thought to play a role (Fahrion et al., 2021).

In the case of ω Cen, there have been dynamical associations made between it and a number of the halo substructrues we previously discussed. Myeong et al. (2019) speculated that it may be part of the system that also comprises FSR 1758. Conversely, Massari et al. (2019) speculated that it originates from the Sausage/Gaia Enceladus merger. Chemical comparison between ω Cen and these substructures is made difficult by the fact that it exhibits some of the most extreme abundance patterns in the Milky Way GC system that are both obvious photometrically (Bellini et al., 2010; Milone et al., 2017a; Nitschai et al., 2024) and spectroscopically (Johnson & Pilachowski, 2010; Marino et al., 2011; Mészáros et al., 2021a; Alvarez Garay et al., 2024).

Interpreting the abundance patterns of ω Cen is the focus of §3, where we use a combination of APOGEE abundances, *Gaia* astrometry, MUSE data, HST photometry, and one-zone galaxy chemical evolution models to thoroughly characterise the MPs of the cluster, and speculate as to how these abundance patterns came about.

1.9 Summary and thesis outline

Thus far, we have presented a summary of the chemical and kinematic properties of stellar populations in the Milky Way and Local Group dwarfs. We also discussed the role of galaxy chemical evolution modelling in interpreting these abundances, and finally

the Galactic globular clusters, and their relation to substructures identified in Galactic archaeological studies.

In the following chapters, we describe in detail the work conducted over the course of this PhD on the basis of cosmological hydrodynamical simulations, and observational data for the Milky Way and its satellite galaxies.

1. In §2 we present our results concerning the formation of α-Fe knees in a high-resolution volume of the EAGLE simulations, constraining the scaling relation between $M_\star$ and $[\mathrm{Fe/H}]_{\mathrm{knee}}$ and comparing the abundance patterns of simulated galaxies to those seen in the Local Group data.

2. In §3 we present a detailed chemical study of the Galactic stellar cluster ω Centauri, placing novel constraints on the formation of this enigmatic stellar system.

Following the main chapters, I summarise the conclusions that we have drawn from this work and reflect on the direction I would like to see both myself and the field progress toward in future work, concerning galaxy chemical evolution and Galactic archaeology.

Chapter 2

The formation of α-knees in realistic simulations of galaxy formation

When the sun has set, no candle can replace it.

George R. R. Martin

The content of this chapter comprises material presented in the paper Mason et al. (2024, 10.1093/mnras/stae1743) in collaboration with Ricardo Schiavon, Rob Crain, David H. Weinberg, Joel Pfeffer, Joop Schaye, Tom Theuns, and Matthieu Schaller. The simulation data was created by the EAGLE collaboration.

We examine the stellar [α/Fe]-[Fe/H] distribution of $\simeq$ 1000 present-day galaxies in a high-resolution EAGLE simulation. Roughly half of the galaxies exhibit the canonical distribution, characterised by a sequence of low-metallicity stars with high [α/Fe] that transitions at a 'knee' to a sequence of declining [α/Fe] with increasing metallicity. This population yields a knee metallicity - galaxy-mass relation similar to that observed in Local Group galaxies, both in slope and scatter. However, many simulated galaxies lack a knee or exhibit more complicated distributions. Knees are found only in galaxies with star formation histories (SFHs) featuring a sustained decline from an early peak ($t \simeq 7$ Gyr), which enables enrichment by Type Ia supernovae to dominate that due to Type II supernovae (SN II), reducing [α/Fe] in the interstellar gas. The simulation thus indicates that, contrary to the common interpretation implied by analytic galactic chemical evolution (GCE) models, knee formation is not a consequence of the onset of enrichment by SN Ia. We simulate the chemical evolution of a typical classical knee galaxy using a leaky box single-zone GCE model instantiated using the VICE (Johnson & Weinberg, 2020; Johnson et al., 2021a; Griffith et al., 2021) package. We input the SFH of a simulated galaxy exhibiting a knee and a constant gas consumption timescale, finding it yields an α-rich plateau enriched only by SN II, but the plateau comprises little stellar mass and the galaxy forms few metal-poor ([Fe/H]$\lesssim$–1) stars. This follows from the short, constant gas consumption timescale typically assumed by GCEs, which implies the presence of a readily-enriched, low-mass gas reservoir. When an initially longer, evolving consumption timescale is adopted, VICE reproduces the simulated galaxy's track through the [α/Fe]-[Fe/H] plane and its metallicity distribution function.

2.1 Introduction

Galactic archaeology has undergone a renaissance in recent years with the emergence of a number of ambitious stellar surveys. Precision element abundances and phase space properties of millions of stars have now been measured and interpreted within the broader context of theoretical predictions from galaxy formation theory to help elucidate the formation history of the Galaxy. Such efforts include RAVE (Steinmetz et al., 2006), SEGUE (Yanny et al., 2009), Gaia-ESO (Gilmore et al., 2012; Randich et al., 2013), GALAH (De Silva et al., 2015; Martell et al., 2017), APOGEE (Majewski et al., 2017a), H3 (Conroy et al., 2019a), and the Gaia mission (Gaia Collaboration et al., 2018), as well as surveys forthcoming in the near future (e.g., de Jong et al., 2019; Gonzalez et al., 2020; Jin et al., 2023).

It has been suggested that the Milky Way exhibits properties somewhat atypical of similarly massive disc galaxies (see, e.g., Mackereth et al., 2018a; Schiavon et al., 2020), implying that study of the Galaxy alone cannot offer a comprehensive picture of galaxy formation and evolution. Besides the Galaxy, the Local Group also hosts a population of dwarf galaxies ($M_\star \lesssim 10^{10}$ M$_\odot$) which comprise both 'fossil' and young stellar populations. Dwarfs are the most abundant galaxies in the Universe (e.g. Li & White, 2009; Baldry et al., 2012) and yet detailed observations of their stellar populations are comparatively sparse compared to the Milky Way. The Local Group is thought to host at least ≃150 (e.g. Drlica-Wagner et al., 2015; Newton et al., 2018) dwarf galaxies, which are observed to exhibit diverse star formation histories, even at fixed $M_\star$ and even within the same morphological class (see, e.g., Weisz et al., 2011, 2014; Gallart et al., 2015; Skillman et al., 2017). The Local Group in totality thus represents a rich parameter space and understanding how the panoply of its formation histories maps onto the so-called canonical chemical planes in the literature remains an open question.

For nearby galaxies, the resolvable distribution of individual stars in the [α/Fe]-[Fe/H] plane (hereafter α-Fe plane, and sometimes referred to as the Tinsley-Wallerstein diagram following Tinsley, 1979 and Wallerstein, 1962) encodes a wealth of information about the galaxy's formation history. The distribution exhibited by galaxies is affected by, amongst other things, the timescales of production of the α-elements (i.e. O, Mg, Si, Ca, Ti) and Fe. The former are synthesised by the progenitors of core-collapse supernovae (hereafter SN II, e.g. Portinari et al., 1998b; Kobayashi et al., 2006b) whereas the latter is synthesised by both SN II and Type Ia supernovae (hereafter SN Ia, e.g. Woosley & Weaver, 1994; Iwamoto et al., 1999; Seitenzahl et al., 2013; Gronow et al., 2021a,b). The two classes of SN explode and return their nucleosynthetic products to the interstellar medium (ISM) on markedly different timescales, fostering a time dependence of the characteristic ratio between the abundances of α-elements and iron, [α/Fe], in the ejecta produced by a simple stellar population.

The early phase of chemical evolution stemming from a nascent stellar population is dominated by SN II due to the short lifetimes of their progenitors ($\tau \simeq 3 - 30$ Myr), whose masses range between $M_\star \simeq 8$ and 100 M$_\odot$ (e.g., Portinari et al., 1998b). The hydrostatic α-elements O and Mg are produced during the hydrostatic burning stage over the progenitor's lifetime while the explosive α-elements (Si, Ti, and Ca) are produced in the SN explosion.

SN Ia originate from white dwarf (WD) stars in binaries that experience mass transfer from their companion stars, exceeding the Chandrasekhar mass (Iwamoto et al., 1999).

This is thought to strongly constrain the minimum timescale over which SN Ia can occur as white dwarfs are the culmination of low-mass stellar evolution (the remnants of stars with $M < 8$ M$_\odot$). Consequently, the minimum time taken for SN Ia to explode is governed by a combination of the main sequence lifetime of the most massive WD progenitors ($\tau \sim 100$ Myr; Matteucci et al., 2009) and the dynamical evolution of the binary systems in a given stellar population. Thus, following an episode of star formation, it is expected that there is a characteristic delay before SN Ia detonations begin, and a further timescale over which they explode in *significant* numbers. The distribution of SN Ia delay times (SN Ia DTD) for an SSP ($R_{\rm Ia}$, e.g. Graur & Maoz, 2013) is generally thought to scale as $\propto t^{-1}$ after a minimum delay (see, e.g., Maoz & Graur, 2017), evidenced by the observed volumetric SN Ia rate density. SN Ia are significant contributors to the Fe budget of the ISM (see Fig. 2 of Wiersma et al., 2009b, for example), but synthesise no α-elements.

Analytical models of chemical evolution typically implement an exponential form of the SN Ia DTD ($R_{\rm Ia} \propto e^{-t/\tau_{\rm Ia}}$ where $\tau_{\rm Ia}$ is the e-folding timescale) and a minimum delay time ($t_{\rm d}$, e.g. 150 Myr per Nidever et al., 2020a; Johnson & Weinberg, 2020; Johnson et al., 2021a; Griffith et al., 2021). As these models do not account for the hierarchical assembly of galaxies from their progenitors, by construction SN II alone contribute to the chemical enrichment of the ISM over a period $t_{\rm d}$ following the onset of star formation in a nascent galaxy, leading to the formation of a flat sequence of elevated [α/Fe] at low [Fe/H], whose absolute value in [α/Fe] is initially set by the [α/Fe] of pure SN II yields. When SN Ia enrichment begins, [α/Fe] progressively decreases, increasingly so as t approaches the DTD's e-folding timescale. This results in [α/Fe] decreasing as [Fe/H] increases (e.g., Matteucci & Brocato, 1990). The ensuing decrease in [α/Fe] leads to the appearance of a characteristic transition in the α-Fe plane commonly referred to as the "α knee".

For the purposes of the work presented in this chapter, we labelled the sequence of approximately flat [α/Fe] as a function of [Fe/H] located at [Fe/H]<[Fe/H]$_{\rm knee}$ as the "plateau" and the sequence of declining [α/Fe] as a function of [Fe/H] located at [Fe/H]>[Fe/H]$_{\rm knee}$ the "shin"[1]. To date, a knee has been observed in a number of the Local Group Dwarfs (LGDs) (e.g. Gonzalez et al., 2011; de Boer et al., 2014; Hendricks et al., 2014; Carlin et al., 2018; Hasselquist et al., 2021b) and the Galactic thick

[1]The terms plateau and shin were originally coined by McWilliam (1997) and Nidever et al. (2020a), respectively.

disk (e.g., Wallerstein, 1962; Bensby et al., 2014; Hayden et al., 2015; Mackereth et al., 2019a).

There has been much interest in measuring the position of this knee in [α/Fe]-[Fe/H] space (respectively, $[\alpha/\mathrm{Fe}]_{\mathrm{knee}}$ and $[\mathrm{Fe/H}]_{\mathrm{knee}}$). Some studies (Hendricks et al., 2014; Nidever et al., 2020a) show that $[\mathrm{Fe/H}]_{\mathrm{knee}}$ scales with both the stellar mass and dynamical mass of a galaxy, which is in broad agreement with observations of the α-abundances of massive galaxies (e.g. Worthey et al., 1992; Trager et al., 2000; Schiavon, 2007; Johansson et al., 2013; Conroy et al., 2014; Segers et al., 2016). Based on one-zone galaxy chemical evolution (GCE) models, some groups (e.g., Andrews et al., 2017) have interpreted the broad empirical evidence as resulting from a correlation between galaxy mass and the gas consumption timescale[2]. If a galaxy's reservoir of star-forming gas is initially characterised by a short t_{g}, more stars form before the minimum delay time of the SN Ia DTD, and many more before the e-folding timescale τ_{Ia}. Thus, more stars form and experience chemical enrichment with the metallicity-dependent yield closer to that of SN II *only*, leading to the formation of a longer plateau, and thus leading to a greater $[\mathrm{Fe/H}]_{\mathrm{knee}}$. Feedback efficiency is also likely to be important, as efficient feedback may expel much of the enriched gas in galaxy-wide outflows before it is incorporated into new stellar generations. Thus, the properties of the underlying dark matter distribution must be important as stellar feedback is less efficient in removing the star-forming gas in a galaxy with a deeper potential well and a higher entropy (e.g. Keller et al., 2014; Davies et al., 2020).

However, a growing number of observations (e.g., Vargas et al., 2013, 2014; Nidever et al., 2020a) suggest that the α knee is not ubiquitous. Measurements of $[\mathrm{Fe/H}]_{\mathrm{knee}}$ in dwarf galaxies by Hendricks et al. (2014) and Nidever et al. (2020a) show that the relationship between $M_\star$ and $[\mathrm{Fe/H}]_{\mathrm{knee}}$ is subject to a large degree of scatter at fixed $M_\star$. In addition, there are dwarfs in the Local Group that display monotonically-decreasing trends of [α/Fe] as a function of [Fe/H], with no evidence for the presence of a knee (e.g., Vargas et al., 2013, 2014).

Moreover, the premise that α knee formation corresponds only to the onset of SN Ia has been called into question by other authors. On the basis that chemical enrichment by massive stars is highly correlated with ongoing star formation, Tolstoy et al. (2009)

[2]The gas consumption timescale, t_{g}, is the inverse of what is often termed the 'star formation efficiency' (SFE) by the GCE community. We do not use this terminology in order to avoid possible confusion with the efficiency per free-fall time term in the Schmidt star formation law.

suggested that a declining-α shin could form due to a decrease in the SFR, which induces a prompt reduction of the SN II rate but a delayed reduction in that of SN Ia.

The emergence of cosmological simulations of galaxy formation that broadly reproduce a wide range of key properties of the observed present-day galaxy population (for a recent review see Crain & van de Voort, 2023) presents a timely opportunity to examine the predicted elemental abundances of galaxies modelled with fewer ad-hoc components than is the case for GCEs. Here we examine the α-Fe planes of a reasonably representative sample of present-day galaxies that form in a high-resolution cosmological hydrodynamical simulation of a periodic volume from the EAGLE project. The EAGLE simulations (Schaye et al., 2015; Crain et al., 2015), and simulations based on the EAGLE model, have been used to explore many related lines of enquiry, including the α-enhancement of massive galaxies (Segers et al., 2016), the α-bimodality of the Milky Way disk (Mackereth et al., 2018a), the radial gradient of oxygen abundances of galaxy discs (Tissera et al., 2019), the α-enrichment of globular cluster populations (Hughes et al., 2020), the chemical composition of satellites accreted early in the Milky Way history (Horta et al., 2021a), and the influence of star formation histories on α-abundances (Gebek & Matthee, 2022).

Our chief aims are the following: *(i)* to establish the physical mechanism responsible for the formation of α knees; *(ii)* to determine whether the α knees are ubiquitous in well-resolved simulated galaxies; *(iii)* to determine what influences the position of the α knee in this chemical space, given the fixed choices of IMF, SN Ia DTD, stellar yields and lifetimes adopted by the simulations; *(iv)* to determine whether the simulations predict the existence of a $[\mathrm{Fe/H}]_{\mathrm{knee}}$-$M_\star$ relation (hereafter, MKR), whose slope and scatter are consistent with observational constraints; and *(v)* to establish the physical processes responsible for the existence of the MKR and its associated scatter.

In §2.2 we describe the simulation and the procedure we use to characterise the α-Fe planes of its galaxies. In §2.3 we characterise the broad properties of the galaxy population in terms of their α-abundance patterns, determine what forms the α knee in the simulated galaxies and then examine the relationship between α knee metallicity and stellar mass. In §2.4 we examine the element abundance evolution inferred by a one-zone GCE model for a fixed star formation history, similar to that of a simulated galaxy that exhibits a knee. We compare the outcomes using i) the constant gas consumption timescale assumed by default by the GCE, and ii) an evolving gas consumption timescale similar to that exhibited by the simulated galaxy, which is initially significantly longer than the default timescale. Using the latter, we find that the GCE closely reproduces

the element abundance evolution of [O/Fe](t) and [Fe/H](t) exhibited by the simulated galaxy. We summarise our findings in §2.5.

2.2 Methods

In §2.2.1 we provide a brief overview of the EAGLE simulation used here. The simulations have been described in detail in many papers, so we present only a brief overview and restrict discussion of the subgrid models to those most relevant to this study. In §2.2.2 we describe how haloes and galaxies are identified. In §2.2.3 we present our method for quantitatively characterising the 'morphology' of the [α/Fe]-[Fe/H] distribution of simulated galaxies.

2.2.1 The EAGLE simulations

The EAGLE simulations (Schaye et al., 2015; Crain et al., 2015) are hydrodynamical simulations of the formation and evolution of galaxies in a ΛCDM cosmogony, adopting the parameters inferred by Planck Collaboration et al. (2014) ($\Omega_0 = 0.307$, $\Omega_b = 0.04825$, $\Omega_\Lambda = 0.693$, $\sigma_s = 0.8288$, $n_s = 0.9611$, $h = 0.6777$ and $Y = 0.248$). The simulation data can be downloaded by the community from an online database, as described by McAlpine et al. (2016). The simulations were evolved using a modified version of the N-body Tree-PM smoothed particle hydrodynamics (SPH) code GADGET-3 (last described by Springel, 2005). The numerical modifications include the pressure-entropy SPH formulation of Hopkins (2013), the time-step limiter of Durier & Dalla Vecchia (2012), and switches for artificial viscosity (Cullen & Dehnen, 2010) and artificial conduction (Price, 2010).

The suite of subgrid models includes element-by-element radiative cooling and heating for 11 species (Wiersma et al., 2009a) and treatment of the ISM as a single-phase medium. Gas particles are subject to a polytropic pressure floor, becoming eligible for stochastic conversion into star particles at a pressure-dependent rate that reproduces the observed Kennicutt (1998b) star formation law (Schaye & Dalla Vecchia, 2008), when the gas becomes denser than a metallicity-dependent density threshold (Schaye, 2004).

Star particles are treated as simple stellar populations (SSPs) with a Chabrier (2003) initial mass function (IMF) between 0.1 and 100 $M_\odot$, whose stars evolve and lose mass

following the model of Wiersma et al. (2009b). This chemodynamics model uses the metallicity-dependent nucleosynthetic yields for massive stars, Type Ia SN, Type II SN and the asymptotic giant branch (AGB) phase (Portinari et al., 1998b; Marigo, 2001) and metallicity-dependent stellar lifetimes (Portinari et al., 1998b).

The 'lifetimes' of SN Ia are specified by an empirically-motivated exponential delay time distribution, such that their rate per unit initial stellar mass is

$$\dot{N}_{\mathrm{SN\ Ia}}(\tau) = \nu \frac{\mathrm{e}^{-t/\tau}}{\tau}, \tag{2.1}$$

where $\nu = 2 \times 10^{-3} \mathrm{M}_{\odot}^{-1}$ is the number of SN Ia per unit initial stellar mass, and $\tau = 2$ Gyr is the characteristic e-folding time. These parameters were calibrated to ensure that the simulations broadly reproduce the observed evolution of the cosmic Type Ia SN rate density (Schaye et al., 2015). The EAGLE DTD implements a metallicity-dependent minimum delay time of $t_{\mathrm{d,\ min}} \approx 40$ Myr (which is consistent with the shortest delay time of Matteucci et al., 2009; by contrast Schaye et al., 2023 set the SN Ia rate to zero below ages of exactly 40 Myr). This metallicity dependence follows from the metallicity dependence of the stellar mass-age relation (Schaller, private communication). It is worth noting that in the GCE modelling community, a longer minimum delay time of $t_{\mathrm{d,\ min}} = 150$ Myr is typically adopted.

Star particles inject feedback energy associated with the evolution and explosion of massive stars by stochastically and isotropically heating neighbouring gas particles by a temperature increment of $\Delta T_{\mathrm{SF}} = 10^{7.5}$ K (Dalla Vecchia & Schaye, 2012). Black holes (BHs) of initial mass $10^5\, h^{-1}\, \mathrm{M}_{\odot}$ are seeded in haloes with mass greater than $10^{10}\, h^{-1}\, \mathrm{M}_{\odot}$, identified on-the-fly with a periodically-triggered friends-of-friends (FoF) algorithm. BHs act as "sink" particles that grow through BH-BH mergers and Eddington-limited Bondi-Hoyle accretion, modulated by the circulation speed of gas close to the BH (Rosas-Guevara et al., 2015; Bower et al., 2017). Feedback energy associated with BH accretion is injected by stochastically and isotropically heating neighbouring gas particles by a temperature increment of $\Delta T_{\mathrm{AGN}} = 10^9$ K (Booth & Schaye, 2009; Schaye et al., 2015).

As our study principally concerns the detailed element abundance patterns of $\lesssim L^{\star}$ galaxies, superior resolution and particle sampling is desirable. We therefore examine the Recal-L034N1034 simulation from the EAGLE suite (first introduced by Bastian et al., 2020), which follows the evolution of a periodic cube of side length $L = 34.4$ cMpc populated with 1034^3 collisionless dark matter particles of mass $m_{\mathrm{DM}} = 1.21 \times 10^6\, \mathrm{M}_{\odot}$,

and an initially equal number of gas particles of initial mass $m_g = 2.26 \times 10^5$ $M_\odot$. The simulation adopts a Plummer-equivalent gravitational softening length of $\epsilon_{com} = 1.33$ ckpc, limited to a maximum proper length of $\epsilon_{prop} = 0.35$ ckpc. The mass (spatial) resolution of the simulation is therefore superior to that of the flagship Ref-L100N1504 by a factor of 8 (2) and, as discussed by Schaye et al. (2015), at this higher resolution it was necessary to recalibrate the efficiency of the subgrid stellar feedback model's parameters in order to achieve a satisfactory reproduction of the present-day galaxy stellar mass function (GSMF). The Recal-L034N1034 simulation used here has a volume of $\simeq 2.6$ greater than the Recal-L025N0752 simulation introduced by Schaye et al. (2015). It also incorporates the E-MOSAICS treatment of star cluster formation and disruption (Pfeffer et al., 2018; Kruijssen et al., 2019a), though we do not examine the properties of star clusters here.

2.2.2 Halo and galaxy finding

Galaxies and the haloes that host them are identified by applying the FoF algorithm to the dark matter particle distribution with a linking length 0.2 times the mean interparticle separation. Gas, star and BH particles are then associated to the FoF group of the nearest dark matter particle. Substructure bound to these haloes is then identified using the SUBFIND algorithm (Springel et al., 2001, Dolag et al., 2008). In each FoF group, the subhalo that contains the most bound particle is designated the central galaxy/subhalo; the other subhalos of the FoF group are satellites. When referring to the aggregated properties of the gas, star, and dark matter particles comprising a galaxy (for example, quantities such as a galaxy's stellar mass, star formation rate or metallicity), we follow Schaye et al. (2015) and compute the properties from particles within a spherical aperture of comoving radius $r = 30$ ckpc centered on the most bound particle. We examine only galaxies with a present day stellar mass of $M_\star > 10^{8.5}$ $M_\odot$, ensuring that galaxies are sampled by $\gtrsim 2000$ star particles.

2.2.3 Characterising simulated α-Fe distributions

We adopt the standard definition of the abundance ratio of elements x and y relative to their Solar abundance ratio:

$$\left[\frac{x}{y}\right] = \log_{10}\left(\frac{X^x}{X^y}\right) - \log_{10}\left(\frac{X^x_\odot}{X^y_\odot}\right), \tag{2.2}$$

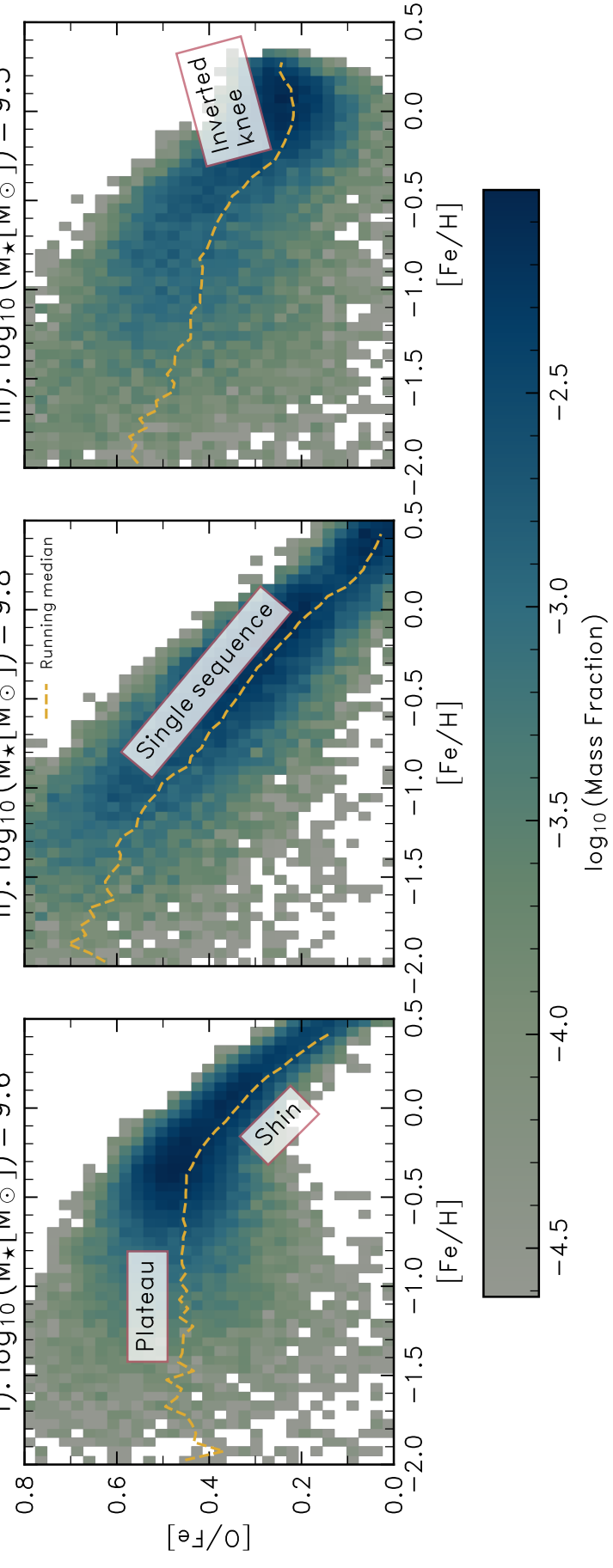

Figure 2.1: The α-Fe planes of three present-day galaxies from the simulation, selected as exemplars of the main categories of α-Fe distribution we find, represented as initial mass-weighted 2-dimensional histograms of stellar abundances. Overlaid dashed yellow curves denote the median of [α/Fe] as a function of [Fe/H]. From left to right, we show *i)* a classical knee, whose α-Fe plane exhibits the canonical plateau-knee-shin morphology, *ii)* a single-slope whose α-Fe plane is characterised by a single declining sequence of [α/Fe] as a function of [Fe/H] and *iii)* an inverted knee, characterised by an initial declining sequence of [α/Fe] as a function of [Fe/H] before a turnover to a positive gradient at high [Fe/H]. A mass fraction of $\log_{10}(f_{\rm bin}) = -3$ corresponds to a stellar mass per pixel of $M_{\star,\rm bin} = (3.6, 6.5, 3.1) \times 10^6$ M$_\odot$ for the left, middle and right panels, respectively.

where $X^x = \sum_i m_i^x / \sum_i m_i$ is the mass fraction of stellar particle i in element x, and m_i and m_i^x are the total mass of the stellar particle, and its mass in element x, respectively. We adopt the Solar abundances of Asplund et al. (2009), in which $X_\odot^{\rm O}/X_\odot^{\rm Fe} = 4.44$. We follow Segers et al. (2016) and use the abundance ratio [O/Fe] as a proxy for [α/Fe], because O dominates the mass fraction of α-elements released by an SSP.

Inspection of the α-Fe planes of the simulated galaxies reveals that there is significant diversity among the galaxy population at $z = 0$. Fig. 2.1 provides illustrative examples of the three main categories of α-Fe plane morphology that we find, from left to right i) galaxies that exhibit the canonical plateau-knee-shin shape, ii) a single sequence of declining [α/Fe] and [Fe/H] and iii) galaxies with an increasing α-element abundances at high [Fe/H]. Overlaid dashed yellow curves denote the median [O/Fe] as a function of [Fe/H], computed in bins of Δ[Fe/H]=0.05. We stress that this median does not necessarily reflect in detail the temporal evolution of the ISM element abundances since, for example, the accretion of a gas-rich progenitor can briefly lower [Fe/H].

The diversity shown in the $z = 0$ galaxy population in Fig. 2.1 illustrates the need for a flexible procedure to quantitatively characterise these α-Fe morphologies. Therefore, we model them as a two-piece piecewise linear function, parameterised as a function $f([{\rm Fe/H}]_{\rm knee},\ [\alpha/{\rm Fe}]_{\rm knee},\ \theta_1,\ \theta_2)$ where θ_1 and θ_2 are, respectively, the slopes of the plateau and the shin component. We define the 'shin' as any sequence of declining α-abundances that follows the high-α plateau of a galaxy, whose stellar particles have [Fe/H] $>$ [Fe/H]$_{\rm knee}$. Hendricks et al. (2014) fitted a piecewise linear function to the abundances of the Sag dSph assuming that their trajectory was consistent with the canonical α-Fe track shown schematically in the review of McWilliam (1997) which comprises a high-[α/Fe] plateau, connected to a low-[α/Fe] plateau at high [Fe/H] by a declining α-shin. However, this parameterisation was made on the assumption that *all* galaxies should show an α knee that conforms to the canonical morphology. The evidence from the Local Group and our initial examination of the simulated galaxies motivates the relaxation of these constraints; both morphologies have been observed in a number of stellar populations in the Local Group. Hayden et al. (2015), Nidever et al. (2020a), Hasselquist et al. (2021b), Horta et al. (2023b), and Fernandes et al. (2023a) provide examples of positive gradients, and Vargas et al. (2013, 2014) provide examples of mono-gradient α-Fe planes. Therefore, we place no restrictions on the signs of the gradients of the two components, nor on the value of the breakpoint in ([O/Fe],[Fe/H]) space that separates them. Thus, we can identify cases where the α-Fe plane shows a declining or increasing trend of [α/Fe] as a function of [Fe/H].

To construct a statistical model of the α-Fe plane of individual galaxies, we use the Python package PYMC3 to fit a piecewise linear model to the data using Bayesian inference. We follow the procedure outlined by Hogg et al. (2010) assuming that there are no measurement uncertainties on the abundances of the simulated galaxies. The best-fitting model is found by maximising the likelihood for the parameters of the piecewise model $O = [[\mathrm{Fe/H}]_{\mathrm{knee}}, [\mathrm{O/Fe}]_{\mathrm{knee}}, \theta_1, \theta_2, \Sigma]$ which we assume takes the form:

$$\ln \mathcal{L}([\mathrm{Fe/H}], [\mathrm{O/Fe}] \mid O) = K - \sum_{i=1}^{N} \left(\frac{\Delta_i^2}{2\Sigma_i^2} + \ln |\Sigma_i^2| \right) \tag{2.3}$$

where Δ_i^2 defines the distance between the i^{th} data point and the model and Σ_i^2 is the variance orthogonal to the model. K is a normalisation constant. We assume that the priors for the model parameters are Gaussian and that the constant scatter term for [O/Fe] at fixed [Fe/H], Σ, is described by a half-Cauchy prior. After minimising the log-likelihood we use this optimal solution to initiate a Markov Chain Monte Carlo (MCMC) sampling of the posterior probability distribution function (PDF) of the parameters O using the No-U-Turn MCMC Sampler (NUTS; Hoffman et al., 2014) as implemented in PYMC3 (Salvatier et al., 2016). This produces an estimate of the posterior PDFs of each parameter from which we take the median values of O. We take the interquartile range of each estimated posterior PDF to be the uncertainty of a given parameter.

Fig. 2.2 shows the 2d initial mass-weighted histogram of the distribution of [O/Fe] vs. [Fe/H] for the classical α knee shown in the left panel of Fig. 2.1, where the piecewise model is overlaid by solid a line. The interquartile range, which is very small, is shown by many transparent yellow curves which show 50 models with parameters drawn randomly from the posterior distributions inferred by the method. For this galaxy we infer a value $[\mathrm{Fe/H}]_{\mathrm{knee}} = -0.24 \pm 0.02$. As we show the running median in Fig. 2.1, it is less sensitive to stellar particles with high [O/Fe] at fixed [Fe/H] and thus appears flatter.

The simulated galaxies can be categorised into the classes illustrated by Fig. 2.1, based on the outcome of our fit to their α-Fe planes: *classical knee* distributions are those for which the fitted piecewise function clearly resembles an α-rich sequence or plateau, and a declining α shin sequence, *single slope* distributions are dominated by a monotonically decreasing sequence of [O/Fe] vs. [Fe/H] with no obvious knee, and *inverted knee* distributions exhibit α-plateaus or even classical knees but transition at relatively high [Fe/H] to a sequence of increasing [α/Fe] as a function of [Fe/H].

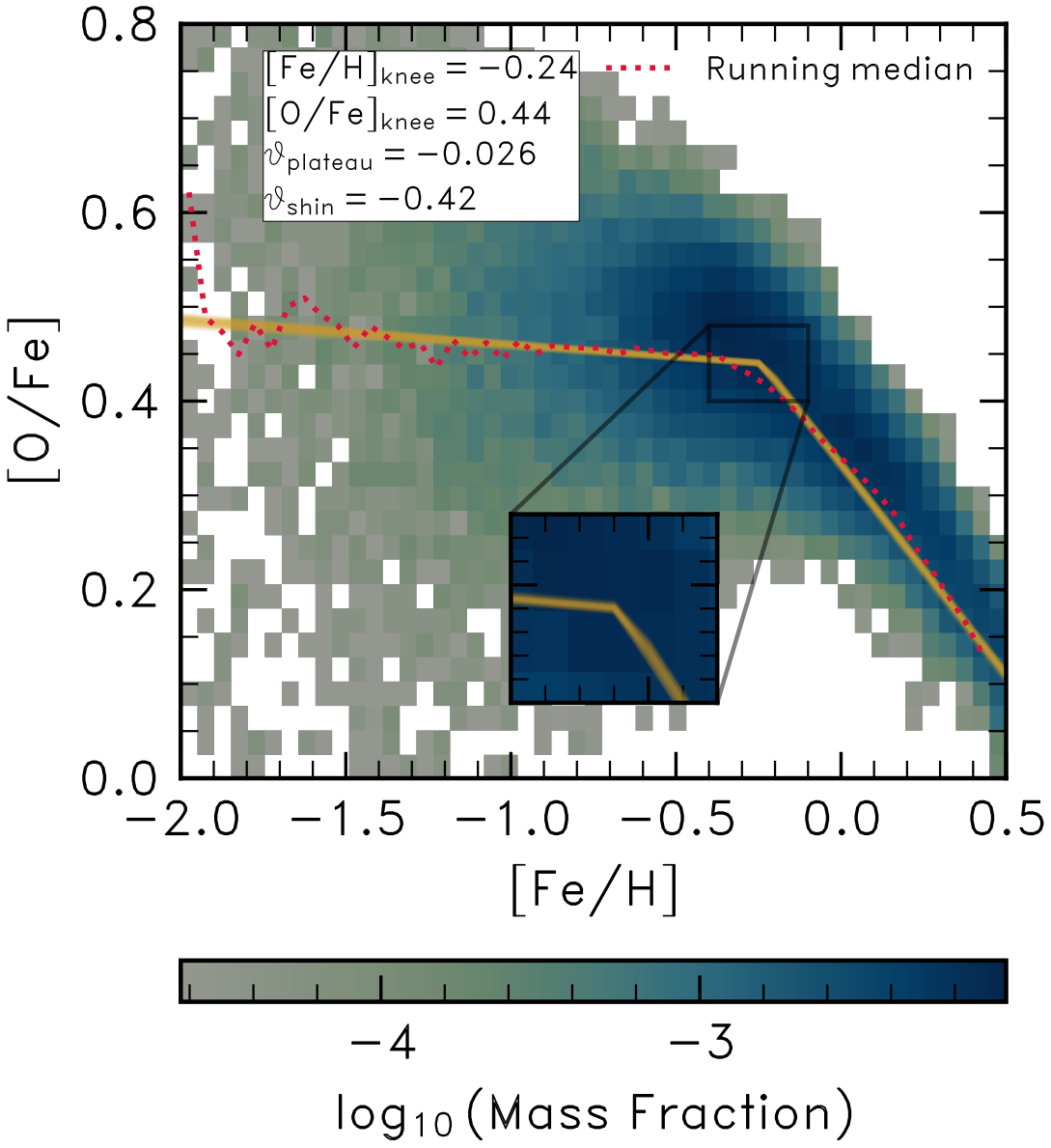

Figure 2.2: The initial mass-weighted histogram of the galaxy exhibiting a classical knee α-Fe distribution shown in panel i) of Fig. 2.1, shown here with the resultant piecewise linear fit determined by linear regression to the data. We superimpose 50 realisations of our piecewise model as sampled randomly from the posterior PDFs of each parameter over the range in [Fe/H], with an inset axis zooming in on $[\mathrm{Fe/H}]_{\mathrm{knee}}$.

For the stellar particles of galaxies with a classical knee, we define the plateau and shin stellar populations as those with [Fe/H] less than, or greater than, $[\mathrm{Fe/H}]_{\mathrm{knee}}$, respectively. This allows us to compute the aggregated properties of the stellar populations which comprise the plateau and shin. In order to select a representative sample of classical knees, we impose the following selection criteria:

1. $\theta_{\mathrm{shin}} + \sigma_{\theta,\ \mathrm{shin}} < \theta_{\mathrm{plateau}}$
2. $\theta_{\mathrm{plateau}} - \sigma_{\theta,\ \mathrm{plateau}} > \theta_{\mathrm{shin}}$
3. $M_{\star,\mathrm{plateau}}/M_{\star,\ \mathrm{total}} > 0.25$
4. $M_{\star,\mathrm{shin}}/M_{\star,\ \mathrm{total}} > 0.25$,

where θ refers to the slope of a component, σ refers to the standard error (measured from the posterior distributions of each parameter) and $\mathrm{M}_{\star,\mathrm{plateau/shin/total}}$ refer to the plateau, shin and total stellar masses. Our criteria for the gradients of each component of the piecewise model and on the masses of the plateau are to ensure that a change in slope and the masses of each component are statistically significant.

Galaxies in the single slope category are selected so that the slopes of the plateau and shin are the same within the measured errors such that:

1. $\theta_{\mathrm{plateau/shin}} \leq 0$
2. $\theta_{\mathrm{shin}} + \sigma_{\theta,\ \mathrm{shin}} > \theta_{\mathrm{plateau}}$
3. $\theta_{\mathrm{plateau}} - \sigma_{\theta,\ \mathrm{plateau}} < \theta_{\mathrm{shin}}$,

are satisfied.

2.3 Results

In order to gain insight into the physics responsible for α knee formation, we contrast the properties of galaxies that exhibit classical knees with those having a single slope α-Fe morphology. In §2.3.1, we characterise quantitatively the galaxies' α-Fe distributions. In §2.3.2, we examine their star formation and chemical enrichment histories, in order to

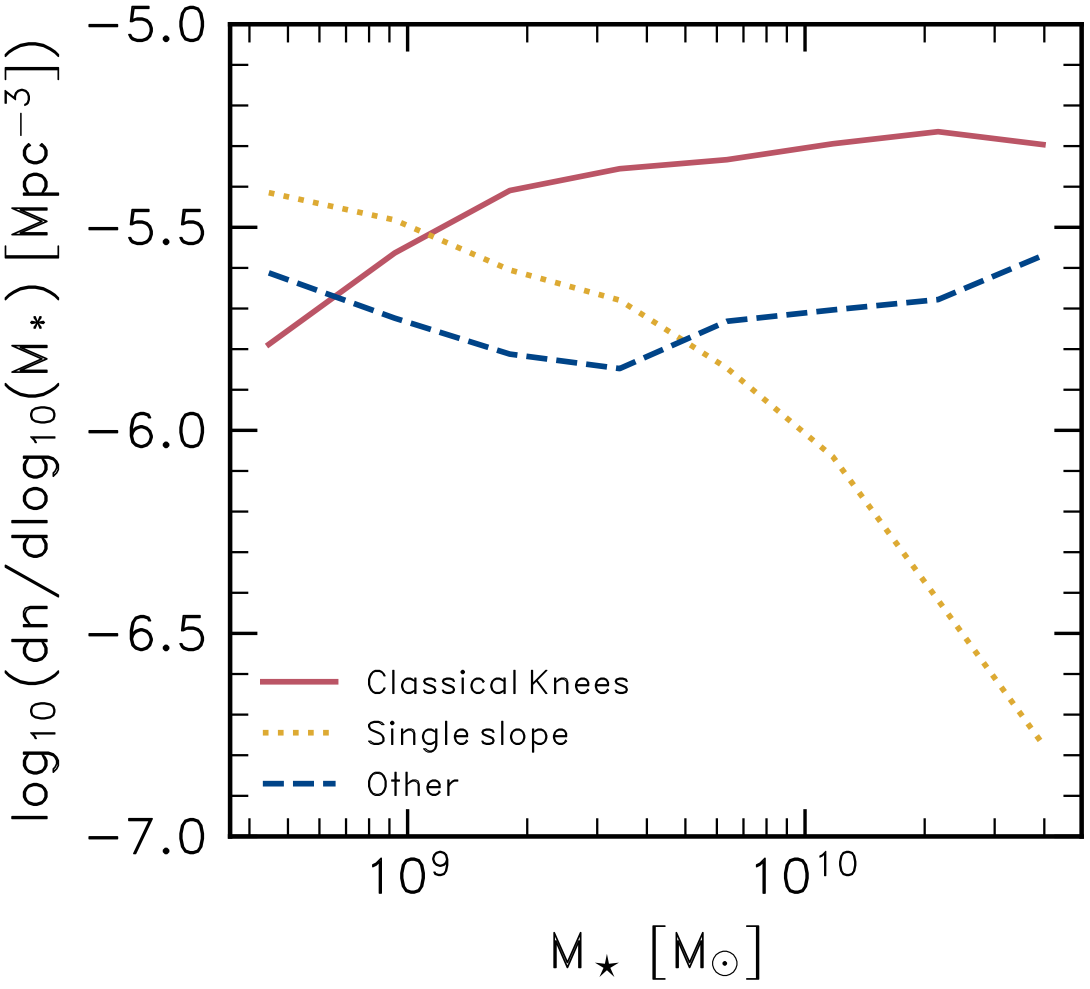

Figure 2.3: The fractions of the present-day galaxy population in the simulation, as a function of galaxy stellar mass, whose α-Fe distributions are categorised as 'single slope', 'classical knee' or 'other'. At low mass, most of the galaxy population does not exhibit classical knees, but as $M_\star$ increases the fraction of single slopes decreases, with that of classical knees commensurately increasing. The fraction of bimodal, inverted knees and unclassified galaxies is largely insensitive to stellar mass.

identify mechanisms responsible for their markedly different α-Fe distributions. Finally, in §2.3.3 we validate the simulation's outcomes via a comparison to observations of stellar populations in the Local Group, focusing on the slope of the relationship between $[\mathrm{Fe/H}]_{\mathrm{knee}}$ and $M_\star$ (dubbed 'MKR' – $\boldsymbol{M_\star}$-$[\mathrm{Fe/H}]_{\mathbf{knee}}$ **r**elationship) and its scatter.

2.3.1 A census of classical knees and single slopes in the simulated galaxy population

Application of the criteria described in §2.2.3 yields 540 simulated galaxies with classical knees, 310 with single α-Fe slopes and 241 whose α-Fe planes cannot be simply described by a two-piece piecewise linear function. The latter category includes both inverted knees and galaxies that exhibit α-bimodality (a phenomenon that in this simulation is only seen at $M_\star \gtrsim 10^{10}$ M$_\odot$; Mackereth et al., 2018a), which together account for ≈ 30 percent of galaxies, irrespective of galaxy mass. Although the classical knees represent just under half the overall sample, there is a significant mass dependence: Fig. 2.3 reveals that for $M_\star \lesssim 10^9$ M$_\odot$ the dominant category of galaxy is, marginally, the single-slopes, with the fraction of galaxies exhibiting classical knees increasing monotonically with $M_\star$.

Fig. 2.4 shows the distribution of the gradients of the sequences recovered from our characterisation of the α-Fe planes of the simulated galaxies: that of the overall sequence in single-slope galaxies, and those of the plateau and shin components of classical knee galaxies. For the latter, we find typical ratios in the gradients of the two sequences of a factor $\simeq 2$. The plot also reveals that the typical gradient of the overall sequence in single-slope galaxies is similar to that of the plateau, and not that of the shin of classical knee galaxies.

These results are in conspicuous contrast to predictions of chemical evolution models in which early evolution results in a horizontal plateau at the [α/Fe] value corresponding to the IMF-averaged yield of Fe and α-elements resulting from *pure* SN II enrichment (e.g. Thomas et al., 1998). In that idealised case we would expect $\theta_{\rm plateau} = 0$. The clear difference between the slopes of plateaus and shins is a signature of differing modes of chemical enrichment. Thus, we can immediately infer that in spite of these galaxies having extended histories of star formation, the formation of single-sloped galaxies must in some way resemble that of high-α plateaus. This would then imply that the occurrence of α-knees and the extent of the plateau in [Fe/H] are not related solely to the form of the DTD.

We are thus left with two conclusions to draw from Fig. 2.3 & Fig. 2.4. Firstly, Fig. 2.3 indicates that the single-sloped galaxies are reasonably common in the simulated galaxy population, particularly at low mass. Secondly, recalling that the EAGLE model adopts a SN Ia DTD with a very short minimum delay time, we nevertheless find that more than half of the simulated galaxies exhibit Fe-rich α-knees. Such α knees therefore cannot be

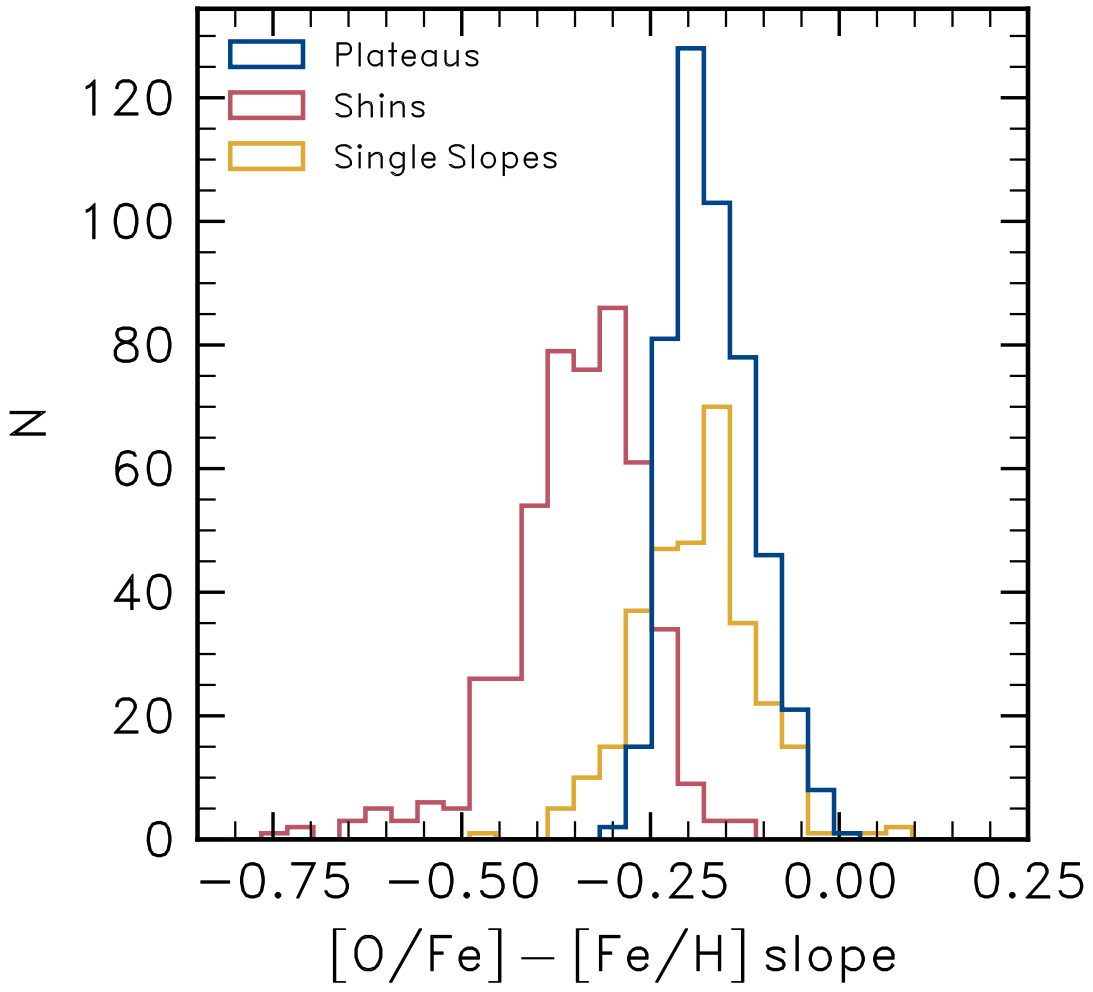

Figure 2.4: Histogram showing the characteristic slopes of *i)* α plateaus, *ii)* α-shins and *iii)* single-sloped α-Fe planes. The distributions of these parameters show that the characteristic slope of the plateau is not close to zero - such slopes are rare in the simulation. Furthermore the slopes of α-plateaus and single slopes seem to be consistent, indicative of them having similar enrichment histories. However, the shins of classical knees are sharply declining by comparison.

solely caused by the onset of SN Ia. Bearing in mind that α-plateaus and single slopes may have similar origins, we turn to the formation histories of classical knees and single slopes in the next sub-section, with the aim of identifying the physical driver(s) of their α-Fe plane differences.

2.3.2 The formation of α-Fe knees

In this sub-section, we compare the star formation and element abundance histories of classical knees and single-sloped galaxies. The chief motivation is to establish why the former exhibit a change in gradient in the [O/Fe]-[Fe/H] relation while the latter do

not, and in particular to scrutinise the orthodox interpretation that α-knees form as a consequence of the *onset* of SN Ia, whether this onset is defined by the minimum delay time or the e-folding timescale.

2.3.2.1 The star formation histories of galaxies with classical knees and single slopes

Fig. 2.5 shows the history of star formation and element abundance evolution of classical knees and single slopes. All evolutionary tracks are computed in 0.3 Gyr bins between $z = 20$ to $z = 0$ ($t \simeq 0$ to $t \simeq 13.8$), where instantaneous abundance ratios reflect the median abundances of newly-formed stellar particles in that interval. The solid yellow curves in the top panels correspond to the median star formation histories (SFHs) of the classical knee and single slope samples (left and right panels, respectively). As our sample comprises galaxies with present-day stellar masses spanning $\simeq 2.5$ dex, we normalise the star formation rates by the present day stellar mass. This yields a quantity with unit Gyr^{-1}, but we stress that this is not the same as the specific star formation rate for $z > 0$. The shaded regions encompass the interquartile range of the SFHs. The SFHs of galaxies with classical knees are characterised by a steady increase to a peak of short duration: averaged over all classical knees in our sample, the peak occurs at $t \simeq 7.5$ Gyr but, owing to cosmic downsizing (e.g. Cowie et al., 1996; Qu et al., 2017), the peak tends to be found earlier (later) for more (less) massive galaxies. Following the peak, the SFH experiences a sustained decline to the present day. Conversely, single-sloped galaxies exhibit SFHs that rise more steadily and remain reasonably constant over a Hubble time.

The dotted lines in the top panels show the ratio between the ongoing SFR (i.e., at time t, averaged over the preceding 300 Myr), and the past average SFR up until that time. We denote this quantity χ. The relative rates of SN II and SN Ia reflect the ratio of current-to-past histories of star formation (Gilmore & Wyse, 1991a). Thus a declining value of $\chi(t)$ indicates that evolved stellar populations are becoming more relevant to the chemical evolution, and a value of $\chi < 1$ implies that evolved stellar populations are beginning to dominate the chemical enrichment of Fe. In Fig. 2.5 we see that when the peak occurs in the classical knee SFH plot, $\chi(t)$ drops below unity while the approximately constant SFR of the single slopes results in a track of $\chi(t) > 1$ at all times.

The grey shaded region enclosed by dashed vertical lines in the left panels denotes the typical time at which the α knee forms for these galaxies, t_{knee}, measured directly from

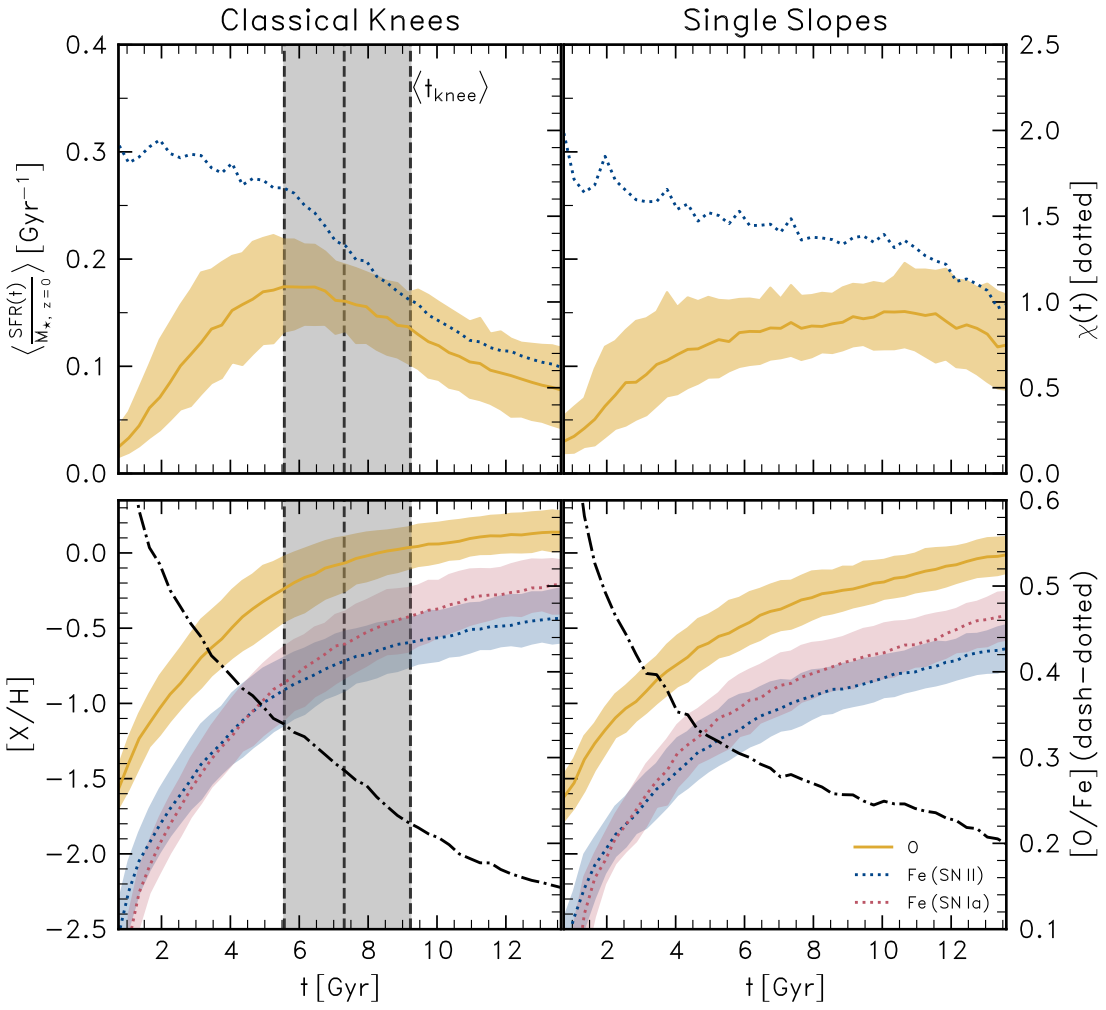

Figure 2.5: The star formation (top) and chemical enrichment (bottom) histories of galaxies exhibiting classical knees (left) and single slopes (right). The median star formation rate as a function of cosmic time is shown normalised by the present-day galaxy stellar mass, to compress the dynamic range. In the left panels the average time at which the α knee forms is denoted by a black dashed line, with the shaded area representing the interquartile range. The bottom panels show the evolution of [O/H] and [Fe/H], the latter decomposed into the contribution from SN II and SN Ia which are explicitly tracked in the simulations. The evolution of [O/Fe] is shown, relative to the right-hand axis, with a dashed-dotted line. Clear differences in star formation and chemical enrichment histories of the two categories of galaxy are evident. The SFHs of classical knees are characterised by a steep initial SFR increase followed by a decline around $t \simeq 6$ Gyr. At the time of α knee formation, $[\mathrm{Fe/H}]_{\mathrm{SN\ II}}$ begins to plateau, whereas $[\mathrm{Fe/H}]_{\mathrm{SN\ Ia}}$ is increasing. The dotted lines in the top panels denote the instantaneous SFR divided by the past mean SFR (right y-axis). The time at which this track drops below unity coincides broadly with the formation of the α knee. The formation of the α knee is *not* associated with merely the onset of SN Ia but rather the contribution of SN II diminishing as the SFR(t) declines.

the time at which [Fe/H](t) crosses $[\mathrm{Fe/H}]_{\mathrm{knee}}$. We see that it generally occurs $\simeq$ 2 Gyr after the peak SFR is reached. Therefore, the formation of the α knee generally precedes the time at which χ first drops below unity, which is highly suggestive that evolved stellar populations begin to dominate the Fe-enrichment of the ISM during the evolution of the "shin" phase. Recalling that the EAGLE model implements R_{Ia} with a short (40 Myr) minmum delay time and e-folding timescale of 2 Gyr, it is clear that the formation of the α knee cannot be attributed to the 'onset' of SN Ia beginning to contribute to the chemical enrichment, whether this is defined as the minimum delay time or the e-folding timescale of the DTD.

2.3.2.2 The effects of differing SFHs on galaxy element abundance evolution

The curves in the bottom panels of Fig. 2.5 show the evolution of the characteristic element abundances of new stellar populations, as a function of cosmic time, in the two categories of galaxy. The panels show the oxygen abundance [O/H] (solid yellow curves), and the iron abundances contributed separately by the two types of SN tracked by the simulation ($[\mathrm{Fe/H}]_{\mathrm{SN\ II}}$, dotted blue curves) and SN Ia ($[\mathrm{Fe/H}]_{\mathrm{SN\ Ia}}$ dotted red curves). For reference, the α-richness of new stellar populations is shown, relative to the right-hand axis, with a dot-dashed line.

The differing star formation histories of the classical knee and single slope galaxy populations impact the evolution of their iron abundances. In single slope galaxies the relative contribution of SNe Ia and SNe II to the Fe abundance of newly-formed stars is fairly constant, as indicated by the red and blue dotted tracks in the bottom right panel of Fig. 2.5, remaining parallel after $t \simeq 6$ Gyr. In classical knee galaxies, following the peak of the SFR, the fractional contribution of SNe II to the iron abundance of newly-formed stars declines, as indicated by the flattening of the dotted blue curve. In contrast, SNe Ia continue to contribute significantly, as their ongoing rate does not react promptly to the decline of the SFR. Over the course of several Gyr, the $[\mathrm{Fe/H}]_{\mathrm{SN\ Ia}}$ and $[\mathrm{Fe/H}]_{\mathrm{SN\ II}}$ curves therefore diverge, leading to the steady evolution of the gradient of the median track through [α/Fe]-[Fe/H] space, from that of the plateau to that of the shin. The differing behaviour can be quantified via the gradient of the ratio $[\mathrm{Fe/H}]_{\mathrm{SN\ Ia}}/[\mathrm{Fe/H}]_{\mathrm{SN\ II}}$, which we measure in the 2 Gyr period centered on t_{knee} (defined for the classical knee sample). The values are, respectively, 0.027 ± 0.005 dex Gyr^{-1} and 0.015 ± 0.003 dex Gyr^{-1}.

It is worth noting that although the Fe locked up in stars born at early epochs is contributed primarily by SNe II, in both categories of galaxy the bulk of the Fe was synthesised by SNe Ia. This is despite EAGLE adopting a yield set for which SNe Ia contribute slightly less than half of the Fe synthesised by evolved stellar populations. We attribute this apparent discrepancy to the preferential ejection of SN II nucleosynthetic products from the ISM in feedback-driven outflows, and remark that this effect may help to exacerbate the divergence of the $[\mathrm{Fe/H}]_{\mathrm{SN\ II}}$ and $[\mathrm{Fe/H}]_{\mathrm{SN\ Ia}}$ curves: ongoing star formation in single slope galaxies ensures that Fe synthesised by SNe Ia is released into an ISM that is in effect always experiencing SNe II-driven outflows, whilst in classical knee galaxies the early decline of the SFR ensures that a significant fraction of Fe synthesised by SNe Ia is released into an ISM without strong outflows, aiding its retention by the galaxy.

Based on Fig. 2.5, it is clear that classical knees and single slopes are distinguished by their differing star formation histories. The peaked star formation histories of classical knees should therefore yield a narrower spread of stellar ages in comparison to those resulting from the relatively constant SFR of the single slope galaxies. We measure the age spread of the stars in the two types of galaxies by equating it to the interquartile range of a galaxy's stellar ages. The resulting histograms (normalised by the total number of galaxies in each category) are plotted in Fig. 2.6. The plot shows that as a consequence of their extended SFHs, single slope galaxies indeed tend to have larger age spreads: on average 5.4 Gyr as opposed to the 4.2 Gyr of classical knees. We perform a two-sample Kolmogorov-Smirnov test and, obtaining a value of $p \ll 0.05$, reject the null hypothesis that the age spread distributions are drawn from the same parent distribution. Consequently, we conclude that, in principle, the presence of an α knee could be inferred in a galaxy in so far as such an age spread can be constrained observationally for the unresolved stellar populations of more distant systems.

2.3.2.3 Implications for the emergence of α knees

It is widely assumed that the α knee is caused by the *onset* of SN Ia contributing significant Fe mass to the ISM (e.g., Tinsley, 1979; Gilmore & Wyse, 1991a). Indeed, an early α knee, following a horizontal plateau at very low [Fe/H] *may* appear following the very first SN Ia explosions, though this may not be the case depending on how strong the metallicity dependence of SN II nucleosynthetic yields is. However, the more significant α knees identified in our simulated galaxies are located at sufficiently high

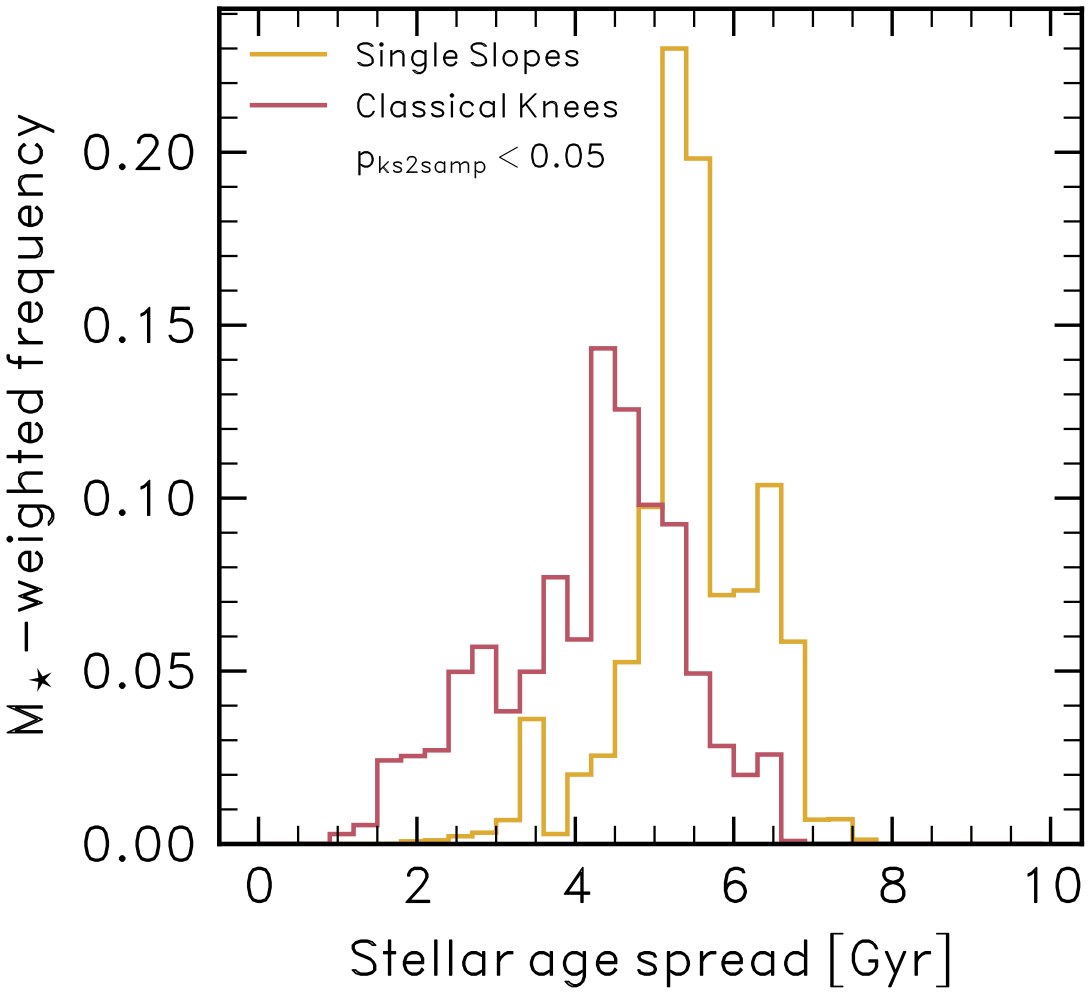

Figure 2.6: The characteristic age spread (i.e. interquartile range) of the stellar populations comprising simulated galaxies that exhibit α−Fe planes with a single slope (green) and that exhibit classical knees (red). As one might expect on the basis of Fig. 2.5, the single slope distribution shows a peak at a characteristically greater spread in stellar ages than that of the classical knees. An observational signature of the α knee, then, might be a stellar age spread which could be measured via stellar population synthesis using the integrated light of unresolved stars.

metallicity that their formation cannot be associated with the emergence of such early SN Ia events.

Our explanation for the emergence of α knees is well aligned with suggestions made in previous work. Tolstoy et al. (2009) has qualitatively argued that the α knees seen in the chemical abundances of the LGDs could originate from a decline in their SFRs, and further suggested that due to their low masses dwarf galaxies are particularly susceptible to sudden events reducing their SFRs. The rate of enrichment by SN II reacts more promptly to this decline than the rate of enrichment by SN Ia, due to a combination of the short lifetime of massive stars and the time dependence of the SN Ia DTD, which

evolves on gigayear timescales. The SN II progenitors with the longest lifetimes are shorter-lived than the typically adopted minimum delay time for the SN Ia DTD.

Our finding has also been anticipated in the work by Maoz & Graur (2017). Those authors convolved the cosmic SFH of Madau & Fragos (2017) with a power-law parameterisation of the SN Ia DTD and re-estimated the SN Ia rate density under the assumption of a Kroupa (2001) IMF. They used these forms of the SFH and DTD to compute the mean α and Fe accumulation history that results from the cosmic SFH. The evolutionary tracks of [α/Fe] and [Fe/H] produced by this model yield an α-plateau that gently declines until $z \lesssim 2$ whence an α knee forms due to a combination of the steep decline of the cosmic SFR (thus reducing the SN II rate) and the shallower decline of the SN Ia rate due to the power-law tail of the DTD. By contrasting Fig. 3 of Schaye et al. (2015) to Fig. 1 of Maoz & Graur (2017), which show model SN Ia rate densities compared to the same set of DTD measurements, we can see that this behaviour is qualitatively mirrored by the exponential DTD of the EAGLE simulations.

To summarise, in the simulation examined here the formation of an α knee is neither ubiquitous nor associated merely with the onset of SN Ia enriching the star-forming gas of a galaxy. Instead, a distinct change of gradient in the α-Fe plane is associated with a decline in the SFR, which brings about a transition from chemical enrichment being dominated by young stellar populations to old stellar populations. As a natural consequence, we find that single slopes host on average younger stellar populations with a wider spread in age than their classical knee counterparts.

2.3.3 The $[\mathrm{Fe/H}]_{\mathrm{knee}}$-$M_\star$ relation

Having determined how the α knee forms in the simulated galaxies, we now turn to the relationship between the metallicity of the α knee ($[\mathrm{Fe/H}]_{\mathrm{knee}}$) and total stellar mass ($M_\star$) of this subset of galaxies. We term this relationship the 'MKR' (Mass-Knee metallicity Relation), and compare it on a quantitative basis to that measured using spectroscopic abundances and stellar mass estimates for the stellar populations comprising the galaxies of the Local Group. We then examine the origin of the $\Delta[\mathrm{Fe/H}]_{\mathrm{knee}} \simeq 0.8$ scatter at fixed $M_\star$ that emerges in the simulation, and discuss it in the context of the LGD observations.

In the top panel of Fig. 2.7 we show the MKR of the present-day simulated galaxies. We find a monotonically increasing relation between $[\mathrm{Fe/H}]_{\mathrm{knee}}$ and $M_\star$. We compute

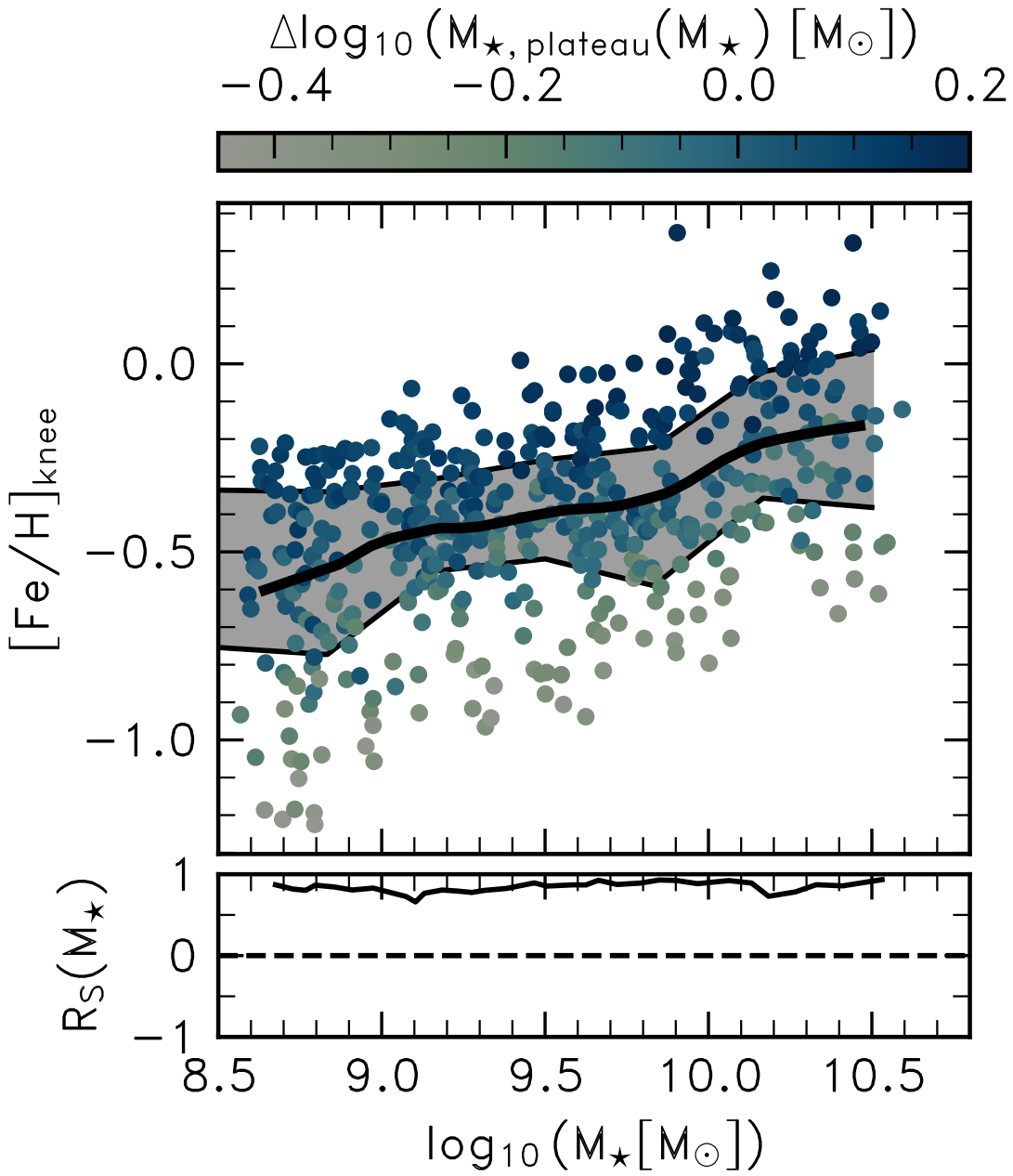

Figure 2.7: Scatter plot of the relationship between the α knee metallicity, $[\mathrm{Fe/H}]_{\mathrm{knee}}$, and the stellar mass of classical knee galaxies (the 'mass - knee metallicity relation'). Each circle symbol represents an individual simulated galaxy. The black curve and grey shared region denote, respectively, the binned median and interquartile range of $[\mathrm{Fe/H}]_{\mathrm{knee}}$ as a function of $M_\star$. Symbols are coloured by the residuals of the relationship between $M_\star$ and $M_{\star,\,\mathrm{plateau}}$ in moving windows of 'fixed' $M_\star$. This shows that at fixed $\mathrm{M}_\star$ there is a correlation between $[\mathrm{Fe/H}]_{\mathrm{knee}}$ and $M_{\star,\,\mathrm{plateau}}$ which means that the scatter in the relationship is driven by variation in how long the star formation rate is rising, forming the plateau. The inset-axis shows the moving Spearman rank correlation coefficient (R_S) of the variables in moving windows of $M_\star$.

the Spearman rank correlation coefficient, R_S, for the MKR and find it has a value is $R_S = 0.44$, indicating that $[Fe/H]_{knee}$ is on average higher in galaxies with greater $M_\star$, consistent with the observed trend (e.g. Tolstoy et al., 2009) for the LGDs. This correlation is also in qualitative agreement with the M_V-$[Fe/H]_{knee}$ relation presented by Hendricks et al. (2014) for seven (Sagittarius dSph, Fornax, Sculptor, Ursa Minor, Carina, Draco and Hercules) of the LGDs. It is also noteworthy that the simulated MKR is characterised by strong scatter in $[Fe/H]_{knee}$ at fixed $M_\star$, in agreement with observational evidence showing that some of the LGDs exhibit significantly low knee metallicities for their stellar masses (e.g., Fornax & the UMi dSph; Hendricks et al., 2014, and the Magellanic Clouds; Nidever et al., 2020a).

2.3.3.1 The origin of scatter in $[Fe/H]_{knee}$ at fixed stellar mass

Symbols in Fig. 2.7 are colour-coded by the residuals for each galaxy about the median relation between $M_{\star,plateau}$ and $M_\star$, calculated non-parametrically using local-weighted scatterplot smoothing (LOWESS; Cleveland, 1979a). $M_{\star,plateau}$ is computed by taking the sum of the stellar masses of star particles with $[Fe/H] < [Fe/H]_{knee}$ in a given classical knee, reflecting the amount of stellar mass that built up prior to the formation of the shin. This information illuminates the origin of the scatter about the MKR (Fig. 2.7. The $M_{\star,plateau} - M_\star$ correlation is unsurprisingly very strong (R_S=0.96), with a typical scatter of $\simeq 0.24$ dex at fixed $M_\star$. The value for the residual indicates whether a galaxy has a high ($\Delta \log_{10} M_{\star,plateau} > 0$) or low ($\Delta \log_{10} M_{\star,plateau} < 0$) plateau mass relative to its similarly-massive counterparts.

The vertical stratification of the symbol colours at fixed $M_\star$ is indicative of a strong positive correlation between $[Fe/H]_{knee}$ and $M_{\star,plateau}$. The lower panel quantifies this correlation, by showing R_S computed for sub-samples within moving bins of $M_\star$ (prior applications of this method can be found in the studies of Davies et al., 2019, 2020). A strong, positive correlation is returned with high significance ($p \ll 0.01$) at all $M_\star$. Galaxies with a high knee metallicity for their stellar mass therefore tend to have a higher plateau mass. Whilst this correlation alone does not denote a causal relation between the two, one can reasonably conclude that the relationship is causal based on Fig. 2.5, from which we established that the α knee forms in response to the decline of the SFR, so that the plateau comprises stars formed prior to the SFR peak and the ensuing α knee formation. Consequently, the Fe synthesised prior to the formation of the α knee was synthesised by stellar populations comprising the plateau, so it is

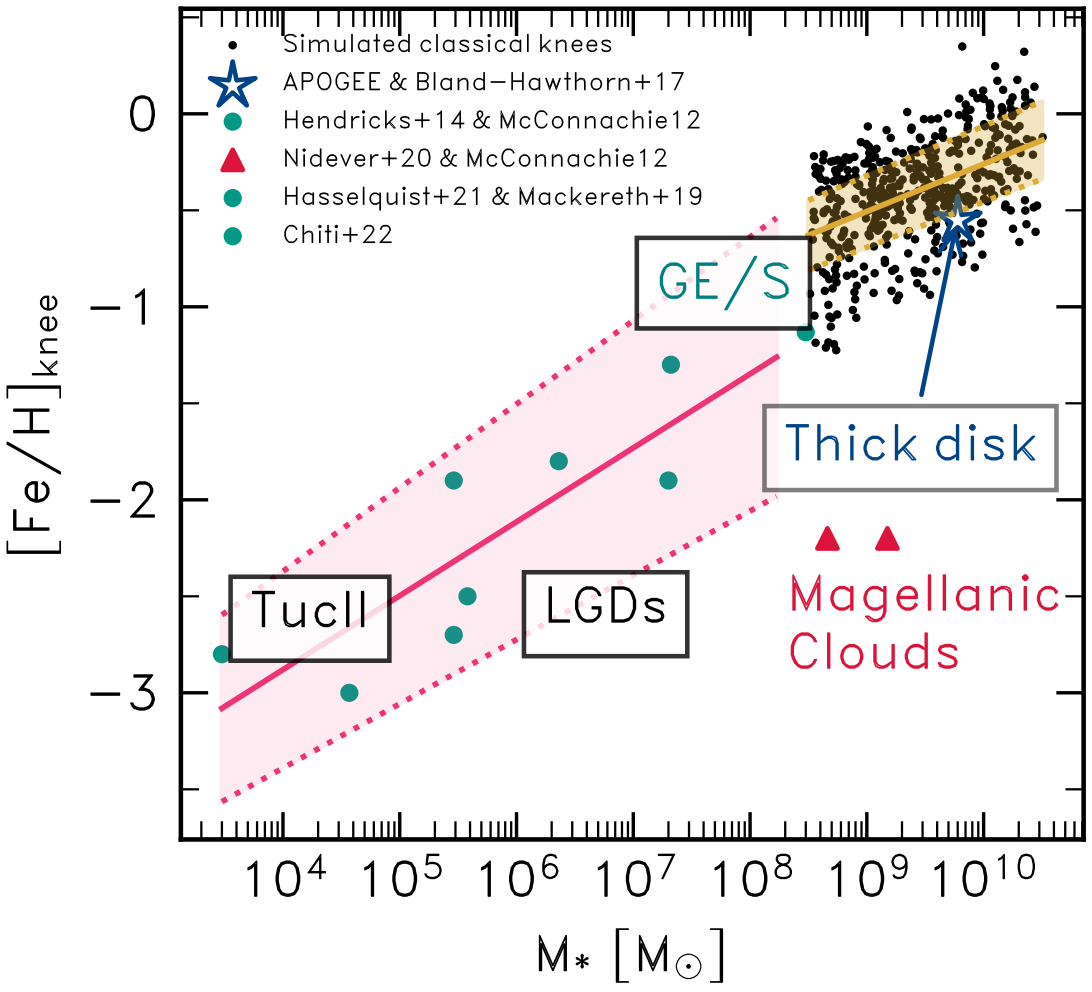

Figure 2.8: Scatter plot of $[\mathrm{Fe/H}]_{\mathrm{knee}}$ as a function of stellar mass for the simulated galaxies that exhibit a classical knee distribution, in addition to observationally inferred measurements of Local Group dwarf galaxies. It shows that the slope of the simulated MKR corresponds closely to that of the observational data. The simulation also exhibits a scatter in $[\mathrm{Fe/H}]_{\mathrm{knee}}$ at fixed $M_\star$ in agreement with the observations. In the exceptional cases of the Magellanic Clouds, which exhibit strongly non-monotonic behaviour on the α-Fe plane, it is known that they underwent recent starbursts associated with their infalling onto the MW halo and thus we cannot truly consider them to belong to our category of classical knees.

unsurprising that $[\mathrm{Fe/H}]_{\mathrm{knee}}$ correlates more strongly with $M_{\star,\mathrm{plateau}}$ ($R_S = 0.64$) than with $M_\star$ ($R_S = 0.44$).

There is ample observational evidence from MZR studies for a secondary dependence of the metallicity of galaxies on the SFR (among other properties) which drives scatter in the MZR at fixed $M_\star$. At fixed $M_\star$, galaxies with higher SFRs tend to have lower metallicities - this is referred to as the fundamental metallicity relation (FMR; Ellison et al., 2008; Mannucci et al., 2010; Bothwell et al., 2013; Salim et al., 2014; Curti et al.,

2020). EAGLE also reproduces this anti-correlation at fixed $M_\star$ (e.g. De Rossi et al., 2017), and it is intriguing that we see a similar anti-correlation between $M_{\star,\mathrm{plateau}}$ and $[\mathrm{Fe/H}]_{\mathrm{knee}}$ at fixed $M_\star$. Although a detailed exploration of the relationship between the MKR and other canonical metallicity scaling relations is beyond the scope of this work, we highlight this as a potential avenue for future efforts.

2.3.3.2 Comparing the simulated MKR to that of the Local Group dwarf galaxies

It is common in the literature for the stellar masses of dwarf galaxies to be "predicted" from their metallicity distribution functions (MDFs; typically represented by the distribution of [Fe/H]), calibrated against the mean MZR (for example that measured by Kirby et al., 2013; see Carrillo et al., 2023). Measurement of the true mean metallicity, Z, of a resolved galaxy requires measurements for an unbiased and representative sample of stars, which is at best very costly observationally. For any galaxy where the presence of a plateau, α knee and subsequent shin has been observed in chemical data, the MKR could be used in principle to estimate the total stellar mass of a galaxy, although there is currently a significant lack of measurements for galaxies with mass $\leq 10^8$ $\mathrm{M}_\odot$, and the scatter in the MKR makes this exercise uncertain.

In Fig. 2.8 we display on the MKR plane the 30 kpc aperture stellar masses and fitted values of $[\mathrm{Fe/H}]_{\mathrm{knee}}$ for our classical knee sample and observational data for LGDs (including the Magellanic Clouds) as well as the debris of the Gaia-Enceladus/Sausage accreted system, and the Milky Way high-α disk. We use the LGD mass measurements presented by McConnachie (2012), the thick disk mass estimate of Bland-Hawthorn & Gerhard (2016) and the Gaia-Enceladus/Sausage (GE/S) mass estimate of Mackereth et al. (2019a). For the low-mass LGDs we adopt the α knee metallicities of Hendricks et al. (2014), for the Magellanic Clouds (MCs) we use the α knee metallicity estimated by Nidever et al. (2020a) while for GE/S and the Milky Way thick disk we apply the method outlined in 2.2.3 on the data from APOGEE. We also include the stellar mass and knee metallicity determined for the dwarf Tucana II from Bechtol et al. (2015) and Chiti et al. (2022). The data for GE/S stars come from Hasselquist et al. (2021b) and the thick disk sample originates from Kisku et al. (in prep).

The running median of $[\mathrm{Fe/H}]_{\mathrm{knee}}$ as a function of $M_\star$ is apparently higher in the simulations than is inferred from the corresponding observations. There are other examples of apparent discrepancies between observed metallicity scaling relations and those originating from cosmological SPH simulations. For example, see the discussion

of Nelson et al. (2018) regarding the MZR in the IllustrisTNG simulations (Weinberger et al., 2017; Pillepich et al., 2018).

However, Fig. 2.8 shows that the slopes of the simulated and Local Group MKRs agree with one another, showing a monotonically increasing trend over the entire mass range sampled. A simple linear regression on each data set yields respective slopes of 0.246 ± 0.077 dex $\log_{10}(\mathrm{M}_\odot)^{-1}$ and 0.385 ± 0.239 dex $\log_{10}(\mathrm{M}_\odot)^{-1}$ with the observed relation being very uncertain due to the limited number of data points. We omit the Magellanic Clouds on the basis that even a cursory look at the data (for example, see Nidever et al., 2020a, 2021; Hasselquist et al., 2021b) reveals that they fall under our category of 'inverted knees'. Although they may exhibit a classical knee at the metal-poor end, the bulk of their populations on the α-Fe plane are characterised by a declining-α plateau at low [Fe/H], turning over to an increasing α-shin, likely caused by a recent burst of star formation.

2.4 A comparison of simulated galaxy abundances with those predicted by a GCE

Our explanation of the origin of the knee in α-Fe space differs from the orthodox interpretation. The latter is primarily motivated by the outcomes of galactic chemical evolution (GCE) models, which adopt a broadly similar set of prescriptions for the behaviour with cosmic time of gas inflow and outflow rates, and the gas consumption timescale. The differing physical origin of α-knee formation that one infers from analysis of the simulation and GCE models therefore warrants further investigation.

We argued in §2.3 that the star formation history is a distinguishing characteristic of galaxies that exhibit classical knees in the simulation. We therefore examine the element abundance evolution inferred by the VICE one-zone GCE model (Johnson & Weinberg, 2020; Johnson et al., 2021a; Griffith et al., 2021) for a fixed star formation history, which we choose to be that of an exemplar classical knee galaxy ($M_\star = 10^{9.60}$ $\mathrm{M}_\odot$) identified in the simulation. We compare the outcomes using i) the constant gas consumption timescale, $t_\mathrm{g} = 1$ Gyr, assumed by default by the GCE, and ii) an evolving gas consumption timescale similar to that exhibited by the simulated galaxy, which we find to be significantly longer at early cosmic epochs than the default gas consumption timescale assumed by VICE.

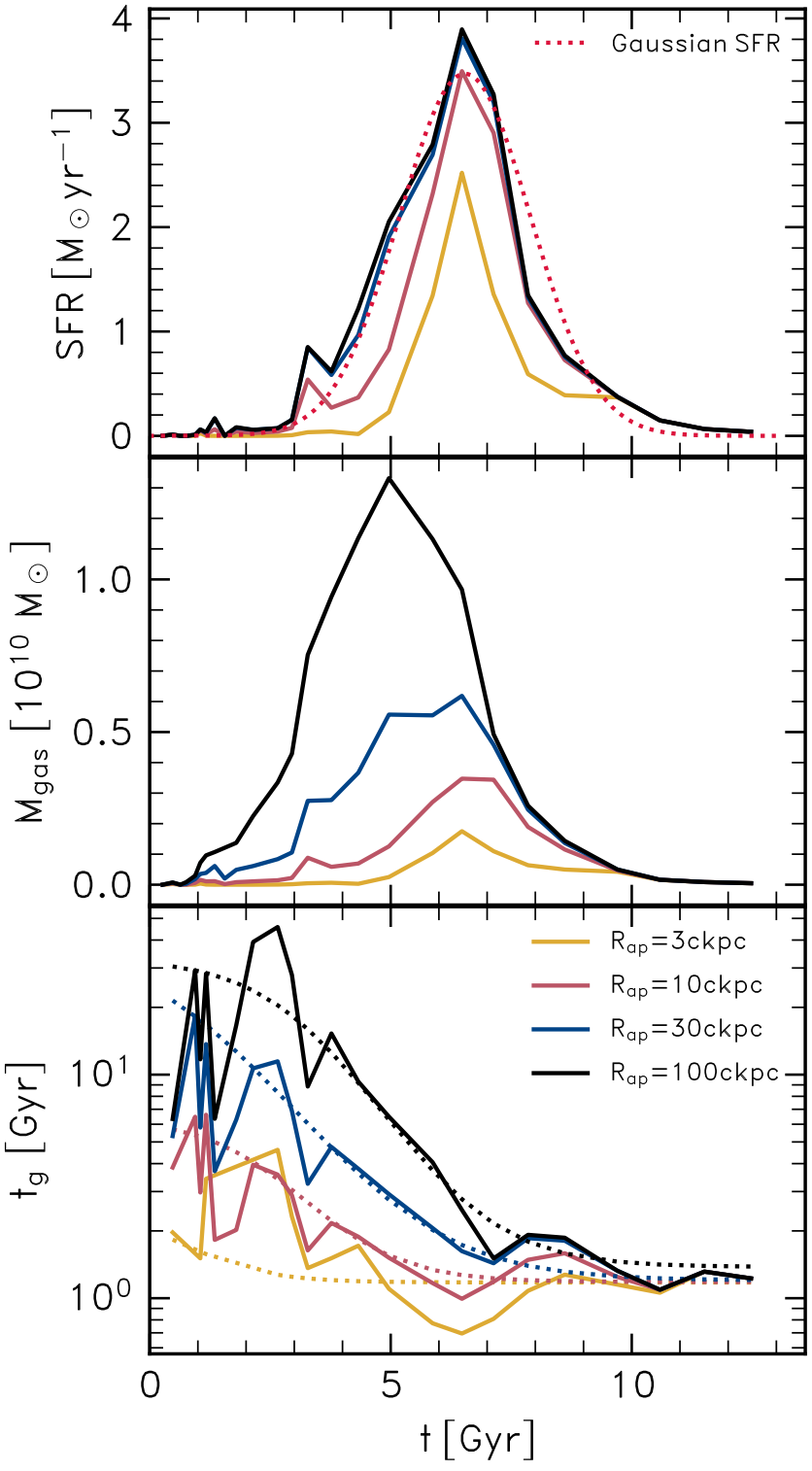

Figure 2.9: The temporal evolution of the star formation rate (top panel), gas reservoir mass (middle) and gas reservoir consumption timescale (bottom) of the exemplar simulated galaxy with a classical knee. We measure the quantities within spherical apertures of commoving radii $R_{\rm ap} = [3, 10, 30, 100]$ckpc, centred about the minimum of the potential of the galaxy's main progenitor. Analytic fits to the SFR and consumption timescale are shown with dashed lines.

Table 2.1: Table of best-fitting model parameters of sigmoid function to merger tree evolutionary tracks of t_g.

R_{ap} [ckpc]	L [Gyr]	t_0 [Gyr]	k	$t_{g,0}$ [Gyr]
3	1.39	0.37	-1.13	1.18
10	5.21	2.37	-0.99	1.18
30	38.3	0.64	-0.73	1.20
100	31.8	3.10	-0.91	1.38

2.4.1 A brief description of the one-zone GCE framework

There is an increasing number of chemical evolution frameworks being made publicly available such as the Flexible Chemical Evolution model (FlexCE; Andrews et al., 2017), ChemPy (Philcox & Rybizki, 2019) and the Versatile Integrator for Chemical Evolution (VICE; Johnson & Weinberg, 2020, Johnson et al., 2021a, Griffith et al., 2021). Starting from a set of assumed stellar evolution timescales, chemical yields, and an IMF, these one-zone GCE models[3] solve a set of differential equations to predict the evolution of element abundances within a galaxy's gas reservoir. They are typically used to infer galaxy formation histories from the distributions of stellar populations of the Milky Way and other Local Group galaxies in various chemical planes. As indicated by their name, 'one-zone' GCE models assume a uniform gas reservoir, all of which is star forming, and into which the nucleosynthetic products of stellar evolution are perfectly mixed upon their release.

Here we elect to use the VICE model. Therein, the SFR is specified by the product of the mass of the (proto-) galaxy's gas reservoir, and the star formation efficiency, where the latter is the inverse of the gas consumption timescale, t_g. The gas reservoir mass follows from the history of gas inflow, the star formation rate, and the gas outflow rate due to feedback (e.g., Nidever et al., 2020a). The reduction in gas mass due to outflows is generally specified by the product of the star formation rate and a mass loading factor, η, i.e. $\dot{M}_{out}(t) = \eta \dot{M}_\star(t)$, usually assumed to be a constant. GCEs also typically adopt fixed values of the gas consumption timescale, of $t_g \simeq 1$ Gyr (e.g. Weinberg et al., 2017a), though there are exceptions in the literature (e.g., Hasselquist et al., 2021b; Vasini et al., 2023). This timescale is typically motivated from the observationally-inferred consumption timescale of molecular gas in nearby galaxies ($\simeq 0.5 - 2$ Gyr, e.g.

[3]Multi-zone models that predict the radial dependence of element abundance distributions have been constructed, primarily to take advantage of the radially-resolved abundances available for the Milky Way. A comprehensive comparison of numerical simulations and multi-zone models is beyond the scope of this study.

Leroy et al., 2008, 2013; Sun et al., 2023), with observations of distant galaxies possibly indicating a shorter molecular gas consumption timescale (Tacconi et al., 2018).

2.4.2 The evolution of an exemplar simulated galaxy with a classical knee

The evolution of the gas reservoir's mass, $M_{\rm gas}(t)$, and parameters such as $t_{\rm g}$ and η, clearly have a marked influence on the resulting chemical evolution predicted by GCEs (e.g. Andrews et al., 2017; Johnson & Weinberg, 2020). Since in VICE the star formation rate is specified by the ratio of the gas mass and the gas consumption timescale, our choice of adopting a fixed star formation history means that the gas inflow history is specified by the gas consumption timescale, i.e. $M_{\rm gas}(t) = \dot{M}_\star(t)\ t_{\rm g}$, where $t_{\rm g}$ can be fixed or time evolving (by default VICE assumes a fixed gas consumption timescale of $t_{\rm g} = 1$ Gyr). We therefore begin by examining the evolving gas reservoir mass, and its corresponding consumption timescale, for our exemplar simulated galaxy. We focus here on $M_{\rm gas}$ and $t_{\rm g}$ and omit η, as the latter has a less significant impact on the predicted element abundances in VICE. We direct readers interested in the outflow mass loadings of EAGLE galaxies to the study of Mitchell et al. (2020), who showed that (at a fixed redshift and for a fixed aperture) mass loading increases with decreasing galaxy mass. We note therefore that examination of a time- or galaxy mass-dependent outflow mass loading in VICE would be an interesting avenue of inquiry, however this is beyond the scope of our investigation.

Fig. 2.9 shows the time evolution of the star formation rate, $\dot{M}_\star$ (top panel), the gas reservoir mass, $M_{\rm gas}$ (middle panel), and the consumption timescale of the reservoir, $t_{\rm g} = M_{\rm gas}/\dot{M}_\star$ (bottom panel). $M_{\rm gas}$ and $\dot{M}_\star$ are measured by summing the corresponding quantities from particles enclosed within spherical apertures of comoving radii $R_{\rm ap} = [3, 10, 30, 100]$ ckpc, centred about the minimum of the potential of the galaxy's main progenitor. We identify the latter using the simple merger tree scheme described by Pfeffer et al. (2018). The aperture measurements are shown using curves coloured yellow, red, blue and black, respectively. We measure the gas mass[4] and compute its associated consumption timescale within multiple apertures to obtain a sense of the uncertainty on these measurements when comparing with the predictions from the GCE. This is because it is not obvious how to most meaningfully compare the uniform gas

[4]We consider all gas, irrespective of its ionisation state, since the nucleosynthetic products of stellar evolution are not preferentially mixed with gas of any particular state.

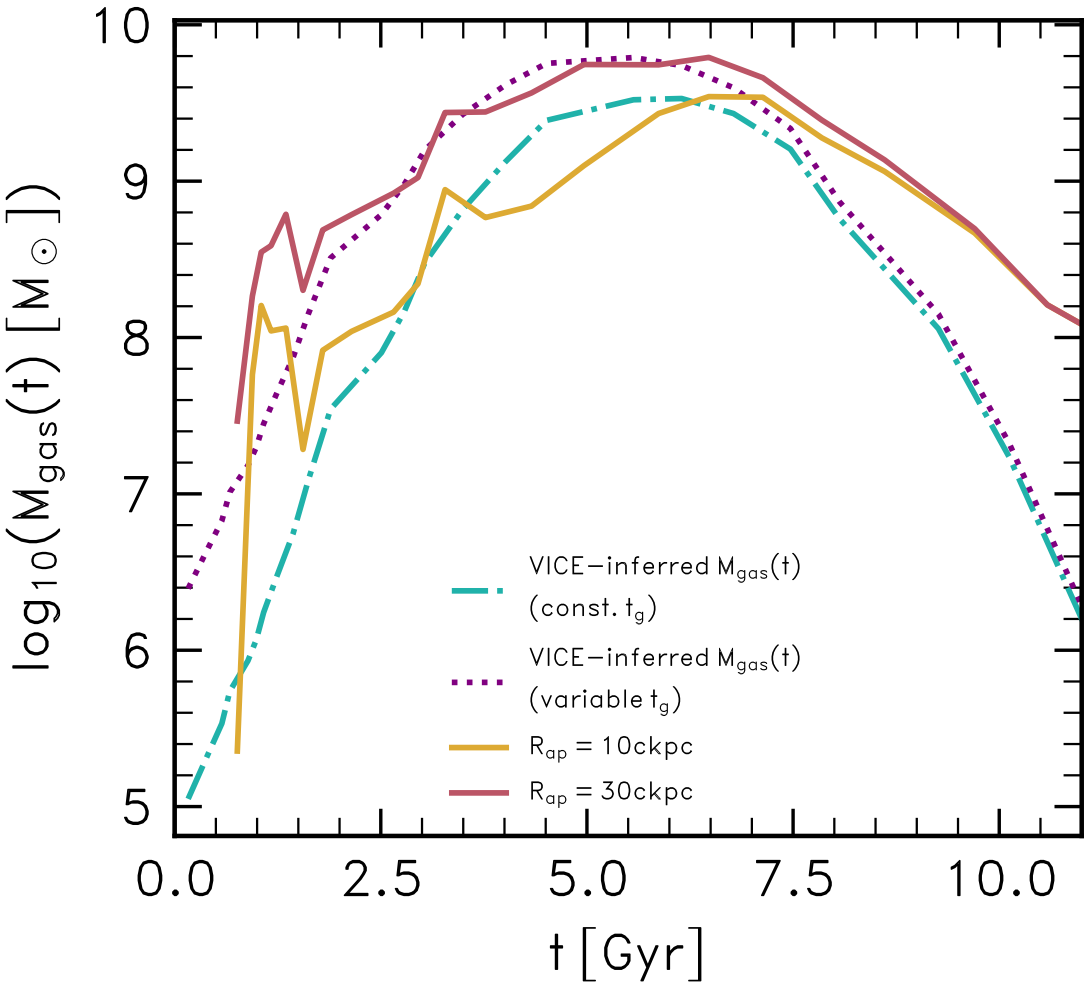

Figure 2.10: The evolution of the gas reservoir mass inferred by the VICE GCE, for the adopted star formation history, in the cases of a constant gas consumption timescale (t_g = 1 Gyr, cyan dot-dashed curve) and a variable t_g similar to that exhibited by gas within 30 ckpc of the main progenitor of the example simulated galaxy (dotted purple line). The true gas mass of the simulated galaxy, measured within spheres of radius 10 ckpc and 30 ckpc are shown with solid yellow and red curves, respectively.

reservoir of a one-zone GCE with the multi-phase gas distributions of hydrodynamically-simulated galaxies, within which only a fraction of the gas will be star forming. We stress that one should not consider only those particles that are star forming, because this would underestimate the mass of the reservoir into which newly-synthesised heavy elements are mixed.

The upper panel reveals that, consistent with the interpretation of Fig. 2.5, the exemplar simulated galaxy exhibits a peaked star formation history, which reaches a maximum $\dot{M}_\star \simeq 4\,\mathrm{M}_\odot\,\mathrm{yr}^{-1}$ at $t \simeq 6\,\mathrm{Gyr}$. The aperture measurements highlight that the star formation is centrally concentrated (i.e. entirely enclosed within $R_{\rm ap} = 30\,\mathrm{ckpc}$, with most enclosed within 10 ckpc). The middle panel shows the evolving mass of gas within

the apertures centred on the main progenitor, which broadly follow the same behaviour as the SFR, though for the $R_{\rm ap} = 100\,$ckpc aperture the peak gas mass of $2 \times 10^{10}\,\mathrm{M}_\odot$ is reached at $t \simeq 4\,$Gyr, giving a sense of the time taken for inflows onto the halo to reach the galaxy. In the bottom panel we show the consumption timescale of the gas reservoir, by taking the ratio of the gas mass and star formation rate measured within each of the apertures. It is immediately apparent that at early times ($t \lesssim 5\,$Gyr), the gas consumption timescale of the simulated galaxy is significantly longer than the default of 1 Gyr assumed by VICE. For the case in which we consider the gas within 10 ckpc, which can be considered conservative since this aperture only just envelops all of the star-forming gas (and thus plausibly excludes cold gas into which newly-synthesised heavy elements will be mixed), we recover a gas consumption timescale $t_{\rm g} > 10\,$Gyr for $t \lesssim 2\,$Gyr. For a fixed star formation history, a longer gas consumption timescale implies the presence of a larger (and less readily enriched) gas reservoir so, as we explore in more detail in §2.4.3, the implications for the evolution of element abundances predicted by GCEs are significant.

To simplify the use of the simulated galaxy's histories of star formation and gas consumption timescale as inputs to VICE, we approximate them with analytic functions. We use a Gaussian function for the star formation history,

$$\dot{M}_\star(t) = A_0 \exp\left(\frac{t - t_0}{\sigma}\right)^2, \tag{2.4}$$

and recover best-fit parameters to the SFR within $R_{\rm ap} = 30\,$ckpc of $A_0 = 3.47\,\mathrm{M}_\odot\,\mathrm{yr}^{-1}$, $t_0 = 6.54\,$Gyr and $\sigma = 1.92\,$Gyr. For the gas consumption timescale we fit a sigmoid function:

$$t_{\rm g}(t) = t_{\rm g,0} + \frac{L}{1 + \exp\left[-k(t - t_0)\right]}, \tag{2.5}$$

whose best-fit parameters for the four apertures are specified in Table 2.1. The best fits are shown with dashed lines in the top and bottom panels of 2.9.

2.4.3 A one-zone GCE model based on the SFH of a simulated galaxy with a classical knee

We construct a VICE model using the parameterised SFH of a realistic simulated galaxy with a classical knee (i.e. equation 2.4) as an input. We mostly adopt the default VICE parameters, an exponential SN Ia delay-time distribution, with a minimum delay time

$t_{\rm D,min} = 0.15$ Gyr and e-folding timescale $\tau_{\rm Ia} = 1.5$ Gyr. We also assume a Chabrier (2003) IMF with lower and upper mass limits 0.08 $M_\odot$ and 100 $M_\odot$ respectively.

Using the SN II ejected masses reported in Tables 7 and 10 of Portinari et al. (1998b), we compute the IMF-averaged yields from SN II for O and Fe by numerical integration using Equation 6 from Johnson & Weinberg (2020):

$$y_{\rm x}^{\rm cc} = \frac{\int_{\rm M_{SN}}^{\rm u} m_{\rm x} \frac{{\rm d}N}{{\rm d}m} {\rm d}m}{\int_{\rm l}^{\rm u} m \frac{{\rm d}N}{{\rm d}m} {\rm d}m}, \tag{2.6}$$

where m_x is the mass of element x ejected in the explosion of a star of initial mass m and $\frac{{\rm d}N}{{\rm d}M}$ is the assumed stellar IMF for which we adopt the Chabrier (2003) IMF with a lower stellar mass limit $l = 0.08$ $M_\odot$ and an upper stellar mass limit $u = 100$ $M_\odot$. $M_{\rm SN}$ is the minimum initial mass of a SN II progenitor, assumed to be 6 $M_\odot$ (Portinari et al., 1998b include electron capture SN, whose progenitors are assumed to be quasi-massive stars with initial masses $M_{\rm i,\ prog} \approx 6-7$ $M_\odot$). By taking the mean yield between metallicities $Z = 0.004$ and $Z = 0.05$, we derive net IMF-averaged yields for the Portinari et al. (1998b) yield tables of $y_{\rm II}^{\rm O} = 0.0172$ and $y_{\rm II}^{\rm Fe} = 0.00148$ for O and Fe, respectively. The EAGLE model rescales the SN II yield of Fe by a factor of 0.5, and we adopt the same SN II yield for Fe when running VICE. These yields place the pure SN II plateau at [O/Fe] = 0.67, in agreement with the low-metallicity trends seen in the simulations (see Fig. 2.1). The Fe yield from SN Ia is computed simply by taking:

$$y_{\rm Ia}^{\rm Fe} = \nu_{\rm Ia} \times m_{\rm Fe}, \tag{2.7}$$

where $\nu_{\rm Ia}$ is the total number of SN Ia per unit initial stellar mass, equal to $\nu = 2 \times 10^{-3}$ $M_\odot{}^{-1}$. Adopting the SN Ia yields of Thielemann et al. (2003) (an ejected Fe mass per SN Ia of $m_{\rm ej,Fe\ Ia} = 0.769$ $M_\odot$), we derive $y_{\rm Ia}^{\rm Fe} = 0.00154$.

The impact of adjusting the assumed gas consumption timescale for a fixed star formation history in the GCE is illustrated by Fig. 2.10: the mass of the one-zone gas reservoir inferred by VICE for the $t_{\rm g} = 1$ Gyr is denoted by the cyan dot-dashed curve, and that inferred from the fit to the gas consumption timescale of the gas within 30 ckpc of the simulated galaxy's main progenitor is shown with a purple dotted curve. At early epochs ($t \lesssim 2.5$ Gyr), the inferred gas reservoir is a factor of ~ 10 more massive in the latter case, with the offset diminishing at later times as the fit to the simulated galaxy's gas consumption timescale declines and, for $t \gtrsim 7$ Gyr, converges towards a value similar to the default assumption of $t_{\rm g} = 1$ Gyr. The solid yellow and red curves, repeated

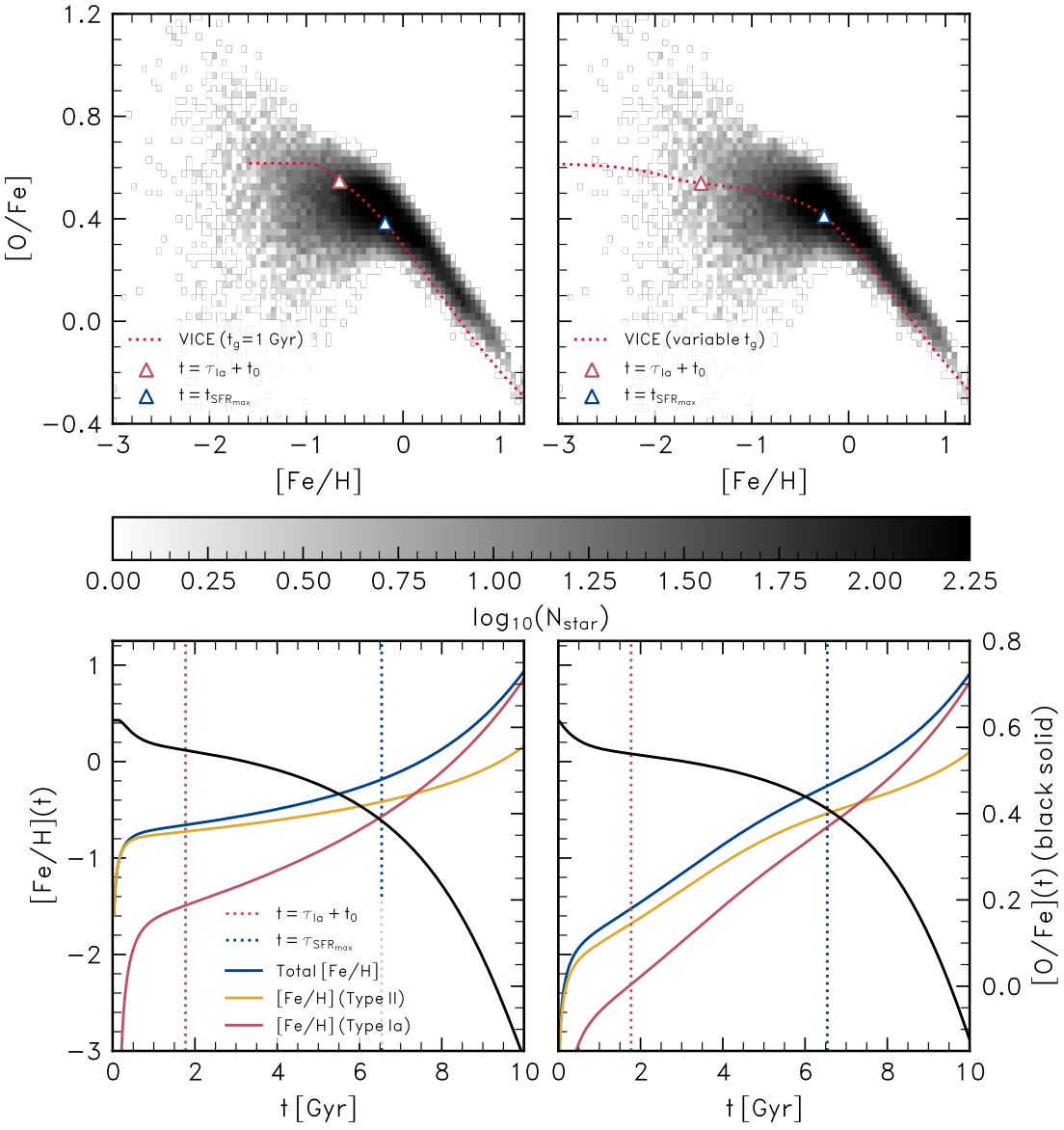

Figure 2.11: The element abundance evolution predicted by the VICE GCE when given, as an input, the SFH of an exemplar simulated galaxy with a classical knee. The left and right columns correspond to the constant t_g and variable t_g cases, respectively. The top panels show the temporal evolution of the gas reservoir's path through the α-Fe plane (red dotted curve). Red overlaid triangles denote the time at which one e-folding timescale of the assumed DTD (τ_{Ia} = 1.5 Gyr) has elapsed after the formation of the first stellar particle (t_0) and blue triangles denote the epoch at which the SFR peaks. The 2-dimensional histogram shows the stellar particle distribution from the exemplar simulated galaxy. The bottom panels shows the temporal evolution of [Fe/H] (left axis, solid blue curve), with yellow and red curves denoting the contributions from SN II and SN Ia, respectively, and [O/Fe] (right axis, solid black curve). Vertical dotted lines correspond to the same epochs denoted by the triangles in the top panels. The low-mass of the one-zone gas reservoir implied by the constant t_g case leads to its rapid enrichment to [Fe/H]> -1, so the plateau corresponds to only a brief period in the galaxy's evolution, comprises little mass and is more α-rich than that of the simulated galaxy. In contrast the (initially) more massive reservoir implied by variable t_g case is more gradually enriched, resulting in the later formation of the knee at a lower [O/Fe], similar to that of the simulated galaxy.

from the centre panel of Fig. 2.9, denote the total gas mass of the simulated galaxy's main progenitor within spheres of radius 10 ckpc and 30 ckpc, respectively. Note that the GCE gas reservoir mass based on the simulated galaxy's gas consumption timescale (dotted red curve) need not closely trace the simulated galaxy's actual gas mass within the same aperture (solid red curve): the GCE model reservoir is uniformly star-forming, whereas only some of the simulated galaxy's associated gas has density above the adopted density threshold for star formation. In addition, there is a mild dependence of the star formation rate on the gas pressure $\dot{m}_\star \propto P^{1/5}$ (Schaye & Dalla Vecchia, 2008), which is unaccounted for in this procedure and contributes to the mismatch.

Fig. 2.11 shows the resulting evolutionary tracks of [Fe/H](t) and [O/Fe](t) for our two models. The top panels show the α-Fe plane, while the bottom panel shows the evolutionary tracks as a function of cosmic time for these abundance ratios, split into the contributions of SN II and SN Ia, respectively. Red triangles on the evolutionary tracks indicate the abundances at $t = \tau_{\rm Ia} + t_0$, where $\tau_{\rm Ia}$ is the e-folding timescale of the assumed SN Ia DTD and t_0 is the formation time of the first stellar particle; blue triangles indicate the time at which the star formation rate peaks and the knee forms in the simulation ($\simeq$6.5 Gyr). The same times are indicated by vertical dotted lines in the bottom panels. The left columns correspond to the fixed $t_{\rm g} = 1$ Gyr case, the right to the variable case.

In both cases, the predicted metallicity of the knee closely corresponds with that exhibited by the simulated galaxy (see Fig. 2.2). However, the constant $t_{\rm g}$ case produces a plateau at [O/Fe]$\simeq$0.6 and a knee forms at $t \simeq \tau_{\rm Ia}$, preceding the time at which the knee forms in the simulated galaxy by $\simeq 5$ Gyr. The plateau therefore corresponds to only a brief and early period of the galaxy's evolution, during which there is little enrichment by SN Ia. In contrast, the (initially) more massive gas reservoir implied by the variable $t_{\rm g}$ case is more gradually enriched, leading to the formation of a gently declining high-α plateau over a prolonged period, so that the knee forms at a much later time, broadly corresponding to that at which the star formation rate begins to decline. It is noteworthy that the two cases, implementing identical yields for SN II and SN Ia and the same IMF, yield plateaus of significantly different α-richness. The constant $t_{\rm g}$ case features a short-lived plateau at the [O/Fe] value corresponding to the IMF-averaged yield of SN II, indicating that the natal gas of these stars was enriched exclusively by SN II. The same feature is seen in in the variable case for the very low metallicity ([Fe/H]$\lesssim -2.5$) part of the plateau. However, at greater metallicity (corresponding to $t \gtrsim \tau_{\rm Ia}$), [O/Fe] declines steadily, which is indicative of a growing contribution to enrichment by SN Ia.

The evolution of stellar abundances shown in the bottom panels of Fig. 2.11, analysed in the light of Fig. 2.10, highlights why, for a fixed star formation history, the assumed gas consumption timescale has such a marked influence on the evolution of the element abundances. The much less massive gas reservoir in the constant t_g case is quickly enriched, reaching [Fe/H]$= -1$ at $t \simeq \tau_{Ia}$, whereas the more massive reservoir implied by the variable t_g case is enriched gradually, attaining [Fe/H]$= -1$ at $t \simeq 5$ Gyr. This has significant implications for the resulting stellar metallicity distribution function (MDF), which we show in Fig. 2.12. Since the star formation rate adopted is relatively low at early times, the brief window of time before the gas reservoir is enriched in the $t_g = 1$ Gyr case leads to a paucity of metal poor stars (solid blue curve), compared to the MDF of the simulated galaxy (red histogram), which in turn is broadly reproduced by the variable t_g case (solid yellow curve).

Our experiments with VICE demonstrate that the nucleosynthetic products of the stellar populations of the progenitors of Milky Way-like galaxies are almost certainly mixed into a reservoir of gas that is significantly more massive and spatially-extended than the nascent galaxy's reservoir of molecular gas, with much of this larger reservoir either forming stars at a later time, or being expelled from the circumgalactic environment by feedback-driven outflows. Approximating this scenario with a one-zone GCE model therefore requires the adoption of a longer consumption timescale than that one infers from observations of molecular gas in distant galaxies (e.g. Tacconi et al., 2018), ensuring that newly-synthesised metals are sufficiently diluted.

2.4.4 The nature of the [α/Fe] plateau

Both of the VICE models exhibit a nearly flat [O/Fe] trend between [Fe/H] $= -1.5$ and -0.5, but the nature of this trend is quite different in the two cases. For the constant-t_g model, the plateau in this regime still reflects the Type II supernova yield ratio. For the variable-t_g model, the [O/Fe] in this regime is about 0.1-dex below this ratio, and it stays roughly flat because the rising SFR allows current Type II enrichment to keep pace with the growing Type Ia enrichment from the growing evolved population. The knee arises when the SFR begins to decline, but it would be present, albeit less sharply, even if the SFR merely flattened and became constant.

The variable-t_g model is reminiscent of the model of early Milky Way chemical evolution proposed by Conroy et al. (2022a) (see Chen et al., 2023a for a broader sample of similar models), which is motivated by the observed [α/Fe] $-$ [Fe/H] trends in the H3 survey

of the stellar halo. There the star formation efficiency grows rapidly from a low value of $t_g^{-1} = (50\ \mathrm{Gyr})^{-1}$ at $t < 2.5$ Gyr to $(2.36\ \mathrm{Gyr})^{-1}$ at $t > 3.7$ Gyr. The [α/Fe] track declines from +0.6 at low [Fe/H] to about +0.25 at [Fe/H] = −1.3, then rises gently in response to the accelerating SFR before turning downward again above [Fe/H] ≈ -0.5. The behaviour of our variable-t_g model is milder than this, with [O/Fe] always declining, but it is similar enough to suggest that the kind of evolution envisioned in the Conroy et al. (2022a) model arises fairly commonly in EAGLE galaxies. This behaviour also supports the contention of Maoz & Graur (2017) that the [α/Fe] plateau observed in the Galactic thick disk already includes substantial Type Ia supernova enrichment.

As Fig. 2.12 shows, the MDF is a good diagnostic for distinguishing these two classes of GCE models. The age-metallicity relation of metal-poor stars is also a valuable diagnostic for the early behaviour of t_g, especially if ages are accurate enough to resolve the evolution from [Fe/H] ≈ -1.5 to -0.5 in a stellar population that can reasonably be ascribed to a single well-mixed progenitor.

We have examined here the star formation history of a single exemplar galaxy, but we note that in one-zone GCE models where the star formation rate is set by the ratio of the gas reservoir mass and the gas consumption timescale, the assumption of a short gas consumption timescale will result in rapid enrichment of the gas reservoir for any star formation rate. As such, we argue that the assumption of a gas consumption timescale that is significantly shorter at early epochs than is indicated by realistic cosmological hydrodynamical simulations of galaxies, leads to the unrealistic prediction that the natal gas of stars comprising α-rich plateaus was enriched exclusively by SN II.

2.5 Summary of results and conclusions

We have examined the stellar [α/Fe]-[Fe/H] distribution of $\simeq 1000$ galaxies of present-day mass $M_\star \gtrsim 10^{8.5}$ M$_\odot$ that form in a high-resolution simulation from the EAGLE suite. The simulation has been shown elsewhere to reproduce a wide range of key properties of the observed galaxy population. Our main conclusions can be summarised as follows:

SUMMARY POINTS

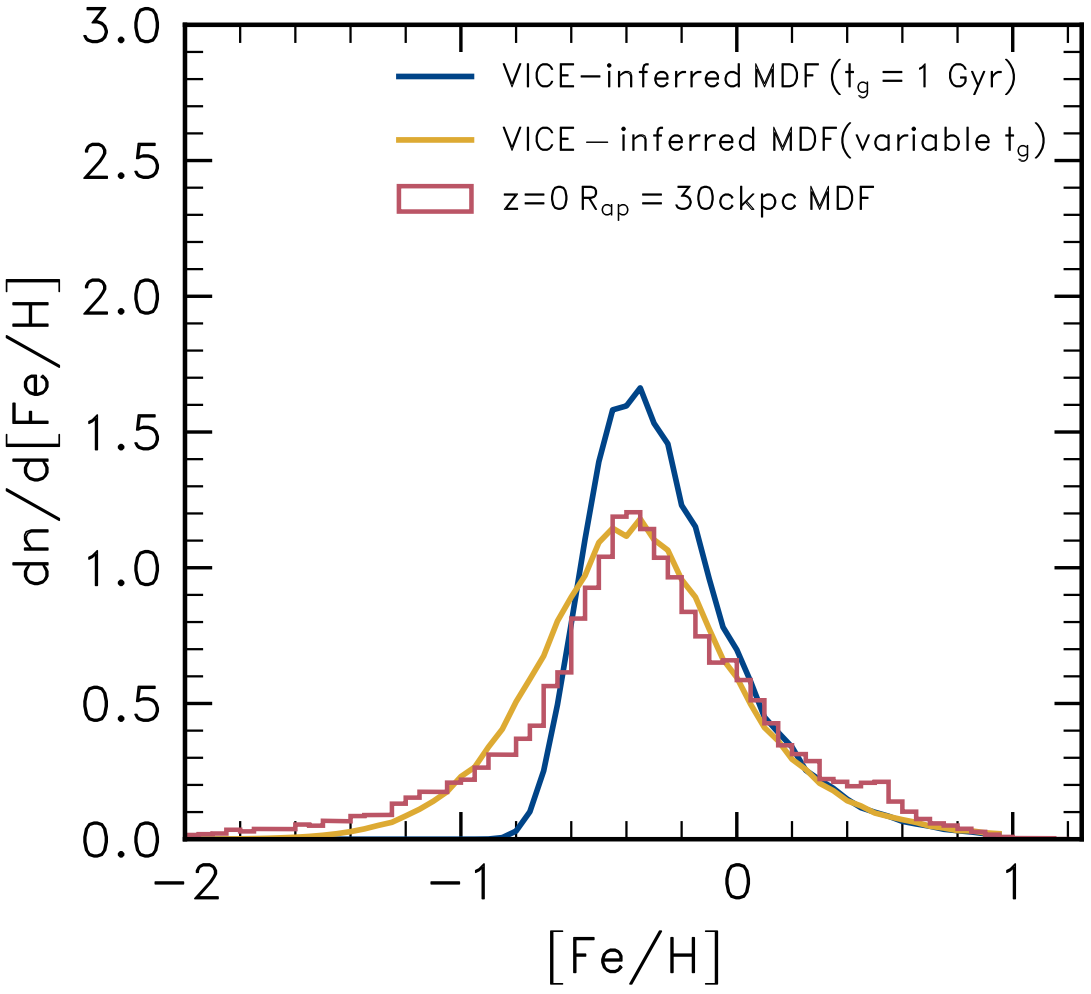

Figure 2.12: Metallicity distribution function (MDF), using [Fe/H] as a proxy for metallicity, of the exemplar simulated galaxy with a classical knee (red histogram), and of the VICE GCE model using the simulated galaxy's SFH as an input, for two cases of the adopted gas reservoir consumption timescale. The blue curve corresponds to the VICE default, t_g = 1 Gyr, the yellow curve corresponds to a variable gas consumption timescale similar to that exhibited by the simulated galaxy (see Eq. 2.5 VICE reproduced the simulated galaxy's MDF closely in the latter case but the assumption of a constant, short gas consumption time results in a paucity of low metallicity ([Fe/H]$\lesssim -1$) stars.

1. The simulated galaxies exhibit a diversity of morphologies in the α-Fe plane (Fig. 2.1). The distributions can be broadly categorised into three types: i) "classical knees" which exhibit a high-α plateau followed by a declining-α shin; ii) "single-slopes" which have mono-gradient α-Fe planes, and; iii) more complicated distributions such as "inverted knees", where there is a sequence of increasing α at high [Fe/H].

2. The galaxy population is dominated by classical knees, but there is a significant

mass dependence to the relative population of each type (Fig. 2.3). Single slopes are more common for $M_\star \lesssim 10^9\,\mathrm{M}_\odot$, but their frequency decreases monotonically with $M_\star$, while that of classical knees increases. We find that the slope of the plateau on the α-Fe plane is consistent with that of the single slopes but that of the shin is typically steeper by a factor $\simeq 2$ (Fig. 2.4). This indicates that the relative contributions to enrichment by SN II and SN Ia is similar in plateaus and single slope galaxies, whereas the shin is characterised by a diminished contribution from SN II.

3. Galaxies with classical knees exhibit peaked SFHs, typically reaching their maximum at $t \simeq 5-7\,\mathrm{Gyr}$ ($z \simeq 1.2-0.7$) before exhibiting a sustained decline until the present day. Contrary to the predictions of GCE models, we find that the typical time of α knee formation, t_{knee}, does not coincide with the time at which SN Ia first contribute significantly to the chemical enrichment (Fig. 2.5). Rather, t_{knee} corresponds roughly to the time at which the SFR begins to decline. The α-poor, Fe-rich shin forms when the star formation rate declines, so that SN II do not enrich the ISM as effectively as SN Ia. This results in the slope of the α-Fe shin being significantly steeper than that of the high-α plateau as enrichment switches from being dominated by young stellar populations to old stellar populations.

4. Conversely, the SFHs of galaxies showing single-slope distributions in the α-Fe plane are not as strongly peaked as those with classical knees. As a result, the stars of single slopes galaxies have a broader spread of stellar ages than those of classical knees.

5. Simulated galaxies presenting classical knees exhibit a correlation between the metallicity of the α knee and galaxy mass, albeit with significant scatter in $[\mathrm{Fe/H}]_{\mathrm{knee}}$ at fixed $M_\star$ (Fig. 2.7). The residuals about this scaling relation (which we dub the MKR) correlate strongly with the fraction of the mass in the high-α plateau.

6. The MKR exhibited by the simulated galaxies has slope $0.246 \pm 0.077\ \mathrm{dex}\,\log_{10}(\mathrm{M}_\odot)^{-1}$, consistent with the Local Group dwarf galaxy MKR which has slope $0.385 \pm 0.239\ \mathrm{dex}\,\log_{10}(\mathrm{M}_\odot)^{-1}$ (Fig. 2.8). The simulations also broadly reproduce the observed scatter in the MKR. Nidever et al. (2020a) reported a strong deviation of the Magellanic Clouds from that relation. However, although it may have a classical knee at very low metallicity, we find that the bulk

of their stellar populations do not follow the distribution of classical knees in the α-Fe plane, which may explain the discrepancy.

7. One-zone chemical evolution models, using as an input the SFH of an exemplar realistic simulated galaxy that exhibits a classical knee, do not reproduce the element abundance history of the simulated galaxy when adopting a constant, and relatively short, gas consumption timescale, typically assumed to be $t_{\rm g} \simeq 1$ Gyr in the literature (Fig. 2.11). The mass of the one-zone gas reservoir inferred by GCE at early epochs is much smaller than the gas mass associated with the main progenitor of the simulated galaxy, resulting in the reservoir being enriched to $[{\rm Fe/H}] = -1$ almost instantaneously. This yields a plateau in the α-Fe plane that is exclusively enriched by SN II, but whose formation is so rapid that it comprises little stellar mass, resulting in a metallicity distribution function that lacks a significant population of metal poor ($[{\rm Fe/H}] < -1$) stars. In contrast, by adopting a gas consumption timescale that evolves in a similar fashion to that of the simulated galaxy, the stars of the plateau form over several gigayears and are significantly enriched by both SN II and SN Ia.

Our findings motivate a revision of the canonical interpretation of the origin of the distinct sequences that are often, but not always, observed in the [α/Fe]-[Fe/H] distribution traced by the stellar populations of Local Group galaxies. At the root of our conclusions is a physical formulation of the star formation efficiency. The latter is a parameter of GCE models that is difficult to constrain, and which we have estimated here from the properties of the gaseous environment of the main progenitor of a realistic simulated galaxy. This application is a modest example of a growing trend in the field of Galactic Archaeology, whereby the development of increasingly sophisticated cosmological numerical simulations, on a par with the ever growing size and complexity of observational maps of the chemodynamical properties of Local Group galaxies, is deepening our understanding of the physical processes that dictate their formation and evolution.

Chapter 3

Chemical tagging with APOGEE, MUSE, and HST: constraints on the formation of ω Centauri

That is not dead which may eternal lie, and in strange aeons even death may die.

The Call of Cthulhu, H.P. Lovecraft

3.1 Introduction

In the prevailing ΛCDM cosmogony, the assembly of the Galaxy was thanks partly due to its accretion of many so-called 'building blocks' during earlier cosmic epochs. In this vein, advancements in the field of Galactic archaeology have led to a number of associations between the debris that comprise the Milky Way's (MW) stellar halo several Galactic globular clusters (GCs). Such associations find support in the theoretical expectation that building blocks accreted at early cosmic epochs are survived by at least some members of their GC systems at $z = 0$ (Searle & Zinn, 1978a; Kruijssen et al., 2019b). Many of these building blocks may also have hosted nuclear star clusters (NSCs), which are hypothesised to be built from a combination of *in-situ* star formation and the spiralling in of GCs from their host galaxy through dynamical friction (see Neumayer et al., 2020, and references therein). There is perhaps no better example of this phenomenon in action than NGC 6715 (M54) (Ibata et al., 1994a), the presumed NSC of the Sagittarius dSph, which is currently in the process of merging with the Milky Way.

ω Centauri (ω Cen) is the most massive ($M = 3.55 \times 10^6$ M$_\odot$; Baumgardt & Hilker, 2018) of the Milky Way's stellar clusters. It has been demonstrated to host multiple stellar populations (MPs; see Renzini et al., 2015; Bastian & Lardo, 2018, and references therein) which are obvious both photometrically (Milone et al., 2017a; Nitschai et al., 2024) and chemically (Johnson & Pilachowski, 2010; Marino et al., 2011; Alvarez Garay et al., 2024). This is in spite of the fact that ω Cen's stars exhibit a broad spread in metallicity (e.g., Pancino et al., 2000; Frinchaboy et al., 2002; Nitschai et al., 2023). Additionally, its metallicity distribution function (MDF) shows multiple distinct peaks in [M/H] (e.g., Villanova et al., 2014; Johnson & Pilachowski, 2010; Alvarez Garay et al., 2024), indicating that it formed its MPs over an extended star formation history (SFH) that was likely characterised by multiple episodes. This is atypical of 'normal' Galactic GCs, which are typically characterised by a mono-metallic stellar population.

ω Cen also has a strongly retrograde, coplanar orbit relative to the Milky Way disk (e.g. Majewski et al., 2000), which has naturally led to conjecture as to its origin in the context of the hierarchical assembly of the Milky Way, and not just the physics responsible for the formation of its MPs. Earlier work speculated that ω Cen may be the nucleated remnant of a galaxy which originally resembled the massive dSphs we see in the Local Group today. According to this scenario, such a galaxy would have then been captured by the Milky Way (e.g. Bekki & Freeman, 2003) and gradually stripped over many

passages, in a process similar to that currently undergone by the Sagittarius dSph. Such antecedents might explain its retrograde orbit and structural parameters, which place it on the border between the loci occupied by GCs and the ultra-compact dwarfs in the luminosity-size relation, (e.g., Tolstoy et al., 2009, and references therein).

While an enormous amount of work has gone into obtaining data from ω Cen and constraining its properties, it was not until the advent of *Gaia* (Gaia Collaboration et al., 2016) that these data could be placed in context with a representative sample of stars within the Galaxy. The addition of detailed chemical compositions and radial velocities of individual stars from massive spectroscopic surveys (e.g. GALAH, LAMOST, and APOGEE De Silva et al., 2015; Deng et al., 2012; Majewski et al., 2017b) with astrometric information from *Gaia* has enabled the construction of a rich multi-dimensional chemo-kinematic dataset.

The above data prompted speculation as to the association of ω Cen with recently identified halo substructures. Massari et al. (2019) proposed that ω Cen was the nuclear star cluster of the Sausage/Gaia Enceladus' progenitor galaxy (S/GE; Belokurov et al., 2018b; Haywood et al., 2018; Helmi et al., 2018; Mackereth et al., 2019b), which underwent a major merger with the Milky Way some $\simeq$ 10 Gyr ago. Alternatively, Myeong et al., 2019 advocate that ω Cen is instead associated with the 'Sequoia' remnant, also associated with the bulge GC FSR 1758 (Barbá et al., 2019). It is thought that there is a specific mass range in the scaling relation between $M_{\rm host}$ and $M_{\rm NSC}$ within which NSCs formed by an almost 50/50 mixture of *in-situ* star formation and the inspiralling of a number of its host's globular clusters (Neumayer et al., 2020; Fahrion et al., 2021). If ω Cen does originate from the Sausage/Gaia-Enceladus, notional estimates (e.g. Limberg et al., 2022) for the mass of this system and the measured mass of ω Centauri place it firmly within this mass range.

In this chapter, we give an extensive overview of the properties of ω Cen using a combination of stellar abundances, astrometry, and HST photometry. In §3.2, we describe the data used for our study, and our procedure for selecting individual stellar populations within the sample, as well as the procedure we used to construct the so-called 'chromosome map' of ω Cen. In §3.3, we show the detailed chemistry of the multiple populations in ω Cen and provide a quantitative description of their properties, and speculate as to the origin of their abundance patterns. By identifying stars in common between our photometric and chemical data, we tie our analysis into the wider observational state of play by directly linking the loci stars occupy on the chromosome map to their detailed stellar abundance patterns. In §3.4 we fit galaxy chemical evolution

models to two of the three populations we identify in ω Cen. Finally, in §3.5, we thorough discuss our results in the wider context of proposed formation scenarios for ω Cen, and give a critical look at our modelling. We then provide a highly speculative formation scenarion for the cluster, and perform a detailed statistical comparison between what we identified as the 'field' population of ω Cen's progenitor and purported substructure in the Galaxy's stellar halo.

3.2 Data and Methods

Our analysis is based on an amalgamation of data from three different sources. Detailed chemical compositions for 1,756 ω Cen stars are extracted from the Schiavon et al. (2024) Value Added Catalogue (henceforth, simply VAC) of Galactic GC stars from the 17$^{\text{th}}$ data release (DR17) by the Apache Point Observatory Galactic Evolution Experiment (APOGEE Majewski et al., 2017b; Abdurro'uf et al., 2022). This catalogue is supplemented by *Gaia* astrometry (Gaia Collaboration et al., 2021), providing coordinates and proper motions alongside radial velocities from APOGEE.

Additional spectroscopic and multi-band photometric data come from the oMEGACat catalogue (Nitschai et al., 2023; Häberle et al., 2024), which combines spectroscopy from the ESO/VLT Multi Use Spectroscopic Explorer (MUSE, Bacon et al., 2010, 2014) with PSF photometry from the Hubble Space Telescope. The latter data are based on Advanced Camera for Surveys Wide Field Channel (ACS/WFC) and Wide Field Camera 3 UVIS Channel (WFC3/UVIS) covering the half-light radius of ω Cen ($R \approx 5'$).

In this section, we describe the data, our crossmatch between the VAC and oMEGACat, the quality cuts we perform on both samples, our construction of the so-called "chromosome map" (ChM) to reproduce that by Nitschai et al. (2024), and finally our method to split the VAC sample into different stellar populations on the basis of their chemical abundances.

3.2.1 The APOGEE value-added catalogue of Galactic globular cluster stars

The work presented in this chapter combines the latest data release (DR17; Majewski et al., 2017b; Abdurro'uf et al., 2022) of the SDSS-III/IV (Eisenstein et al., 2011; Blanton et al., 2017) and APOGEE survey (Majewski et al., 2017b; Abdurro'uf et al., 2022) with distances and astrometry derived from the third data release of the *Gaia* survey (Gaia Collaboration et al., 2021). The APOGEE DR17 catalogue of stellar parameters comprises high precision chemical abundances for over 20 species as well as radial velocities for approximately $\sim 700,000$ stars in total, within the Milky Way and a number of its satellites and GCs.

Elemental abundances and radial velocities were obtained from the analysis of high-resolution near-infrared spectra of hundreds of thousands of stars in both hemispheres, observed with the Apache Point Observatory 2.5m Sloan telescope (Gunn et al., 2006) and the Las Campanas Observatory 2.5m Du Pont telescope Bowen & Vaughan (1973). These spectra were obtained using twin high efficiency multi-fiber NIR spectrographs assembled at the University of Virginia, USA (Wilson et al., 2019). A technical summary of the overall SDSS-IV experiment can be found in Blanton et al. (2017).

Further in-depth information on the APOGEE survey, data, and data reduction pipeline can be found in Majewski et al. (2017b), Jönsson et al. (2020) & Holtzman et al. (2018), and Nidever et al. (2015), respectively. The APOGEE Stellar Parameters and Abundances Pipeline (ASPCAP) is described in García Pérez et al. (2016).

Chemical composition data based on earlier APOGEE data releases were presented for a number of Galactic GCs (Mészáros et al., 2015; Schiavon et al., 2017b; Masseron et al., 2019; Mészáros et al., 2020, 2021b). However, on a GC-by-GC basis the number of visits by APOGEE, apparent magnitudes and apparent sizes vary. Furthermore, prior APOGEE data releases lacked robust estimates of star-by-star GC membership probabilities. To address this issue, Schiavon et al. (2024) produced the SDSS/APOGEE Value Added Catalogue of Galactic Globular Cluster (GC) Stars (VAC). This VAC is the result of a sweeping search of the APOGEE DR17 catalogue for likely GC members using a set of membership criteria, leveraging precise astrometry (positions and proper motions) from *Gaia*, and radial velocities and chemical compositions from APOGEE.

We concern ourselves primarily with a subset of the APOGEE VAC, namely giants located in ω Cen. The sample of ω Cen stars analysed within this study is defined by the following set of criteria:

1. `GC_NAME=NGC5139`
2. $p_{\omega\mathrm{Cen}} > 0.5$
3. $\log g < 3.6$
4. 3500 K < T_{eff} < 4500K
5. S/N > 70 pixel^{-1},

where $p_{\omega\mathrm{Cen}}$ is the ω Cen membership probability and the other parameters have their usual meaning. These criteria yielded 1,555 unique stars in total. When data for other GCs are described in the analysis, they are subject to identical criteria on a GC-by-GC basis.

3.2.2 Complementary HST and MUSE data for ω Cen stars

Complementary HST photometry for APOGEE stars is derived from the oMEGACat catalogue (Nitschai et al., 2023; Häberle et al., 2024), comprising both MUSE and HST observations of individual stars within ω Cen, out to the half-light radius ($R \simeq 5'$). We applied the same quality cuts (QC) as in Nitschai et al. (2024), whereby we select red giants comprising the MUSE QC sample that are also present in the HST QC sample from Häberle et al. (2024). Thus, we are left with 10,850 stars satisfying the following conditions:

1. Present in the HST QC with $m_{F625W} < 17$ mag
2. Measurements in F625W, F435W, F275W, F336W, and F814W

Any star in ω Cen also observed as part of the *Gaia* mission has its source ID present in the oMEGACat catalogue, making the match to the VAC sample trivial. There are 135 stars present in oMEGACat satisfying the above conditions, which also appear in the VAC.

3.2.2.1 Constructing the ω Cen chromosome map

To briefly summarize, so-called "chromosome maps" have become a valuable diagnostic tool for identifying stellar populations with abundance anomalies in Galactic GCs. Based on photometry alone, they are very useful for the characterization of multiple populations in GCs for which spectroscopic abundances of large samples of member stars are not available. In addition, they are sensitive to helium abundance variations, which are not easy to constrain from spectroscopy of cool stars. Their construction requires multi-band photometry combining optical and ultraviolet filters.

The method to produce a ChM for a mono-metallic globular cluster requires the construction of 'fiducial lines' (typically 'blue' and 'red') which trace the run of the 4^{th} and 96^{th} percentile values of colour as a function magnitude. Subsequently, the CMDs can then be 'verticalised' by computing Δ, which measures the position of a star with a given colour and magnitude relative to these fiducial lines. Judicious choice of filter combinations sensitive to physical properties, such as metallicity and light-element abundance variations, reveals different populations that may not be obvious from the CMD alone.

The colours of choice are $m_{F275W} - m_{F814W}$ and $C_{F275W,\,F336W,\,F435W}$, where the latter is defined as:

$$C_{F275W,\,F336W,\,F435W} = (m_{F275W} - m_{F336W}) - (m_{F336W} - m_{F435W}), \tag{3.1}$$

whereas the magnitude adopted for both CMDs is F814W.

We follow the procedure from Nitschai et al. (2024), briefly described here, but refer readers to Appendix C of that paper for detailed instructions. We start by selecting a sample of red giant stars meeting the quality cuts described in §3.2.2. Our procedure is mostly identical to Milone et al. (2017b), except that we use different photometric filters (Milone et al., 2017b, used F438W instead of F435W). As stated in that paper, the metallicity spread in ω Cen requires constructing several fiducial lines for sequences on the CMD with different [M/H]. We thus break the sample down by metallicity sub-group, by applying a 1D Gaussian Mixture Model (GMM) to the [M/H] distribution. We found 11 to be the number of components with the lowest Bayesian Information Criterion (BIC, after running up to 30), in agreement with Nitschai et al. (2024), We select labels from the GMM procedure corresponding to the metal-poor, metal-intermediate, and metal-rich stars.

We then constructed the fiducial lines for each metallicity group in both CMDs. We start by describing the method applied to the CMD based on the $C_{F275W,\,F814W}$ colour. For the metal-poor population, we used LOWESS smoothing (Cleveland, 1979b) in order to compute the difference at fixed magnitude for individual stars between their pseudocolor values and the LOWESS curve, δm. Then, the fiducials corresponding to the position of the 4th and 96th percentiles of the distribution of δm were simply constructed by adding $\pm$ 2 σ to the LOWESS-determined median. For the intermediate and metal-rich populations, the red giant branches are well separated, so that single LOWESS fiducial lines are calculated for $C_{F275W,\,F814W}$, and δm is derived from these for each star.

The procedure differed slightly in $C_{F275W,\,F336W,\,F435W}$. That is because the giant branches of the metal-poor and intermediate population are well separated in $m_{F275W} - m_{F814W}$, but not in $C_{F275W,\,F336W,\,F435W}$. Therefore, $\Delta_{F275W,\,F336W,\,F435W}$ values are calculated on the basis of fiducial lines, corresponding to the 4th and 96th percentiles for *i)* a combination of the metal-poor and intermediate stars, and *ii)* the metal-rich stars. Using these fiducial lines for both CMDs, we derived star-by-star values of $\Delta_{F275W,\,F336W,\,F435W}$ and $\Delta_{F275W,\,F814W}$, calculated for each colour using Eqs. C1-C11 and conditions from Table 3 in Nitschai et al. (2024).

3.2.3 Chemically tagging the multiple populations of ω Centauri

In order to identify the multiple populations (MPs) of ω Cen on the basis of their chemistry, we use k-means clustering applied to a parameter space consisting of the following stellar abundances of stars in the sample: [Fe/H], [Mg/Fe], [Si/Fe], [Al/Fe], and [Mn/Fe].

Over the course of chemical evolution expected during secular galaxy evolution, Mg, Si, and Al are thought to be contributed to the star-forming gas by SN II explosions (Woosley & Weaver, 1995; Portinari et al., 1998a; Chieffi & Limongi, 2004; Kobayashi et al., 2006a; Nomoto et al., 2013), with Al having yields that strongly depend on metallicity (Weinberg et al., 2019). All three elements are also affected by the MP phenomenon, where anomalous populations tend to exhibit Al-enhancement, Mg-depletion, and sometimes Si-enhancement (Alvarez Garay et al., 2024). Mn is an Fe-peak element, produced by both SN II and SN Ia (Weinberg et al., 2019), widely used in combination with Mg and Al to discriminate accreted from *in-situ* populations from one another (Das et al., 2020).

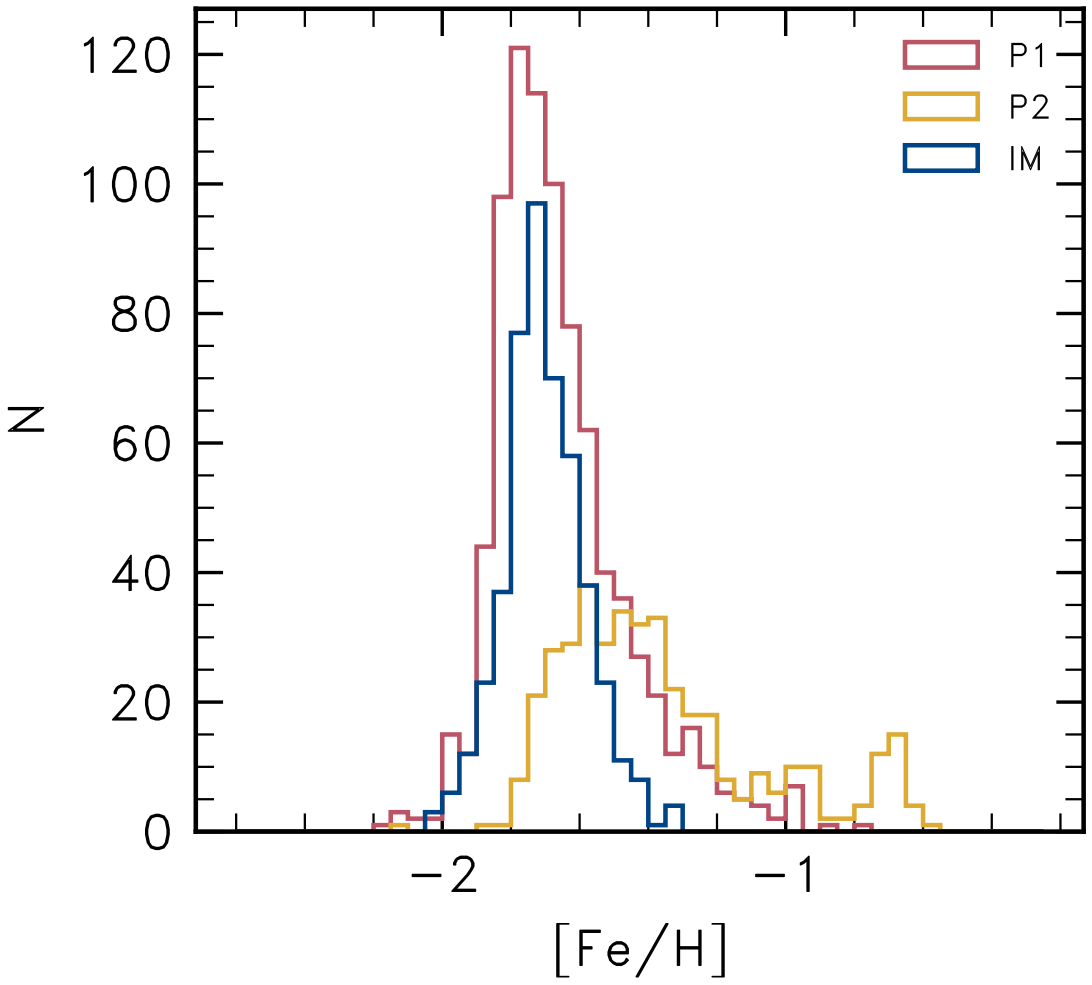

Figure 3.1: Metallicity distribution functions of the three populations identified by k-means clustering in ω Cen, which we label P1 (red), P2 (yellow) and IM (for intermediate; blue). P1 is characterised by its lower [Fe/H] and a tail towards higher [Fe/H], whereas P2 is more metal-rich and has a broader metallicity spread. Conversely, the intermediate population is characterised by a narrow dispersion in [Fe/H] at the same [Fe/H] as P1 (see Table 3.1).

Using a combination of these abundance ratios, we rescale the numerical values by subtracting the mean from each stellar abundance and then dividing the resultant number by the variance about the mean. On the basis of this rescaled dataset, we find that the data are well-described by $n = 3$ clusters, whose MDFs are shown in Fig. 3.1.

We label the three populations P1, P2, and IM. The reasons for this nomenclature are clarified in §3.3. The P1 and IM populations have similar metallicity distributions, though P1 exhibits a tail towards higher [Fe/H]. P2 is characterised by a broader metallicity spread that extends to [Fe/H]$\simeq -0.6$. In §3.3 we place these populations on canonical chemical planes and characterise their abundance patterns.

3.3 Interpreting the Abundance Patterns of ω Centauri's Multiple Stelar Populations

In this section, we first provide a quantitative analysis of the abundance patterns of our three clusters identified by the procedure described in §3.2.3, and speculate on the origin of these abundance patterns and how they shed light on ω Cen's assembly history.

Fig. 3.2 shows the distributions of the three ω Cen populations described in Section 3.2.3 in various chemical planes. Table 3.1, lists *i)* the median [X/Fe], *ii)* the dispersion in [X/Fe] ($\sigma_{[X/Fe]}$), and *iii)* the Spearman rank correlation coefficient (R_S) computed for each abundance ratio [X/Fe] with respect to [Fe/H]. We also provide measurements of the median [Fe/H], and the dispersion in [Fe/H] represented by the standard deviation ($\sigma_{[Fe/H]}$).

Fig. 3.2 displays some striking features. *Firstly*, there is a clear separation between P1 and P2 in these chemical planes. *Secondly*, strong correlations between [X/Fe] and [Fe/H] for several elements attest to the occurrence of strong chemical evolution induced by a history of active star formation. *Thirdly*, the fact that the P1 and P2 populations are extended over *parallel* sequences in many of the planes indicates that these two populations likely evolved in chemical detachment, suggesting that P1 and P2 stars formed in different locations, at different times, or both (see discussion by Mackereth et al., 2018b, for similar considerations in the context of the α-bimodality in galaxy disks). *Lastly*, the distribution of the IM population in all chemical planes is not characterised by a correlation between any abundance ratios and [Fe/H]. Instead, this population has a very small metallicity spread, combined with a large spread in the abundances of some elements, such as Al, C, and N. In fact, we show in Section 3.4 that these abundance variations display the anti-correlations known to exist in Galactic GCs (Ventura et al., 2013; Alvarez Garay et al., 2024).

3.3.1 The abundance pattern of the P1 population

The stellar abundances of the P1 population at the low metallicity end exhibit a pattern that resembles that of field stars at the same metallicity (e.g., [Mg/Fe]$\simeq$ 0.4 at [Fe/H] $\simeq -$ 1.8), which is consistent with the value of the high-α plateau (e.g., Mackereth et al., 2017; Horta et al., 2021b, 2023b). Above [Fe/H] ≈ -1.62 there is a monotonically increasing trend of [α/Fe] with [Fe/H] which is seen in both Mg and Si and reflected

	P1			IM			P2		
X	[X/Fe]	$\sigma_{[X/Fe]}$	R_S	[X/Fe]	$\sigma_{[X/Fe]}$	R_S	[X/Fe]	$\sigma_{[X/Fe]}$	R_S
C	0.07	0.36	0.54	-0.10	0.32	0.14	-0.08	0.21	0.12
N	0.36	0.37	0.17	0.82	0.31	0.52	1.26	0.25	0.77
Mg	0.36	0.11	0.58	0.26	0.08	0.09	0.00	0.24	0.84
Al	-0.11	0.17	0.69	0.48	0.24	0.30	1.05	0.19	-0.06
Si	0.29	0.09	0.55	0.26	0.04	-0.13	0.36	0.07	-0.47
Mn	-0.35	0.27	-0.37	-0.31	0.26	-0.51	-0.38	0.22	-0.18
Median [Fe/H]		-1.70			-1.69			-1.41	
$\sigma_{[Fe/H]}$		0.19			0.12			0.30	

Table 3.1: Summary of abundance ratios and their properties for three samples.

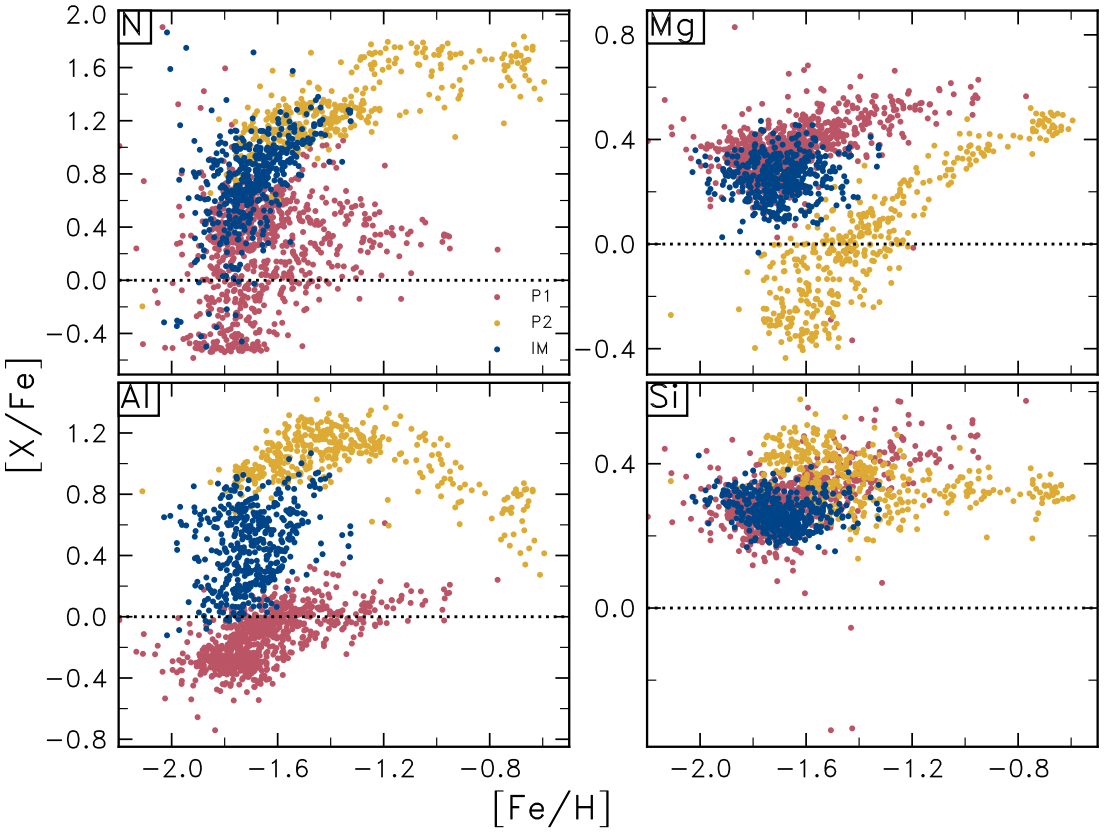

Figure 3.2: Distribution of k-means selected clusters on chemical planes, where the y-axis values are the element abundance ratios [X/Fe] for species X in Table 3.1 plotted as a function of [Fe/H]. Consistent with prior observations, the most obvious feature of these abundance planes is the discreteness of what we dub the P1 and P2 populations. The former is characterised by initially halo-like light-element abundances that increase over the whole range of [Fe/H], consistent with a starburst. P2 is characterised initially by heavy depletion in Mg, heavy enhancement in Al and enhancement in Si. As chemical enrichment took place in the cluster, the abundances tend back toward those characteristic of enrichment by SN II and SN Ia. The IM population has a narrow metallicity spread compared to P1 and P2, slight depletion in Mg (but not Si), and intermediate C, N, and Al-enhancement between P1 and P2.

by the high Spearman rank correlation coefficients (R_S, 0.55 and 0.58, respectively) for both of those abundances as a function of [Fe/H]. Such a strong positive correlation between [α/Fe] and [Fe/H] implies that P1 underwent an early starburst which resulted in the chemical enrichment by CCSNe dwarfing that by SNe Ia (Gilmore & Wyse, 1991b; Weinberg et al., 2017b; Mason et al., 2023). The P1 stars also exhibit similar behaviour in [Al/Fe]. At low [Fe/H] ([Fe/H]$\simeq -2.0$), P1 shows [Al/Fe] $\simeq -0.3$, which is consistent with what is seen in the halo field (e.g., Horta et al., 2023b). In addition, [Al/Fe] is strongly correlated with [Fe/H] (R_S=0.69). As in the case of α elements, a significant fraction of Al is produced in CCSNe, so that this trend is further evidence that P1 underwent an early starburst. Conroy et al. (2022b) claim that similar behaviour,

at approximately the same metallicity, can be seen in prograde ($L_z > -500$ kms^{-1}) stars in the stellar halo.

If indeed the early starburst hypothesis is correct, the star forming gas reservoir had abundances typical of field stars in the halo at same [Fe/H]. This starburst must have been short-lived enough that either the gas was consumed entirely or star formation was quenched before SNe Ia could make an important contribution to the chemical enrichment of the gas.

3.3.2 The abundance pattern of the P2 population

Unlike their P1 counterparts the stars belonging to the P2 population exhibit, at the low metallicity end ([Fe/H]≃–1.7) depleted Mg ([Mg/Fe]≃–0.2), enhanced Si ([Si/Fe]≃0.40), and very strongly enhanced Al ([Al/Fe]≃0.8). Similarly to the case of P1, [Mg/Fe] increases monotonically with [Fe/H]. Conversely, [Si/Fe] initially decreases and flattens to a plateau of [Si/Fe]≃ 0.3. [Al/Fe] also increases steeply with [Fe/H], before reaching a peak at [Fe/H]≃ −1.4 and declining towards higher [Fe/H]. These abundance patterns are consistent with observations ω Cen stars from other groups (e.g., Johnson & Pilachowski, 2010; Alvarez Garay et al., 2024).

Such abundance patterns are ubiquitous among the Galactic globular clusters that host MPs. Si and Al enhancement, coupled with Mg depletion, have been postulated to be a clear sign that the star-forming gas reservoir incorporated material processed in stellar interiors by the Mg-Al cycle, during high-temperature ($T \simeq 10^7$K) H-burning in massive as well as AGB stars (e.g., Arnould et al., 1999). As in the case of P1, the steep growth of [Mg/Fe] and [Al/Fe] with [Fe/H] on the low metallicity end suggests the occurrence of an early burst of star formation. However, [Si/Fe] does not go up with metallicity, making the interpretation of the data for P2 difficult. This issue is further discussed in Section 3.4.

3.3.3 The abundance pattern of the IM population

We discussed the abundance patterns of the P1 and P2 populations in detail in previous sections, concluding that they both differ in substantial ways. The IM population is also characterised by substantially different chemistry. One chief difference is the fact that IM stars present a very small dispersion in metallicity, indeed significantly smaller than those

of P1 and P2 populations. The dispersion in the metallicity of the IM population is lower than that of the metal-poor peak of P1 ($\sigma_{[Fe/H],\,IM} = 0.12$, versus $\sigma_{[Fe/H],\,P1} = 0.19$). In addition, it presents a different distribution in the relevant chemical planes. The light-element abundance ratios of IM stars lie somewhere between those of P1 and P2 populations at same [Fe/H]. For α elements Mg and Si, IM is closer to P1, whereas for N and Al it shows much larger variance than P1 and P2 stars at the same metallicity.

Looking more closely, the distribution of the IM population in chemical space is somewhat puzzling, especially when considering the Al-Fe and N-Fe planes. In both planes the trends described by the IM and P2 populations merge seemlessly, with the latter looking like an extension towards higher metallicity of the trends exhibited by the IM population, suggesting a possible chemical evolution link between the two. However, the much closer similarity between IM and P1 in the abundances of Si and Mg seem to rule out such a chemical association, arguing instead in favour of a chemical evolution link between those two latter populations. These contradictory features make it quite difficult for one to devise a clear qualitative evolutionary path connecting these three populations.

3.3.4 On the absence of a chemical evolution history connecting the P1, P2, and IM populations

The abundance patterns of the three populations displayed in Fig. 3.2 are intriguing. The fact that P1 and P2 draw widely separate trends in almost all chemical planes suggests no straightforward evolutionary link between these two populations. By the same token, in some chemical planes the IM population seems to be chemically associated with the P1 stars (Mg-Fe and Si-Fe), whereas in others (Al-Fe and N-Fe) there is a hint of a chemical evolution connection between IM and P2 populations.

Additional insights can be gained by adopting Mg, instead of Fe, as the reference metallicity indicator (following Weinberg et al., 2019, and subsequent work). Unlike Fe, Mg has a single source of enrichment (SNe II), so that the interpretation of Mg abundances is not affected by ambiguities stemming from the enrichment by the ejecta of both SNe II and SNe Ia in the case of field stars in galaxies. However, given that one of the characteristic abundance patterns of 'extreme stars' such as our P2 sample is Si-enrichment and Mg-depletion, thought to arise the stars formed from material processed by high-temperature quiescent hydrogen burning (see Alvarez Garay et al., 2024, and

references therein), it is possible that ambiguities of a different nature may manifest in the P2 stars by adopting Mg as a metallicity tracer.

The result is shown in Fig. 3.3. It becomes immediately obvious that the three populations are quite detached in critical chemical planes, particularly Al-Mg. Stars belonging to the IM population show median [Mg/H]≃–1.43, whereas the P1 and P2 populations start their chemical evolution at [Mg/H]≃–1.6 and –2.0, respectively. Moreover, P2 stars do not seem to constitute an extension of the IM trend in either the [Al/Mg]-[Mg/H] or the [N/Mg]-[Mg/H] planes. P2 stars also differ substantially from the P1 and IM in [Si/Mg] on the metal-poor end. In these planes, however, IM and P1 populations are similar, though slightly different in [Fe/Mg] and [Si/Mg], while differing quite substantially in [Al/Mg].

This exercise demonstrates that the seeming chemical evolution connection between the P2 and IM populations, apparent in the Al-Fe and N-Fe planes falls apart when Mg is taken as the reference metallicity indicator. By the same token, while the IM population is more similar to the metal-poor end of the P1 population, differences are large enough that it is not quite easy to conceive how one can evolve from the other. We next consider how further examination of the abundance pattern of the IM population can help resolving this conundrum.

3.3.5 The resemblance of the IM population to mono-metallic Galactic globular clusters

Fig. 3.4 shows the distribution of our populations on the Mg-Al plane. The arrows indicate the direction of [Fe/H] growth in the cases of P1 and P2 (as discussed in Section 3.3.3, the IM population has very small dispersion in [Fe/H]). Most notably, the IM population shows a significant anticorrelation, at approximately fixed [Fe/H], between [Al/Fe] and [Mg/Fe]. This is consistent with the behaviour of so-called second-generation populations within monometallic Galactic globular clusters (e.g., Carretta et al., 2012a,b; Mészáros et al., 2015; Schiavon et al., 2017b; Nataf et al., 2019; Mészáros et al., 2020). On this basis, we speculate that the IM population may in fact be the result of the spiralling in of a field globular cluster belonging to the host galaxy of ω Cen when it was the NSC of that galaxy.

To test this hypothesis, we search the Schiavon et al. (2024) VAC for globular clusters whose median [Fe/H] lies within [Fe/H] $\pm$ $\sigma_{\rm [Fe/H]}$ of the median value for IM stars

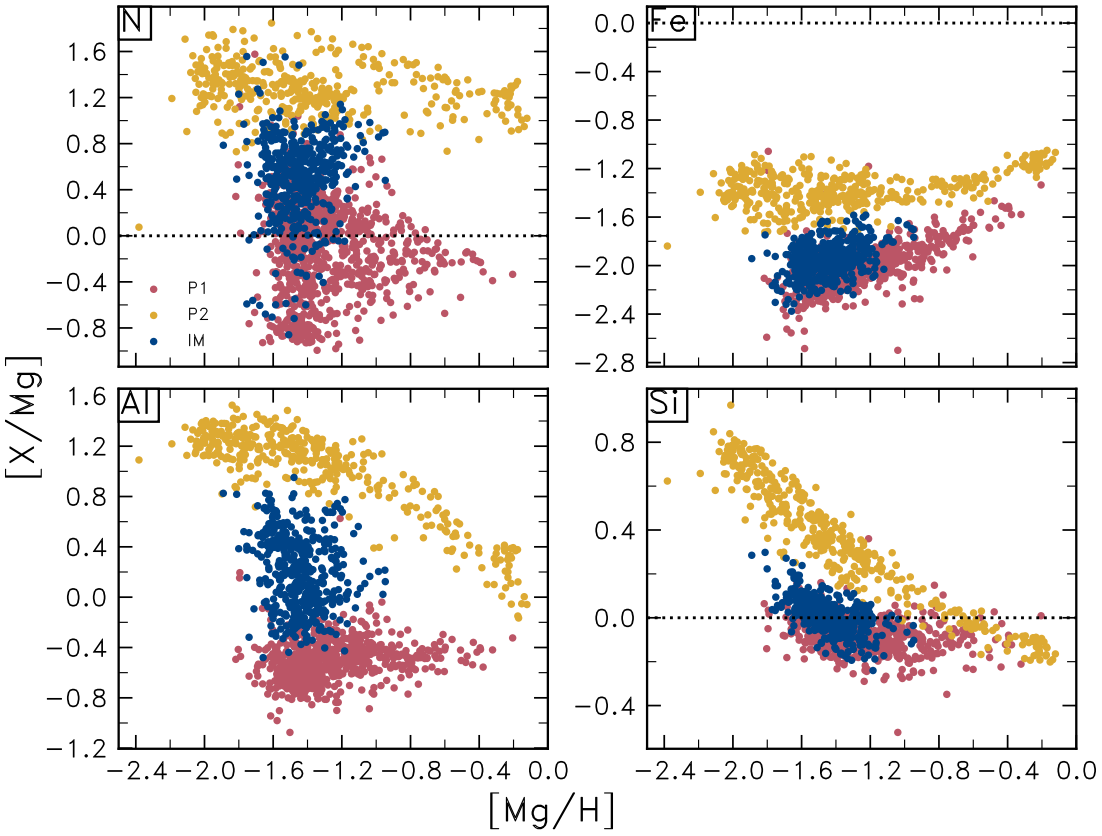

Figure 3.3: Distribution of k-means selected clusters on chemical planes, where the y-axis values are the element abundance ratios [X/Mg] for species X used in the clustering plotted as a function of [Mg/H]. Here, it becomes more obvious that the IM and P2 populations are far more distinct from one another. The Al-Mg plane in particular shows that there is a discontinuity in the abundance patterns around [Al/Mg]≃ 0.8 - it is clear that whatever produced the abundance pattern of the P2 stars must be distinct from the IM population.

(Table 3.1). For those Galactic globular clusters, we coarsely select anomalous stars by imposing the criterion that they have [Al/Fe] above the line where $[\mathrm{Al/Fe}] = m * [\mathrm{Fe/H}] + c$ with $m = 0.5$ and $c = -0.3$ (a criterion also adopted in O'Connor et. al, in prep.). We summarise their properties in Table 3.2.

Fig. 3.5 shows the GC stars identified by the above criterion on the Mg-Al plane (gray points) overlaid onto stars comprising the ω Cen IM population (black points). The agreement is remarkable, in support of our hypothesis. We may further argue that these stars are not simply the 'P2' (or 2G population, as in Milone et al., 2017b) of the P1 stars. Assuming that the onset of the MP phenomenon followed the formation of P1, it makes little sense that they would form with such an abundance pattern after the starburst.

In the following subsection, we directly map the stars comprising our P1, P2, and IM sample onto the oMEGACat chromosome map, which we derived in §3.2.2.1.

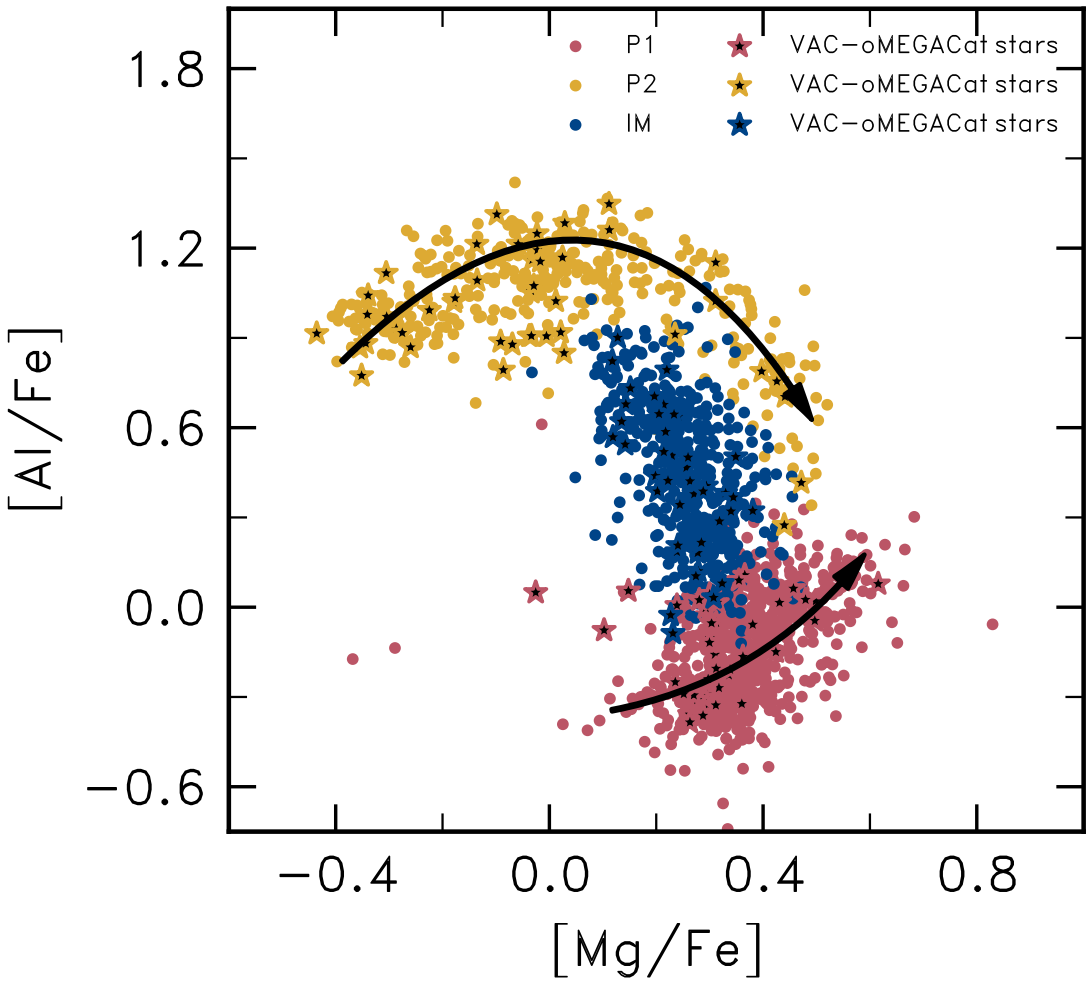

Figure 3.4: The Mg-Al anticorrelation plotted for the P1 (red), IM (blue), and P2 (yellow) populations in ω Cen. The black arrows show, approximately, the direction in which [Fe/H] evolves with [Mg/Fe]. It is remarkable that the P2 and IM populations are quite well separated, and that there is little, if any, evolution with [Fe/H] for the IM population. This is one piece of evidence that the IM population may not be the product of *in-situ* star formation at all, but rather a 'fossil population' formed by the spiralling in of a globular cluster into the centre of the ω Cen host galaxy. Stars that appear in both the VAC and oMEGACat catalogues are marked by filled stars, to illustrate that the stars exhibit the same abundance pattern as the sample they are drawn from.

3.3.6 APOGEE stars on the chromosome map

In this section, we examine how the abundance patterns exhibited by our three populations in the VAC maps into their distribution on the so-called 'chromosome map' (ChM). Fig. 3.6 shows the ChM derived from oMEGACat, as described in §3.2.2.1. Data from oMEGACat are represented as a 2d histogram where each pixel is shaded according to the (logarithmic) number of stars in 0.05 mag bins in $\Delta_{\mathrm{F275W,\ F336W,\ F435W}}$

GC name	Median [Fe/H]	$\sigma_{[Fe/H]_{2P}}$
NGC 4147	-1.63	0.06
NGC 5466	-1.81	0.09
NGC 5634	-1.72	0.06
NGC 6093	-1.61	0.004
NGC 6144	-1.80	0.00
NGC 6273	-1.71	0.14
NGC 6656	-1.70	0.10
NGC 6809	-1.76	0.08
Terzan 10	-1.62	0.10

Table 3.2: Globular clusters in the APOGEE VAC whose median P2 [Fe/H] lies within $\pm\sigma_{[Fe/H]_{IM}}$.

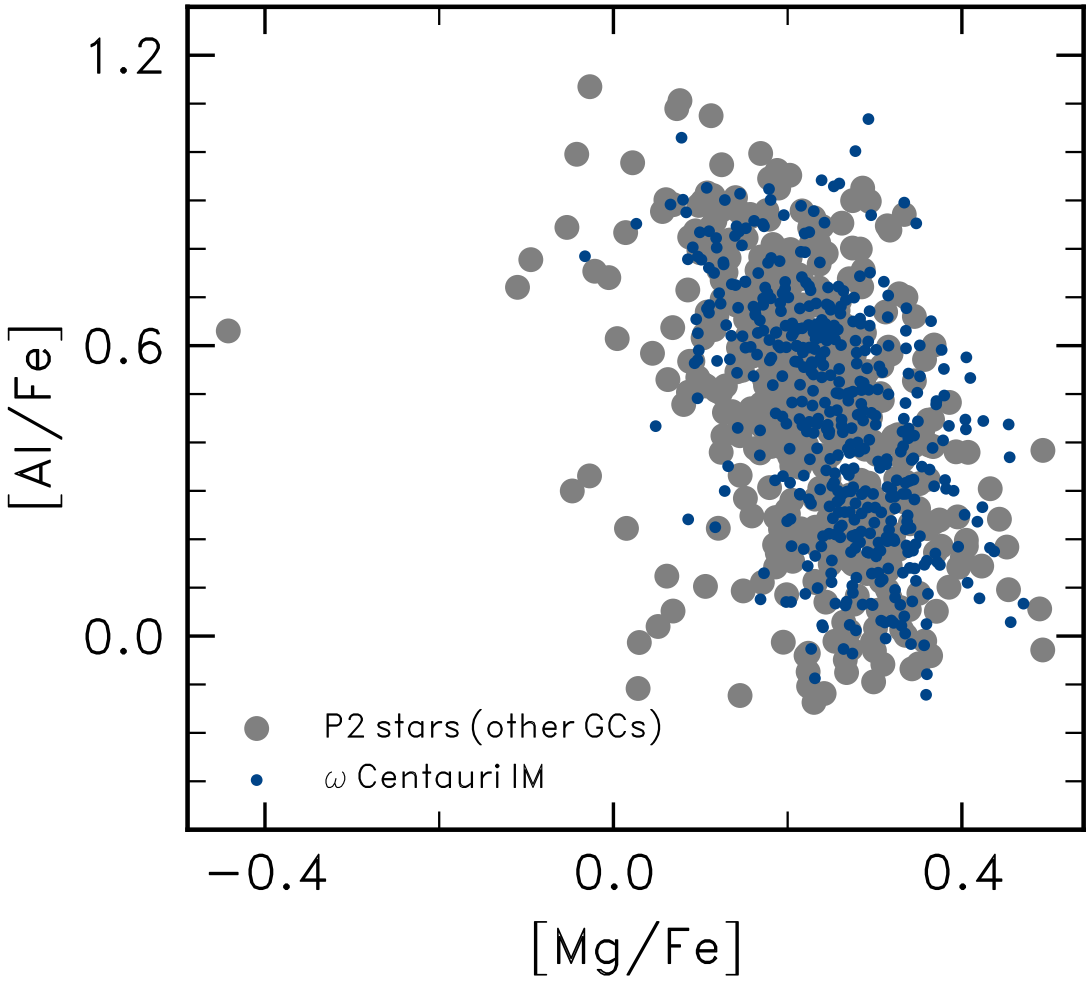

Figure 3.5: The Mg-Al anticorrelation of the IM stars identified in ω Cen, and those in other Galactic globular clusters present in the VAC whose properties are summarised in Table 3.2, having been identified as having median [Fe/H] within $\pm\sigma_{[Fe/H,\ IM]}$ of the IM population. The fact that these stars all show a distribution in this plane consistent with the IM population lends credence to the scenario whereby ω Cen experienced spiralling in of field globular clusters from its host galaxy during distant cosmic epochs.

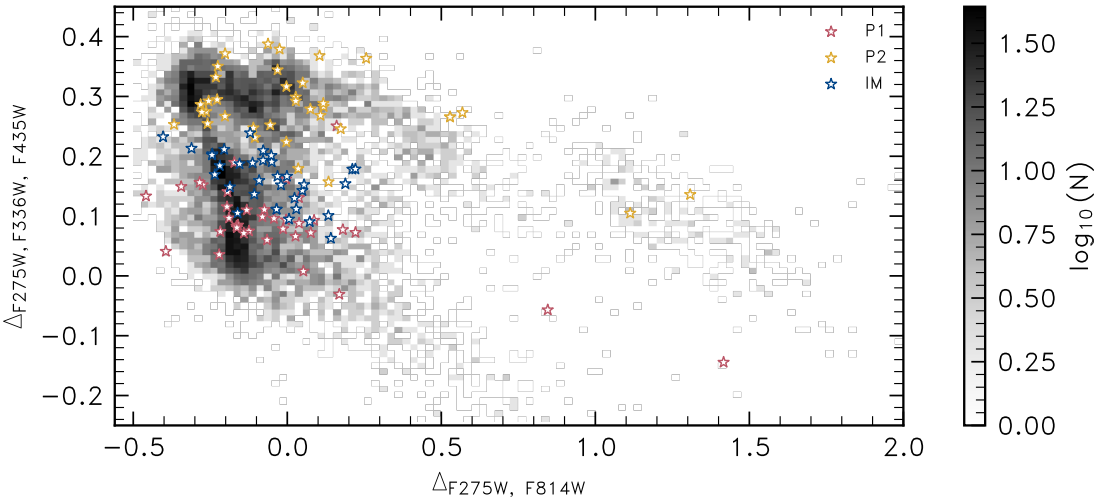

Figure 3.6: The chromosome map for ω Cen, constructed using multi-band photometry from the oMEGACat catalogue, represented as a 2d histogram where in 0.05 dex bins of $\Delta_{\rm F275W,\,F814W}$ amd $\Delta_{\rm F275W,\,F336W,\,F435W}$ each pixel shows the number of stars contained in each bin. Coloured points indicate the positions of the P1 (red), P2 (yellow), and IM (blue) stars that overlap between the VAC and oMEGACat.

and $\Delta_{\rm F275W,\,F814W}$. Adopting the same colour scheme as in Figs. 3.1-3.5, crosses show the 135 giants in common to oMEGACat and APOGEE.

Fig. 3.6 shows that the P1, P2, and IM stars occupy discrete sequences on the ChM as they do in Figs. 3.2, 3.3, and 3.4. The three sequences run roughly diagonally from the top left to the bottom right of the plane, which is associated with the metallicity variation within each population. The sequences are vertically displaced, as expected in view of their light element abundance differences.

The P2 population overlaps a locus that encompasses the overdensity at the top left of the plot ($\Delta_{\rm F275W,\,F336W,\,F435W} \simeq 0.3$), extending along a "plume" that runs diagonally towards redder $\Delta_{\rm F275W,\,F814W}$ and bluer $\Delta_{\rm F275W,\,F336W,\,F435W}$. It connects with the overdensity at $\Delta_{\rm F275W,\,F814W} \simeq 1.25$, which corresponds to the high metallicity end of P2 at [Fe/H] $\simeq -0.6$. Conversely, the P1 population is associated with the bluest $\Delta_{\rm F275W,\,F336W,\,F435W}$ sequence, although its most metal-rich stars do not seem aligned with it on the red $\Delta_{\rm F275W,\,F814W}$ end. Finally, the IM population occupies a locus at $\Delta_{\rm F275W,\,F336W,\,F435W} \simeq 0.15$, located in between the regions populated by P1 and P2, with a narrower spread in $\Delta_{\rm F275W,\,F814W}$.

The most important conclusion we draw from Fig. 3.6 is the following. The chemical complexity of ω Cen has been discussed by various groups (Johnson & Pilachowski, 2010; Milone et al., 2017a; Marino et al., 2019; Alvarez Garay et al., 2024). In particular,

studies have led to reports that there may be as many as 15 stellar populations in ω Cen on the basis of its metallicity distribution function and light element abundance patterns (Pancino et al., 2000; Sollima et al., 2005). Fig. 3.6 implies that the stellar population mix of ω Cen may in fact be simpler than previous studies have suggested. The distribution of chemically selected stellar populations (from APOGEE) on the ChM suggests that the distribution of ω Cen's stellar populations on the ChM can be explained by two components. The first component accounts for the roughly vertical displacement of substructures on the ChM. It is due to the variation in light-element abundances, associated with the multiple populations phenomenon. According to the APOGEE data, there are broadly three populations characterised by distinct abundance patterns, and their relation with metallicity. The second component explains the variation along these three sequences, whereby $\Delta_{\mathrm{F275W,\,F336W,\,F435W}}$ decreases as a function of $\Delta_{\mathrm{F275W,\,F814W}}$. That variation is associated with the spread in metallicity of each of the three populations, with P1 and P2 extending over a much wider range in colour than IM. These sequences run in parallel both on the ChM, and in the chemical planes displayed in Figs. 3.2-3.4 while displaying marked difference in their abundance patterns. This behaviour suggests that all three formed from different star formation episodes operating on distinct gas reservoirs. According to that interpretation, the distribution of stellar populations displayed in Fig. 3.6 can be understood as resulting from a bursty star formation history, so that seemingly detached substructures occurring along either of the three parallel sequences are in fact connected by a common abundance pattern, while differing chiefly in terms of overall metallicity (and in the cases of P1 and P2, possibly also in terms of age). In §3.4 we elaborate on this scenario using models of galactic chemical evolution.

3.3.7 Summary of the observational evidence

We have examined the chemical properties of each subpopulation identified on the basis of their abundances using k-means clustering. There are two populations (P1 and P2) that seem to exhibit tight correlations between abundance ratios and metallicity, which are characteristic of chemical enrichment during periods of extended star formation. Conversely, there is a population characterised by its comparative lack of an [Fe/H] spread which is consistent with that measured in other Galactic GCs present in the VAC. This population (IM) has light element abundance ratios that are intermediate to those of the P1 and P2 populations at same metallicity. Most importantly, it exhibits the well-known Mg-Al anticorrelation which strongly resembles that of other GCs.

We interpret these observations as evidence that ω Cen can broadly be described as being comprised of three populations, which formed in different episodes. One of them (IM) also shows an abundance pattern at fixed [Fe/H] that is consistent with that of monometallic metal-poor Galactic GCs, suggesting that it may result from the inspiralling of at least one GC into the central potential of ω Cen's host galaxy. Conversely, the other populations (P1 and P2) are characterised by metallicity spreads and tight correlations between metallicity and abundance ratios, which suggest that their chemical evolution was influenced by an early burst of star formation. Because the abundance ratios of these two populations differ significantly at every metallicity these bursts of star formation have likely occurred at different points in space, time, or both.

In §3.4 we speculate as to the histories of gas infall and star formation that could be responsible for the chemical evolution of the P1 and P2 populations. Following from our interpretation of its abundance patterns in §3.3, we assume that the IM population represents a typical mono-metallic GC, featuring chemical anomalies typically found in Galactic GCs. In view of the lingering uncertainties regarding the origin of such anomalies (Renzini et al., 2015; Bastian & Lardo, 2018), we refrain from modelling the chemical evolution of the IM population. Instead, we focus on the P1 and P2 populations. In §3.5 we discuss scenarios that may explain the co-existence of these three populations today within the ω Cen stellar system.

3.4 Modelling the Chemical Evolution of ω Centauri

We begin this section by describing the prescriptions adopted for the key ingredients of our models. Following that we compare our predictions with the chemical composition data available for the P1 and P2 populations. All our calculations are based on the `Versatile Integrator for Chemical Evolution (VICE)` galaxy chemical evolution modelling code (Johnson & Weinberg, 2020; Johnson et al., 2021a; Griffith et al., 2021).

3.4.1 Model prescriptions

In §3.3 we speculated that the abundance patterns shown by the P1 and P2 stars identified in ω Cen on the Al-Fe and α-Fe planes were consistent with chemical evolution that was affected by bursts of star formation, which has been seen in several Local Group Dwarfs

such as the Large Magellanic Cloud (Nidever et al., 2020b), Sagittarius dSph (Hasselquist et al., 2017), and Fornax (Hasselquist et al., 2021a; Fernandes et al., 2023b). In GCE models, bursts of star formation can be brought about by invoking either a sudden inflow of gas, or by an enhancement of the star formation efficiency. This follows from the fact that both kinds of event can significantly enhance the SFR, and thus temporarily enhance the instantaneous metal contribution by CCSNe such that it exceeds that of SNe Ia before steadily converging toward an equilibrium abundance (see Weinberg et al., 2017b, for a thorough discussion of α-enhancement due to sudden events in GCE models).

Thus, for P1 and P2 we require prescriptions in VICE that can reproduce the trend of increasing [α/Fe] as a function of [Fe/H]. In the case of P1 the characteristic 'rising' behaviour, similar to that observed in the Milky Way thick disk in the H3 and APOGEE surveys presented in Conroy et al. (2022b), perhaps indicates a period of initially inefficient star formation that was followed by a sudden enhancement of the star formation efficiency (SFE) to form the 'α-rise'. In that paper, this was attributed to a burst of star formation that coincided with the formation of the high-α disk from an initially kinematically hot population. However, to caveat this picture we point out that Chen et al. (2023b) found that such a change in the SFE was not necessary to produce the observed enhancement of [α/Fe] and that the inflow of fresh gas (i.e. 'cold mode' accretion) can also produce this behaviour.

Firstly, we adopt the widely-used linear-exponential form of the gas inflow rate as a function of cosmic time, t, by the following equation:

$$\dot{M}_{\rm in} = \frac{M_{\rm i}}{\tau_{\rm in}} \frac{t}{\tau_{\rm in}} {\rm e}^{\frac{-t}{\tau_{\rm in}}}, \tag{3.2}$$

where $M_{\rm i}$ is the inflow mass scaling factor in units $M_\odot$, and τ_{in} is the e-folding timescale in Gyr. We describe the SFE in terms of its inverse, the gas consumption timescale ($t_{\rm g}$), and assume it takes the form of a sigmoid function (as used in Mason et al., 2023) such that:

$$t_{\rm g}(t) = t_{\rm g,b} + \frac{t_{\rm g,i}}{1 + \exp\left[-k(t - t_b)\right]}, \tag{3.3}$$

where $t_{\rm g,b}$ is the final value of $t_{\rm g}$ in Gyr, $t_{\rm g,i}$ is the initial value of $t_{\rm g}$ in Gyr, k is the multiplicative factor of the exponent of the sigmoid, and t_b is the time at which the SFE begins to change.

We assume that ω Cen's P1 and P2 populations formed such that no gas enriched by either population was mixed into the other, and thus attempt to fit two separate open box single-zone models. We assume that the amount of gas removed by feedback at any

given timestep ($t_{\rm step}$) within this box is given by:

$$M_{\rm out,\ t=t_{step}} = \eta\ {\rm SFR}(t = t_{\rm step}), \tag{3.4}$$

where SFR is the star formation rate in $M_\odot$ Gyr^{-1}, η is the outflow mass loading factor in units Gyr, and $t_{\rm step}$ is the time corresponding to a given timestep in Gyr. Furthermore, we assume that the inflowing gas is *not* of a primordial composition whose abundances were set by Big Bang nucleosynthesis. Instead, in each case, we assume that the inflowing gas was of a specific composition. For P1, we assume that the chemical composition of the inflowing gas is similar to that of the halo at same [Fe/H]. For P2, we set the chemical composition of the inflowing gas to match the observed abundances of P2 stars at the low end of the [Fe/H] distribution.

We follow the procedure outlined in Johnson et al. (2023) in order to infer best-fitting models to the APOGEE data for the P1 and P2 stars identified in §3.2, adopting the above prescriptions for the metallicity of the inflowing gas, the outflow mass loading factor, the gas consumption timescale, and the history of gas inflow. There are nine free parameters in our model, given by $\theta = [L,\ t_0,\ k,\ t_{\rm g,0},\ \eta,\ \tau_{\rm in},\ t_{\rm tot},\ Z_{\rm in,\ Fe},\ Z_{\rm in,\ Mg}]$. Parameters L, t_0, k, $t_{\rm g,0}$, ν, and $\tau_{\rm in}$ are defined in Eqs. 3.2-3.4. The remaining parameters $t_{\rm tot}$, $Z_{\rm in,\ Fe}$, and $Z_{\rm in,\ Mg}$ are the total cosmic runtime of the model in Gyr, and the inflowing abundances of Fe and Mg into the box, respectively.

We assume flat, uniform priors on each model parameter with additional conditions that, for P1, ensure:

1. $0 \leq \eta < 100$ Gyr
2. $t_{\rm tot} < t_{\rm cosmo}$
3. $Z_{\rm in,\ Mg} > Z_{\rm in,\ Fe}$,

where $t_{\rm cosmo}$ is the age of the universe, taken as the Planck Collaboration et al. (2020b) value of $t_{\rm cosmo} \simeq 13.8$ Gyr (see Table 2 of that paper). For P2, we enforce identical conditions except for *(iii)* where we enforce $Z_{\rm in,\ Mg} < Z_{\rm in,\ Fe}$, drawing from a uniform priors in the ranges $Z_{\rm in,\ Mg} = 10^{-6} \times 1 - 10$ and $Z_{\rm in,\ Mg} = 10^{-5} \times 1 - 10$. We show the results of our model fit to the P1 stars in Fig. B.1, and summarise them in Table 3.3.

3.4.2 Modelling results

3.4.2.1 Initial caveats

When fitting models with large sets of free parameters, it is good practice to impose reasonable constraints on the range of values parameters should span. It is common practice in applications of GCE models to maximise the constraints by considering both the run of abundance ratios of stellar populations with metallicity and the probability density of observing a star at a given metallicity (the Metallicity Distribution Function, MDF).

The case of ω Cen is not simple in that regard. As the likely former nuclear cluster of a satellite of the Milky Way that was accreted many Gyr ago (Massari et al., 2019; Limberg et al., 2022), ω Cen must have been subject to strong tidal stripping. This has been confirmed by some studies that have detected ω Cen stars in the halo (Ibata et al., 2019; Simpson et al., 2020). There are at least two important implications of that fact to our attempts at modelling the chemical evolution of the system. First, stars of varying age and chemical composition may have been stripped over the lifetime of ω Cen, so that the MDF of the surviving stellar population may not be reflective of its history of star formation and chemical enrichment. Second, the possible occurrence of gas loss due to tidal stripping over the life of the system means that gas removal cannot be assumed to originate purely from stellar feedback, as implied by Eq. 3.4.

To address these issues, we proceed as follows. Two sets of model fits are pursued, in which the MDF is or is not used as a constraint. In this way, we can evaluate whether there is consistency between the evolution on the abundance ratios and the bulk chemical enrichment of the system. Important discrepancies in the results obtained in the two model fits could lend insights into the history of tidal stripping of the system.

Another important warning must be brought to the reader's attention at this stage. The MDFs for each population displayed in Fig. 3.1 are based on samples of several hundred stars, spread over a range of over a decade in metallicity. Such a limitation has an obvious impact on our ability to discern sharp time variations in ω Cen's star formation rate, likely caused by tidal interactions as its host galaxy collapsed under the gravity of the massive Milky Way halo. While definitely not fine-grained, the SFHs inferred from our modelling should nonetheless be able to account for the broad distribution of ω Cen's stellar populations in chemical space, hopefully shedding light on the evolutionary history leading up to its current state.

	Parameter	Value
SFE	$t_{\rm g,i}$ [Gyr]	$227\pm^{7.4}_{5.7}$
	$t_{\rm g,b}$ [Gyr]	$1.16\pm^{0.17}_{0.10}$
	$t_{\rm b}$ [Gyr]	$4.49\pm^{0.03}_{0.05}$
	k	$12.76\pm^{0.6}_{0.31}$
Inflows	$t_{\rm in}$ [Gyr]	$2.97\pm^{0.24}_{-0.26}$
	$Z_{\rm in,\ Mg}$	$0.89 \pm 0.02 \times 10^{-5}$
	$Z_{\rm in,\ Fe}$	$0.88 \pm^{0.02} \times 10^{-5}$
	η [Gyr^{-1}]	38.76 ± 0.9
Other	$t_{\rm total}$ [Gyr]	$4.99\pm^{0.36}_{0.32}$

Table 3.3: A table showing the median values of the posterior probability distributions of the model parameters for our P1 fit. Uncertainties are taken as the interquartile range of the posterior PDF.

3.4.2.2 "MDF-Constrained Models"

We start by studying models optimised to match both the distribution of stars on the Mg-Fe plane and the MDFs of the two populations. The model fit to the P1 stars favours parameters with initially inefficient star formation, characterised by a gas consumption timescale $t_g \simeq 227$ Gyr. At $t \simeq 4.49$ Gyr, t_g declines precipitously to $\simeq 1.16$ Gyr, resulting in a starburst in the gas reservoir. Gas of a halo-like composition, such that $[\mathrm{Mg/Fe}]_{\rm in} = 0.35$, flows into the box over a timescale of $t_{\rm in} = 0.40$ [Gyr]. Outflows are highly efficient in removing gas per unit star formation, such that $\eta = 38$ Gyr. The top panels of Fig. 3.7 shows the predicted model track of [Mg/Fe](t) vs. [Fe/H](t) and MDFs for the P1 model, plotted against the P1 stars identified in §3.3.

The top panels of Fig. 3.7 shows the results of our constrained models for P1. The left panel shows the observed Mg-Fe plane, with a solid line indicating the model corresponding to the median parameters of the posterior probability distribution produced by the fitting. The shaded region indicates 1000 realisations of models with parameters randomly drawn, with values ranging between the 16$^{\rm th}$ and 84$^{\rm th}$ percentiles of the posterior PDF. The right panel shows the observed MDF as a histogram in 0.05 dex bins of [Fe/H]. The solid line corresponds to the model prediction generated for the median parameters of the posterior probability distribution. The shaded region shows the 16$^{\rm th}$ to 84$^{\rm th}$ percentiles of the distribution of predictions resulting from the 1,000 model realisations. Overall, a good match to the data is achieved. The normalisation

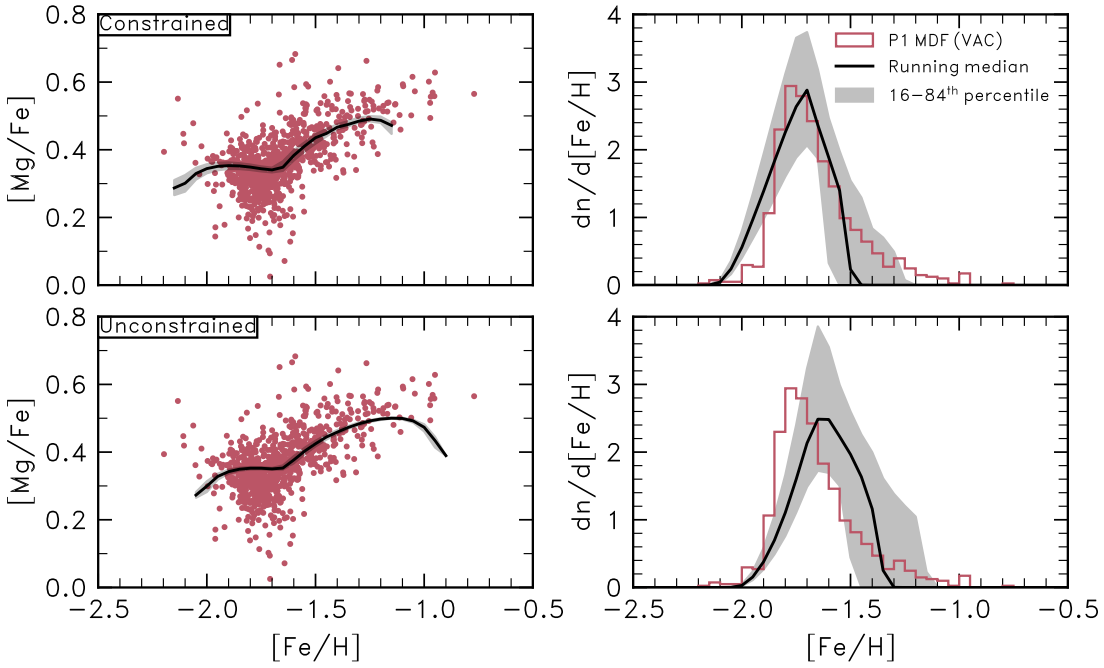

Figure 3.7: MDFs and Mg-Fe planes from the model fits to the P1 stars, where black solid lines correspond to the model corresponding to the median of the posterior PDFs shown in Fig. B.1. In each case, MDFs generated by the model have been convolved with the median uncertainty in [Fe/H] in the APOGEE VAC for P1 stars in ω Cen. The top and bottom rows correspond to the models described in §3.4.2 and §3.4.2, respectively. Grey shaded regions indicate the range of MDFs and abundance tracks produced by randomly sampling model parameters about between the 16$^{\text{th}}$ and 84$^{\text{th}}$ percentiles of the posterior probability distributions produced by the procedure of Johnson et al. (2023). The precipitous decline in the probability density of stars with [Fe/H]> -1.7 reflects the rapid consumption of the star-forming gas following the onset of the starburst.

and shape of the MDF is reproduced, along with the [Fe/H] corresponding to the peak of the MDF. However, the model under-predicts the number of metal-rich stars.

The top panels of Fig. 3.8 and Table 3.4 show, respectively, the predicted Mg-Fe planes and MDF as in Fig. 3.7; and the best-fit model parameters for the P2 stars obtained as a result of applying the method of Johnson et al. (2023). The abundance patterns of the P2 population necessitate the inflowing gas to have abundances characteristic of the so-called 'extreme' populations seen in some Galactic globular clusters, such that $[\text{Mg/Fe}]_{\text{initial}} \simeq -0.60$. We do not include prescriptions for any of the purported progenitors responsible for these abundance patterns, and instead assume that they have already contributed their metals to the gas reservoir. Subsequent star formation, and chemical evolution from this initial abundance pattern, is driven by a combination of SN II, SN Ia, and AGB stars

	Parameter	Value
SFE	$t_{g,i}$ [Gyr]	$235\pm^{5}_{6}$
	$t_{g,b}$ [Gyr]	$1.51\pm^{0.06}_{0.09}$
	t_{b} [Gyr]	$4.43\pm^{0.71}_{0.92}$
	k	$16.5\pm^{0.8}_{0.6}$
Inflows	t_{in} [Gyr]	$0.3\pm^{0.01}_{0.01}$
	$Z_{in,\ Mg}$	$1.0 \pm 0.06 \times 10^{-6}$
	$Z_{in,\ Fe}$	$2.46 \pm^{0.07}_{0.04} \times 10^{-5}$
	η [Gyr^{-1}]	18.8 ± 0.68
Other	t_{total} [Gyr]	4.89 ± 0.06

Table 3.4: A table showing the median values of the posterior probability distributions of the model parameters for our P2 fit. Uncertainties are taken as the interquartile range of the posterior PDF.

Before the starburst, the P2 model generally agrees well with the MDF as seen in the left panel of Fig. 3.8. However, the model significantly over-predicts the number of stars formed from the starburst, which is readily explained. Our modelling sugests that these stars form over the course of a continuous history of star formation, and not a bursty one where there can be periods of quiescence or even temporary quenching of star formation, during which time gas mass can be lost due to sources of feedback and stripping. This assumption may be valid for P1, but there is some observational evidence that the most metal-rich ([Fe/H]>-1.2) stars in P2 may have formed later, subsequent to some loss of gas from the system. Fig. 3.6 shows that there is a significant discontinuity between the most metal-rich P2 stars and the main body of the P2 stars on the ChM. This may in fact reflect such a pause in the SFR, during which time gas was removed. A subsequent burst would explain the low number of metal-rich P2 stars.

3.4.2.3 Models without MDF constraints: a new mass budget problem

In this Section we examine the performance of models optimised without the imposition of an MDF constraint. The results are displayed in the bottom panels of Figs. 3.7 and 3.8. For both P1 and P2 populations, the match to the run of [Mg/Fe] vs [Fe/H] is only marginally improved—a little more so in the case of P1, whose metallicity now extends beyond [Fe/H]$\simeq$–1.2. Unsurprisingly, the biggest changes take place in the MDF predictions, which in both cases get shifted to greater power towards the high metallicity end. The variation is more extreme in the case of P1, which presented a fairly good

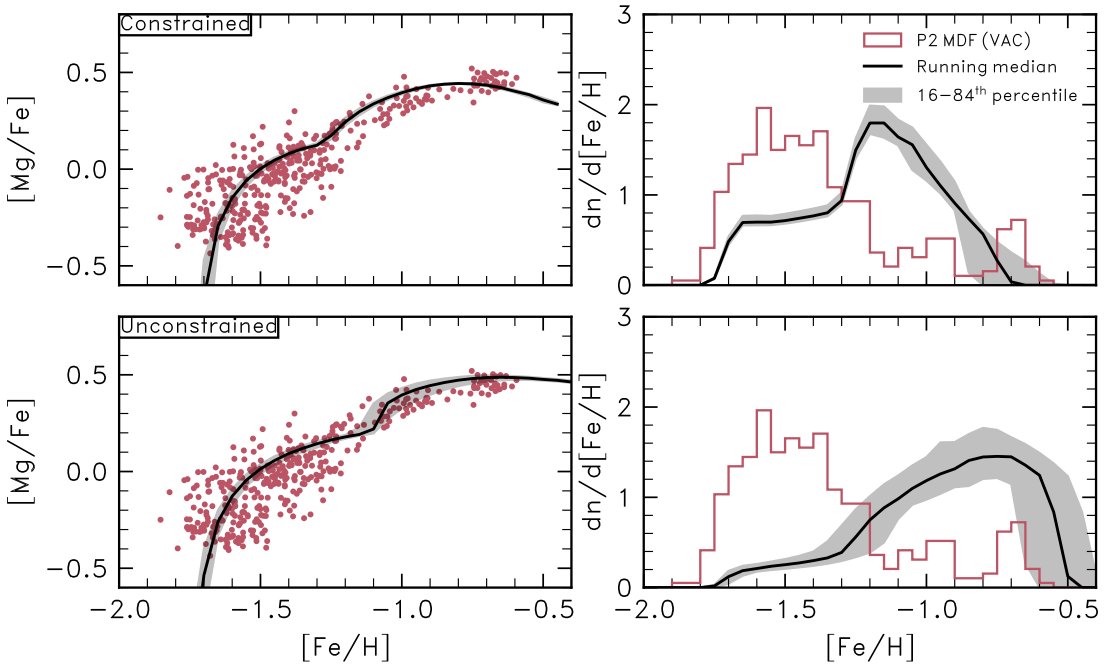

Figure 3.8: MDFs and Mg-Fe planes from the model fits to the p2 stars, where black solid lines correspond to the model corresponding to the median of the posterior PDFs shown in Fig. B.2. In each case, MDFs generated by the model have been convolved with the median uncertainty in [Fe/H] in the APOGEE VAC for P2 stars in ω Cen. The top and bottom rows correspond to the models described in REF and REF, respectively. Grey shaded regions indicate the range of MDFs and abundance tracks produced by randomly sampling model parameters about between the 16th and 84th percentiles of the posterior probability distributions produced by the procedure of Johnson et al. (2023). Both models over-predict the abundance of metal-rich ([Fe/H]> -1.2) stars to varying degrees, in spite of successfully reproducing the abundance pattern of P2. This over-abundance can be attributed to the prescription of a continuous SFH - if there was a period of less-intense star formation during which gas was stripped from the cluster, followed by a fresh round of more intense star formation from the diminished gas reservoir, this could explain the relative paucity of metal-rich stars, and why the model is unsuccessful. Alternatively, these stars could have been stripped during interactions with the Milky Way.

match in the "constrained" case, and now displays a sizeable wing towards [Fe/H]$\gtrsim$–1.5. In the case of P2, most of the power is now located at [Fe/H]$\gtrsim$–1.2, in sharp constrast with the populations observed MDF.

These results suggest the presence of an inconsistency between the apparent evolution of both populations in the Mg-Fe plane and their MDFs. They suggest that, in order to produce the strong increase in [Mg/Fe] observed towards the metal-rich half of both populations, the system must undergo a strong burst of star formation, thus producing an over- abundance of metal-rich stars which are not observed. This new type of *mass budget problem* can be explained away in two possible ways. In one scenario, it can be

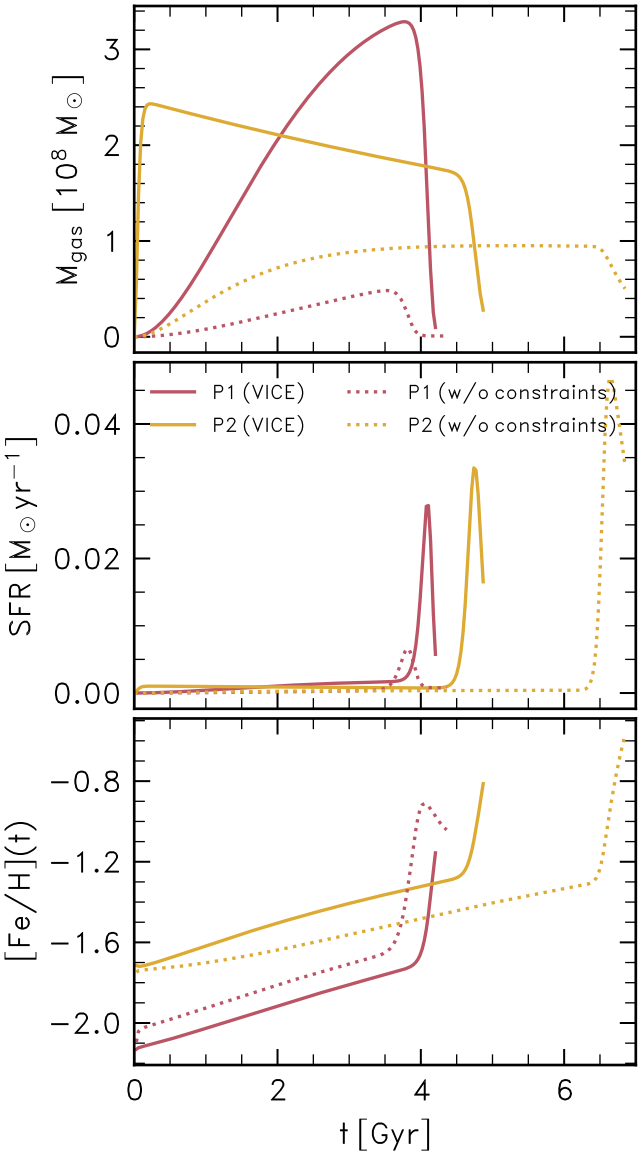

Figure 3.9: Histories of gas infall, star formation, and Fe-evolution with cosmic time from the models corresponding to the median parameters drawn from the posterior PDFs of our model fits to the P1 and P2 samples, also seen in Figs. 3.7 and 3.8.

argued that these metal-rich stars were actually formed, but due to their being somehow less bound to the system they were tidal-stripped through interaction with the Milky Way host halo. Alternatively, gas stripping could be responsible for the mismatch between the predicted and observed MDFs. The prescription for outflows due to stellar feedback (eq. 3.4) are likely too simplistic to represent a situation where gas may have been tidally stripped through interaction with the host halo, nor does our model allow for temporary quenching of star formation. Indeed, continued interaction between an infalling satellite galaxy and the host halo can lead to the complete removal of the star forming gas, as well as star formation bursts. Such events may single-handedly explain the discrepancies

observed between the model and observed MDFs we showed in Figs. 3.7 and 3.8.

Fig. 3.9 shows the histories of gas infall and star formation of the P1 and P2 populations, as well as their predicted age-metallicity relation. A spread in age of $\simeq$ 4 Gyr is predicted for both populations. In both cases, the burst of star formation is predicted to have occurred in the latest stages of the chemical evolution of both populations, being associated with the formation of their most metal-rich stars. Interestingly, it is in this regime that important discrepancies between observed and predicted MDFs are found. We further elaborate on this result in Section 3.5.

3.4.3 Summary of results from GCE modelling

Employing the `VICE` GCE modelling code, we have derived best-fitting GCE models to the P1 and P2 populations in ω Cen, under the hypothesis that these populations evolved in chemical detachment. This assumption is well-motivated by an inspection of the chemical abundance patterns evident in Figure 3.2. By optimising parameters dictating the evolution of gas infall, outflows, and star formation efficiency, we find that the models predict that both populations underwent a burst of star formation, preceded by a few Gyr of low star forming rate. The GCE models are a good match to the distribution of both P1 and P2 stars on the Mg-Fe plane, but fail to reproduce their MDFs. The mismatch is of course exacerbated when MDFs are not adopted as constraints in the optimisation. In both cases the best-fitting models predict an excess of metal-rich populations formed during the bursts of star formation.

In the following section, we first compare the data and our interpretations to other studies of the chemical composition of ω Cen stars. Following that, we perform a chemical comparison between the P1 stars of ω Cen and the field stars of accreted dwarf galaxies in the Milky Way's stellar halo in an attempt to constrain the nature of ω Cen's parent population. Finally, we tie in our chemical tagging of the P1, P2 and IM stars in the VAC with the larger observational state of play concerning ω Cen.

3.5 The Multiple Populations of ω-Centauri in the GCE context

In §3.3 and 3.4, we presented a complementary view of the abundance pattern variations in ω Cen afforded by a combination of precise chemical abundances from the

APOGEE VAC, and the oMEGACat catalogue, mapping the abundance patterns of its stellar populations into sequences on the chromosome map. Furthermore, we presented exploratory galaxy chemical evolution models that attempt to explain these abundance patterns in terms of episodes of star formation occurring in star-forming gas reservoirs with markedly different compositions. In this section, we briefly comment on our selection of the different populations in ω Cen in relation to other studies that have used spectroscopically derived abundances of individual stars in the cluster. Then, we discuss the shortcomings of the GCE models described in §3.4, particularly in relation to the MDF of P2 and the implications of the model's failure to reproduce it. Then, we speculate as to the origin of the intermediate and P2 populations, which are both characterised by the anomalous abundance patterns associated with the Galactic GCs. Finally, under the assumption that our P1 sample comprises former field stars of the progenitor of ω Cen, we perform chemical comparisons between these stars and other stars belonging to substructure identified in the literature, particularly ones where there has been a speculative link to ω Cen's progenitor.

3.5.1 On the role of gas mass loss in shaping the MDF of P2

In §3.4, we fitted GCE models on the basis of the Mg-Fe plane of the P1 and P2 samples constructed in §3.2. The underlying assumptions of these models were that after a period of initially inefficient star formation, the star formation rate was suddenly enhanced without the inflow of additional gas due to a sudden increase in the star formation efficiency. Such a starburst (dubbed an 'efficiency-driven starburst', e.g. Nidever et al., 2020b; Johnson & Weinberg, 2020) is markedly different from one driven by accretion, as it simply marks an enhancement in the consumption of the available gas, enhancing the rate of SN II enrichment relative to that of SN Ia from antecedent star formation. Such a burst could be driven by a dynamical disturbance to the existing gas supply.

What Fig. 3.8 shows is that at the onset of the starburst, there is too much gas available in the reservoir and thus the number of stars at [Fe/H]$\gtrsim -1.2$ is vastly over-predicted by the model. Fig. 3.3.6 indicates that the sequence on the ChM corresponding to our P2 sample is characterised by a dearth of stars between $\Delta_{\mathrm{F275W,\ F814W}}$. The stars comprising the overdensity at $\Delta_{\mathrm{F275W,\ F814W}} \simeq 1.25$ are located on the locus on the Mg-Fe plane that must have formed during the starburst, characterised by constant [Si/Fe], enhancement in [Mg/Fe], and enhanced [N/Fe] as a function of [Fe/H] (see stars with [Fe/H]$\gtrsim -1.2$

in Fig. 3.2). This 'gap' on the ChM is also seen in M54 (Milone et al., 2017a), a system understood to have experienced a bursty history of star formation and boasting metal-rich populations like ω Cen (Bellazzini et al., 2008), combined with the gradual stripping of its gas during its interaction with the Milky Way. Thus, we conclude that there may have been a temporary period of low-intensity or quenched star formation, during which a significant fraction of the gas reservoir was removed from ω Cen. A subsequent burst of star formation formed the metal-rich stars of P2.

3.5.2 The origin of the IM population

In §3.3 we compared the abundance patterns of the intermediate population to the 'P2' populations of Galactic globular clusters at the same metallicity. We found that not only are their metallicity spreads consistent with those of the IM population, they also show the same abundance anticorrelations expected of chemically anomalous populations in those GCs. Fig. 3.3 also indicates that the P2 and IM populations in ω Cen exhibit significantly different abundance patterns - P2 is significantly more enhanced in Si and Al.

We argue that the IM stars *cannot* be indicative of the MP phenomenon polluting the gas reservoir from which the P1 stars formed. The starburst behaviour of P1 precludes that hypothesis. Instead, we speculate that this population may well be the result of globular clusters spiralling into the centre of ω Cen at early times. ω Cen has long been speculated to be a nuclear star cluster, the nucleated remnant of a satellite that merged with the Galaxy. These systems are hypothesised to grow by the spiralling in of the host galaxy's field clusters by dynamical friction, in-situ star formation, or most likely a combination of both. Assuming a typical ratio between NSC and host galaxy mass, ω Cen was likely hosted by a galaxy with $M_\star \simeq 10^9$ M$_\odot$ which is in the mass regime where both processes contribute to NSC growth (Fahrion et al., 2021). Thus, given its apparent chemical disconnect with the P1 and P2 populations and the fact that it exhibits the standard Mg-Al anti-correlation, it is reasonable to assume that the IM population originates from the inspiralling of metal-poor GCs towards the centre of ω Cen's host galaxy.

3.5.3 On the origin of the P1 and P2 populations

Having a working hypothesis for how the IM population has happened upon ω Cen, we now turn to an interpretation of our results for the P1 and P2 populations. A critical aspect of our approach is that we choose to model the chemical evolution of the two populations separately, without attempting to establish a chemical evolution link between them. By proceeding in that way we renounce any ambition to devise a fully consistent model for the chemodynamic evolution of the ω Cen stellar system. Indeed, formulating a chemical link between populations such as P1 and P2 is a proposition that has eluded the community for well over a decade (see the discussion by Bastian & Lardo, 2018), and is beyond the scope of this work. Our focus instead is on understanding what type of star formation and chemical evolution histories can produce such a unique distribution of chemical properties as observed in ω Cen. In doing so we hope to gain new insights into the history of this peculiar system.

We start by looking at the evidence for the occurrence of star forming bursts in these systems. As discussed in Sections 3.3, a steep relation between abundance ratios such as [Mg/Fe] and [Al/Fe] and [Fe/H] is a tell tale sign of a burst of star formation, as it implies a preponderance of enrichment by massive stars (e.g., Hasselquist et al., 2021a; Fernandes et al., 2023b). Indeed, optimisation of GCE model parameters using the `VICE` code results in SFHs characterised by low level star formation followed by a strong burst for both P1 and P2 (Fig. 3.9). We note that the starting time for both models is completely arbitrary, so that age differences implied by the SFHs displayed in Fig. 3.9) have no physical meaning.

Bursts of star formation can be triggered by interactions between infalling satellites and their hosts (e.g., Bekki & Freeman, 2003; Emsellem & van de Ven, 2008; Pearson et al., 2019). In addition, such episodes of star formation in infalling satellites are accompanied by gas stripping through various processes, such as tidal forces, dynamical friction, and stellar feedback (Bassino et al., 1994; Pfeffer & Baumgardt, 2013). In this context, it may be possible to understand the MDF mismatch displayed in Figs. 3.7 and 3.8 as a by-product of the merger process just as much as the bursts of star formation themselves. In other words, the deficit in metal-rich stars (particularly important in the case of P2), may be the result of the loss of metal-rich gas incurred during the accretion of the ω Cen host into the halo of the Milky Way. This gas mass deficit would then account for the reduced impact of the star formation burst on the final stellar mass budget of ω Cen, explaining the MDF mismatches.

3.5.4 Putting the pieces together: a hypothetical scenario for the genesis of ω Cen

Before proceeding, it is suitable that we take stock of where we are with the different pieces of the puzzle. According to our k-means analysis (Section 3.3), ω Cen hosts three stellar populations, characterised by distinct chemistry. One population (IM) is likely the result of the inspiralling of one or more metal-poor GCs into the centre of the ω Cen host galaxy. The remaining populations are P1, which is characterised by abundance ratios that are akin to those of halo field stars at same metallicity, whereas P2 displays extreme second-generation GC chemistry. The two populations seem to have undergone separate histories of star formation and chemical enrichment, both characterised by a period of "simmering" star formation, followed by a starburst.

Since the P1 burst is triggered at a time when the gas has substantially lower metallicity than P2 ([Fe/H]≈–1.7 as opposed to ≈–1.3), it is reasonable to suppose that the P1 burst took place at an earlier time. This notion is further supported by the fact that the models predict a longer period of "simmering" star formation for P2 than for P1 (Fig. 3.9). Thus the evidence favours the P1 burst having occurred first.

A possible scenario would thus start with P1 as the direct chemical descendant of the primordial stellar population residing in the centre of the ω Cen host galaxy. Steady conversion of gas into stars at a low rate proceeded until the falling into the Milky Way halo triggered a burst of star formation. Interaction with the Milky Way could then have led to a quenching of the star formation rate, due to gas loss associated with tidal stripping, harassment, and/or feedback.

The P1 hypothesis being accepted, one is then left with the difficult question regarding the origin of the gas from which the P2 population was formed. As mentioned above, this is a fundamental unsolved problem in the present understanding of GC formation (see, e.g., Renzini et al., 2015; Bastian & Lardo, 2018). It is beyond the scope of this work to attempt a solution, so we simply take the existence of multiple populations in GCs for granted. What follows are mere speculations based on the information at hand.

We have assumed that the P1 and P2 populations evolved in chemical detachment. At first glance this assumption may seem unreasonable in view of the fact that these two populations are tightly co-located today in a dense environment. The obvious competing scenario would be one according to which the system underwent accretion of gas with the chemical composition needed to, upon mixing with the existing *in situ* gas, dilute

its chemical composition so as to next form stars with the abundance ratios observed in the metal-poor end of the P2 population. Looking at Figure 3.3, that would require, for instance, a decrease of ≃1.6 dex in [Mg/H] and 3 dex in [Al/H]. In short, the chemistry of the early P2 populations is so exceptional that for it to result from mixing with pre-existing evolved P1 gas would call for infall gas abundances that may be unreasonably extreme. While worth mentioning it, we deem this scenario unlikely.

A possible source for the gas that formed P2 is the inspiralling GC(s) that gave origin to the IM population. Given that the IM stars clearly processed material polluted by the progenitors that give rise to the MP phenomenon, it is possible that the inspiralling of their host GC(s) brought gas whose abundances were characteristic of this extreme abundance pattern. Such stars are also found in even larger amounts in the field (e.g., Schiavon et al., 2017a; Fernández-Trincado et al., 2019; Kisku et al., 2021; Horta et al., 2021d; Phillips et al., 2022; Belokurov & Kravtsov, 2023b).

While at present we lack a clear definition of what process is responsible for this phenomenon, there is no question about its ability to generate enough gas to form $\approx 10^6$ $M_\odot$ in 2G stars within the most massive GCs. These inspiralling GC(s) would likely be forming the early P2 stars at a low level of star formation, but then infall of such a large amount of dense gas into the core of ω Cen's host galaxy may trigger a second burst of star formation, responsible for the production of the metal-rich P2 stars observed in ω Cen today. Stripping of that gas partly during the inspiralling into the host galaxy, and partly due to feedback and harassment by the Milky Way may be responsible for the "metal-rich mass budget problem" laid bare by the MDF comparisons of Fig. 3.8.

3.5.5 Can we identify the remains of ω Cen's host galaxy on the basis of chemistry?

As we discussed in §3.1, there may be a genetic link between ω Cen and accreted populations in the Milky Way's stellar halo. The two most prominent candidates suggested to date for ω Cen's former host system are the Sausage/Gaia Enceladus (Belokurov et al., 2018b; Helmi et al., 2018) and the Sequoia (Myeong et al., 2019).

Horta et al. (2023a) utilised a χ^2 method on the basis of APOGEE data to compare the chemical abundance patterns of substructures in the Milky Way stellar halo to *in-situ* stars at the same metallicity. Notable inclusions in the analysis were Heracles (Horta et al., 2021b), the Sausage/Gaia-Enceladus, the Sagittarius dSph (Ibata et al., 1994b),

the Helmi stream (Helmi et al., 1999), and Sequoia (Barbá et al., 2019; Myeong et al., 2019).

We perform the same exercise, comparing the abundances of the Sausage/Gaia-Enceladus, Sequoia, Heracles, and Aurora (Belokurov & Kravtsov, 2022; Myeong et al., 2022) to the P1 stars in the VAC. That is based on the assumption that P1 stars resemble the field stars of ω Cen's progenitor—no substructure identified in the literature to date is wholly characterised by abundance patterns consistent with P2/IM. Aurora is purportedly the *in-situ* relic of the Milky Way prior to the onset of the formation of the disk, characterised by hot kinematics, an isotropic velocity ellipsoid, and slight rotation.

To briefly summarise the method presented in Horta et al. (2023a), for each population considered we make corrections to the abundances to account for systematic abundance variations with log(g), which can be caused by a combination of stellar evolution or systematic effects as a function of stellar parameters (see Weinberg et al., 2022, for a thorough discussion). We make these corrections, restricting our sample to stars with $1 < \log(g) < 2$, and fit second order polynomials to the relationship between $\log(g)$ and [X/H] for every species in the comparison (X$\in$ [O, Mg, Si, S, Ca, Ti, C, N, Al, K, Mn, Ni, Ce]). Corrections are made by subtracting the difference between the polynomial fit to the data and the observed abundance.

Following the correction of the abundances, for each substructure we determined the uncertainties of the abundances using a boostrapping resampling method, generating 1000 realisations of the X-Fe planes of every substructure considered, for every species X. For each one of the boostrapped realisations of a chemical abundance plane for a given substructure, the [X/Fe] value at $[\mathrm{Fe/H}]_{\mathrm{comp}}=-1.7 \pm \sigma_{[\mathrm{Fe/H}]_{\mathrm{P1}}}$ and $[\mathrm{Fe/H}]_{\mathrm{comp}}=-1.2 \pm \sigma_{[\mathrm{Fe/H}]_{\mathrm{P1}}}$. This yields 1000 median [X/Fe] values for the 13 elements adopted for the comparison, from which we compute the mean and standard deviations of [X/Fe], using them to compare the chemical abundances between the two populations.

With the means and uncertainties computed for every abundance [X/Fe] at our values of $[\mathrm{Fe/H}]_{\mathrm{comp}}$, we quantitatively compare the chemical compositions of the P1 stars in relation to other halo substructures by computing a χ^2 statistic to assess the similarity. This is given by Eq. 1 in Horta et al. (2023a), given by:

$$\chi^2 = \sum_i \frac{([\mathrm{X/Fe}]_{\mathrm{i,sub}} - [\mathrm{X/Fe}]_{i,\mathrm{P1}})^2}{(\sigma^2_{[\mathrm{X/Fe}]_{i,\mathrm{sub}}} + \sigma^2_{[\mathrm{X/Fe}]_{i,\mathrm{P1}}})}, \tag{3.5}$$

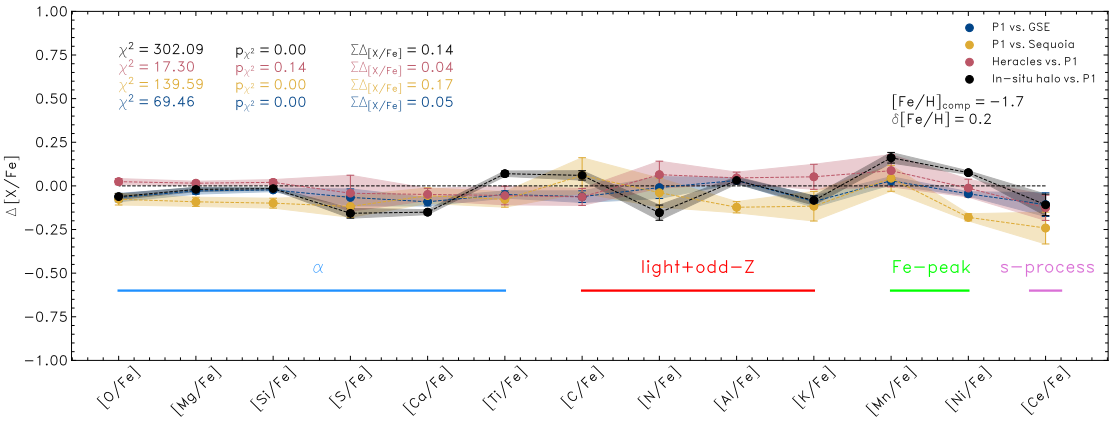

Figure 3.10: Δ[X/Fe] differences between the resulting mean values obtained using the method presented in §5 of Horta et al. (2023a) in 13 different chemical abundance planes at [Fe/H]=-1.7±$\sigma_{[\mathrm{Fe/H}]_{\mathrm{P1}}}$. Here we compare the stars comprising P1 to the *i)* Sausage/Gaia Enceladus (navy), *ii)* Sequoia, *iii)* Heracles, and *iv)* a sample of *in-situ* halo stars.

where $[\mathrm{X/Fe}]_{\mathrm{i,sub}}$ and $[\mathrm{X/Fe}]_{i,\mathrm{P1}}$ are the abundances of a given halo substructure and the P1 stars, respectively. $\sigma^2_{[\mathrm{X/Fe}]_{i,\mathrm{sub}}}$ and $\sigma^2_{[\mathrm{X/Fe}]_{i,\mathrm{P1}}}$ are the corresponding uncertainties for those abundances. We then compute the p-value for the χ^2 statistic for 12 degrees of separation using `scipy`'s `scipy.stats.chi2.cdf` routine, where we interpret a value of $p_{\chi^2} < 0.05$ as an indication that the abundances of a given substructure have a high degree of certainty that they are *not* drawn from the same distributions as the P1 stars. Finally, we also compute the sum of the differences, $\sum \Delta_{[\mathrm{X/Fe}]}$, given by the numerator of Eq. 3.5.

Fig. 3.10 shows the results of the method applied at $[\mathrm{Fe/H}]_{\mathrm{comp}} = -1.7$, comparing stars in a given substructure to P1 stars at this metallicity $\pm\sigma_{[\mathrm{Fe/H}]_{\mathrm{P1}}}$. This plot excludes the Aurora population, whose metallicities are too high for this comparison. The sample of *in-situ* stars (represented by black points and tracks) was chosen to mimic the same selection in Conroy et al. (2022b) (who adopted a left-handed coordinate frame, hence we select stars with $L_z > 500$ kms^{-1}kpc^{-1} and $e < 0.8$), and they show the largest disagreement with the abundances of P1, followed by Sequoia. On this basis, the data rule out an *in-situ* origin for ω Cen or an association with Sequoia. Conversely, the substructures that show the most similarity to the P1 stars are the Sausage/Gaia-Enceladus (blue points and tracks), and Heracles (red points and tracks) with Heracles' p_{χ^2} value (0.014) formally exceeding the threshold for rejecting the null hypothesis that the substructures are chemically distinct from one another.

Fig. 3.11 shows the results of the method applied at $[\mathrm{Fe/H}] = -1.2$, comparing stars within $\pm\sigma_{[\mathrm{Fe/H}]_{\mathrm{P1}}}$. This time our sample for Aurora is included. As shown in Fig. 1

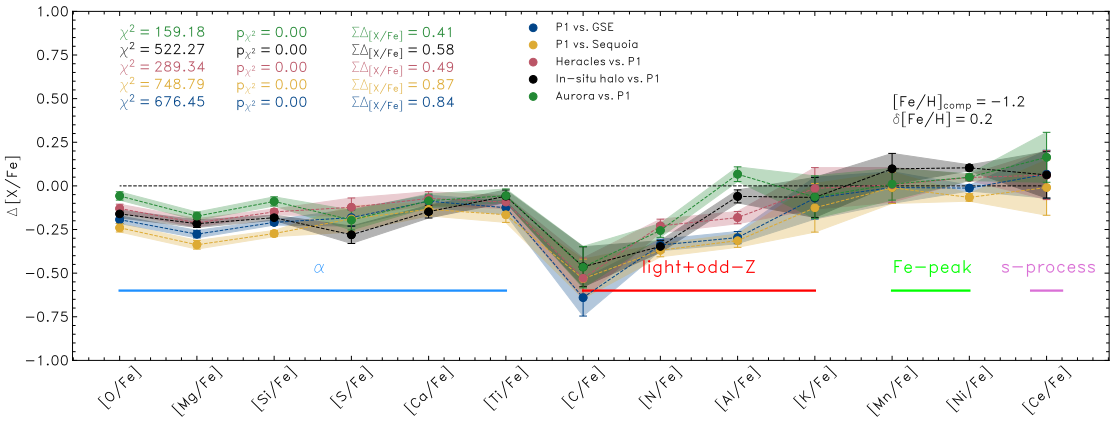

Figure 3.11: Δ[X/Fe] differences between the resulting mean values obtained using the method presented in §5 of Horta et al. (2023a) in 13 different chemical abundance planes at [Fe/H]=-1.2±$\sigma_{[Fe/H]_{P1}}$. Here we compare the stars comprising P1 to the *i)* Aurora (green) *ii)* Sausage/Gaia Enceladus (navy), *iii)* Sequoia, *iv)* Heracles, and *v)* a sample of *in-situ* halo stars.

of Myeong et al. (2022), Aurora is characterised by its rising α and Al abundances as a function of [Fe/H], in addition to its placement in the so-called 'accreted region' in the [Mg/Mn]-[Al/Fe] plane (a chemical plane often used as a diagnostic plot to distinguished accreted from *in-situ* populations; e.g. Das et al., 2020; Horta et al., 2021b; Vasini et al., 2024). In this metallicity range around $[Fe/H]_{comp}$, however, none of the accreted substructures that we compare against the P1 stars exhibits the same abundance pattern as P1. This is unsurprising - for example, P1 exhibits α-abundances up to a factor of $\simeq 2$ higher than those in these substructures at the same metallicity ($[Mg/Fe]_{P1,\ [Fe/H]_{comp}} \approx 0.5$). None of these substructures exhibits as extreme an abundance pattern as what we see in P1, though this is unsurprising given the scenario we advocate here. The stars comprising these substructures, now part of the field, formed over the course of the secular galaxy evolution of the Milky Way system. In marked contrast, P1 formed during the nucleation of the ω Cen host galaxy, an entirely different environment.

The similarity between P1 and Heracles that we see in our statistical comparison of the two samples at low [Fe/H] could hint to a genetic link between these two populations. However, there is no such similarity in our higher [Fe/H] sample. Thus, if ω Cen's P1 stars are connected to Heracles by a common abundance pattern, it is only at low [Fe/H]. A scenario whereby the Heracles progenitor interacted with the Milky Way, depositing its field stars exclusively in the Galactic centre, while its nucleated remnant remains on a coplanar orbit with the disk at $z = 0$ strains credulity. We thus conclude that none of

the known halo substructures contained in the APOGEE DR17 catalogue has a chemical composition suggestive of an association with ω Cen.

3.5.6 Open questions

The highly speculative scenario presented in §3.5.2 and §3.5.4 accounts for some of the broad properties of the ω Cen stellar system, but leaves a number of questions unanswered. It is critical that they are stated clearly, and we enumerate them below.

1. *How much mass did ω Cen lose?* Consider the *metal-rich mass budget problem*. Our scenario explains away the metal-rich MDF mismatch (Figs. 3.7 and 3.8) as being caused predominantly by loss of gas due to tidal stripping and harassment. Nevertheless, there is strong evidence that ω Cen lost substantial mass in the form of stars (e.g., Anguiano et al., in prep., Pagnini et al. 2024, A&A, submitted, Simpson et al., 2020; Ibata et al., 2019). A reliable estimate of the amount of stellar mass lost by ω Cen over the past many Gyr will have to await the chemical tagging of a statistically robust halo field sample. On the other hand, we have no means of ascertaining the total gas mass lost. However, if the model predictions displayed in Figs. 3.7 and 3.8 are accurate, one would reasonably conclude that it lost most of its mass to the field, predominantly in the form of P2 stars or gas.

2. *Are the extreme abundance ratios of the P2 population a feature of Nuclear Star Clusters?* We hypothesize that the P2 population is the result of the conversion of 2G gas present in the GC(s) that spiralled into the centre of ω Cen's host galaxy. Figs. 3.2 and 3.3 show that P2 star formation starts from gas with characteristically low [Mg/Fe] and very high [Al/Fe]. This is a regime found in very few Galactic GCs (see Fig. 8 of Schiavon et al., 2024). It may be reasonable to assume that such extreme abundance patterns are the result of star formation in GCs that are under the effect of a strong interaction with the galaxy host they are spiralling into. Perhaps GCs who never become nuclear clusters never manage to enrich the intracluster gas to such extreme abundance levels. If that is the case, one would conclude that the abundance patterns of 2G stars in GCs (our P2 population) constitute an upper limit on the abundance ratios attained by 2G stars in normal GCs. If that is correct, our results may place important constraints on the source of Al-enrichment/Mg-depletion in GCs. Moreover, if the run of Al with metallicity seen in Figs. 3.2 and 3.3 can be explained on theoretical grounds, one would be

able to explain why multiple populations in metal-rich GCs do not attain a wide range of Al abundances (e.g., Schiavon et al., 2017b; Nataf et al., 2019; Schiavon et al., 2024).

3.6 Summary

We have selected and examined the stellar distributions on canonical chemical planes of the multiple populations hosted by ω Centauri using the APOGEE Value-added Catalogue of Galactic globular clusters (Schiavon et al., 2024). In doing so, we have placed constraints on the assembly history of this complex stellar system. Furthermore, in our cross-match with oMEGACat and construction of the ChM we are able to tie our interpretations into the wider observational state of play. Our main results can be summarised as follows.

1. Application of standard k-means substructure finding to the abundances of Fe, Mg, Si, Al, and Mn, leads to the identification of three distinct populations in ω Cen. The so-called P1 and P2 populations display a broad distribution of metallicities and strong correlations between abundance ratios of Mg, Si, Al, and N and metallicity. The so-called IM population has a narrower range of metallicities, is metal-poor, and displays the abundance anti-correlations commonly present in GCs.

2. P1's chemical compositions are characteristic of dwarf galaxies and the stellar halo at the same [Fe/H]. Starting at [Fe/H]≈ -1.8, [Al/Fe] and [α/Fe] show an increasing trend with respect to [Fe/H], with the latter showing no decline characteristic of the α knee.

3. P2's chemical compositions are characteristic of the most extreme populations seen in Galactic globular clusters. It has significant Al-enhancement (reaching [Al/Fe]$\approx$ 1.2); Si-enhancement (as high as [Si/Fe]$\approx$ 0.4), and significant Mg-depletion (as low as [Mg/Fe]≈ -0.4). Its abundance patterns are characterised by increasing [Mg/Fe], declining [Al/Mg], and constant [Si/Fe] as a function of [Fe/H].

4. We hypothesize that the IM population, with its narrow metallicity spread, and abundance anticorrelations (at fixed [Fe/H]) is the result of the spiralling in of

at least one metal-poor globular cluster towards the centre of the host galaxy of ω Cen.

5. By assuming that the P1 and P2 populations evolve in chemical detachment, we run models of galactic chemical evolution using the `VICE` package to match the behaviour of these populations in the Mg-Fe chemical plane. The best fitting models for both populations consist of a history of star formation characterised by a starburst preceded by a few to several years of low level star formation. The models are a good match to the data on the Mg-Fe plane.

6. Knowing that ω Cen has lost a large amount of stellar mass in its past, we run a `VICE` optimisation that ignores the MDFs of both P1 and P2. The resulting predicted MDFs contain far more power in the metal-rich end than observed. This "metal-rich mass budget problem" can be explained by loss of stars and/or gas on the high metallicity end, predominantly by the P2 population.

7. We suggest that the P1 population was formed first, as a result of chemical evolution from primordial populations in the centre of ω Cen's host galaxy. P2 may form from gas enriched to extreme 2G chemical composition levels within the GC(s) that became the IM population. We speculate that, through this process, extreme 2G abundance patterns such as those seen in P2 are a feature exclusive of nuclear star clusters.

8. The ratio of hydrostatic to explosive α-elements in P2 is much lower than that in P1 and IM. This may be due to P2 having had a top-light IMF.

9. Matching the APOGEE/VAC sample to photometry from the oMEGACat survey, we mapped the loci of the three populations on the so-called chromosome map (ChM) for ω Cen. We find that the P1, P2, and IM populations span the entirety of the area covered by ω Cen stars in the ChM. This exercise demonstrates that the complexity of the distribution of ω Cen stars in the ChM is accounted for by the range of light-element abundances covered by the P1, P2, and IM populations, as well as the chemical evolution of P1 and P2.

10. Finally, we run a robust comparison of the detailed chemical composition of the P1 population with those of halo field substructures Sausage/Gaia-Enceladus, Sequoia, Heracles, and Aurora. The data suggest no chemical association between ω Cen and any of those substructures.

Chapter 4

Summary, Conclusions, and Future Work

Once, the future was only a continuation of the present. All its changes loomed somewhere beyond the horizon. But now the future's a part of the present.

The Writer, *Stalker*

We posed three main questions at the end of **Chapter 1**:

1. What can the abundance patterns of galaxies forming in a simulated cosmological volume tell us about the present-day configuration of the Local Group's galaxies in canonical chemical abundance planes?
2. What are the physics responsible for the formation of the α-knee? Is it merely the 'onset' of SN Ia contributing Fe to the star-forming gas reservoir?
3. Is there a scaling relationship between the metallicity of the α-knee, and if so what drives the scatter in that relationship?
4. What do the abundance patterns of the complex stellar system ω Centauri tell us about its complex assembly history?

In this section, we briefly summarise the contents of each chapter, and how we have answered these questions.

4.1 Concerning the α-abundance patterns in galaxies

Using the EAGLE simulations, in Chapter 2, we presented novel results concerning the α-abundances of galaxies in the Local Group. EAGLE suggests that the α-knee seen in some galaxies in the Local Group only forms in galaxies that experience a decline in their star formation rates, after a peak at some cosmic time. This follows from a variable gas consumption timescale in these systems, whereby it evolves from an initially long value to a short one due to the fact that metals are mixed into a considerably larger gas reservoir that is not uniformly star-forming than implied by the standard assumptions of one-zone GCE models in the simulations.

The SFH characteristic of classical knees means that Fe-enrichment by SN Ia can only dominate that by SN II during the decline due to the prompt decrease in enrichment by SN II. This decrease is not matched by SN Ia as they are still contributing from antecedent stellar populations that have formed. This is not consistent with the way the gas consumption timescale is typically treated in analytical models of galaxy chemical

evolution, where it usually takes a constant value considered reasonable for the stellar mass of the system being modelled, which we demonstrated by running a GCE model that invoked such a variable t_g.

We also constrained the scaling relation between $M_\star$ and $[\mathrm{Fe/H}]_{\mathrm{knee}}$ in the simulations, finding that the slope and scatter are consistent with what has been observed thus far on the basis of chemical abundances of galaxies in the Local Group. This relation is also characterised by significant intrinsic scatter at fixed $M_\star$, which can be understood in terms of the amount of stellar mass that forms during the assembly of the high-α plateau population in these galaxies, before the decline in the SFR. Galaxies with more massive plateaus at fixed total $M_\star$ tend to have higher $[\mathrm{Fe/H}]_{\mathrm{knee}}$. Furthermore, we find that the simulations exhibit a diversity of possible distributions on the α-Fe plane, in addition to knees which we dub 'classical knees'. 'Single slope' galaxies exhibit linearly declining [α/Fe] as a function of [Fe/H], which can be understood in terms of their histories of approximately constant star formation rates as a function of cosmic time, with no steep decline. 'Inverted knees' are characterised by a 'rise' in [α/Fe] at some characteristic [Fe/H], identical to what has been predicted by GCE modelling (Gilmore & Wyse, 1991a; Weinberg et al., 2017a) and observed in some of the Local Group dwarfs (Hasselquist et al., 2017; Nidever et al., 2020a; Hasselquist et al., 2021b) due to the effects of starbursts on the contribution by SN II to the enrichment of the interstellar medium.

The above results have significant implications for our interpretations of the observed α-abundance patterns of galaxies in the Local Group; primarily, those of the high-α disk of the Galaxy. The EAGLE chemodynamical model, as well as one-zone GCE models, show that a high-α plateau can form in spite of a significant contribution to its chemical enrichment by SN Ia, over much longer timescales than assumed in typical treatments for the delay time distribution of SN Ias.

4.2 Concerning the abundance patterns of ω Centauri and its complex assembly history

In Chapter 3, we analysed the chemical abundance patterns of the Galactic stellar cluster ω Cen, a member of the Milky Way globular cluster system suspected to be the nucleated remnant (i.e. nuclear star cluster) of a dwarf galaxy that underwent a merger with the Galaxy during an earlier cosmic epoch. We used data from the APOGEE (Majewski

et al., 2017b) value added catalogue (VAC) of Galactic globular cluster stars (Schiavon et al., 2024). Using clustering analysis, we identify three populations in the cluster based on their chemical abundance patterns which we labelled 'P1', 'P2', and 'IM' according to the standard nomenclature from literature discussing multiple populations in globular clusters. P1 and P2 are characterised by broad spreads in metallicity, and correlations between light-element abundance patterns and metallicity consistent with the stellar halo at the same metallicity, and 'extreme' P2 stars in other GCs, respectively. Conversely, the IM population exhibits a narrow metallicity spread, and the 'standard' anomalous abundance patterns associated with the multiple populations phenomenon.

We further supplemented our data by performing a cross-match between the VAC and a recently-published catalogue of MUSE spectroscopy and HST-derived photometry (oMEGACat; Nitschai et al., 2023; Häberle et al., 2024). This enabled us to directly map the metallicities and light-element abundance patterns of stars in ω Cen to their positions in the cluster's CMD and chromosome map. Using a combination of GCE modelling, and analysis of the positions of stars on a combination of canonical chemical planes and the chromosome map, we are able to infer that both P1 and P2 have had bursty star formation histories. We also demonstrate that P2's abundance patterns are consistent with its stars having formed from gas whose abundances were set by the polluters responsible for 'extreme' GC abundances. The subsequent episodes of star formation that took place did so with a combination of SN II, SN Ia and AGB stars contributing to the chemical enrichment. Using treatments for the star formation efficiency consistent with prior work, the GCE model struggles to reproduce the MDF, particularly of the P2 stars. This could indicate that a significant amount of the star-forming gas, or stars, of the P2 population were stripped from the cluster due to its interactions with the Milky Way.

The IM population exhibits the standard light-element abundance anticorrelations seen in most Galactic GCs, and its narrow spread in metallicity may indicate that it represents a stellar population that formed in ω Cen's assembly by the inspiralling of at least one of its host's GCs, consistent with current scenarios regarding the assembly of nuclear star clusters in dSph galaxies. If these clusters were gas-rich, the P2 population could have formed from this gas with the 'extreme' abundance pattern. Furthermore, we find that the 'extreme' abundance pattern that P2's stars exhibit is seen in very few globular clusters. Comparisons with the abundances of other GCs in the VAC suggest that the extremely high Si and Al enrichment of P2 represents an upper envelope in this chemical plane, with only a handful of other Galactic GCs hosting similar stars.

Our interpretation of the chemical abundance patterns of the cluster imply that the P1 stars represent, at low metallicity, the field stars of the galaxy ω Cen was the NSC of. We perform a statistical comparison between the abundances of P1 and stars comprising other substructures identified using data from *Gaia* and APOGEE. We find a similarity between ω Cen and the stars comprising the Heracles population identified in Horta et al. (2021a), an accreted population identified in the inner ($R < 4kpc$) regions of the Galaxy. However, at higher metallicities there are no literature substructures whose abundance patterns are consistent with P1.

4.3 Future work

I first start by discussing more immediate avenues of follow-up research from Chapters 2 and 3. Then, I discuss upcoming observational and simulated data releases, and their relevance to obvious opportunities for follow-up studies concerning my research. As I briefly alluded to in the introduction, the remit of Galactic archaeology is now well and truly expanding to encompass the entire Local Group. In tandem, advancements in the capability of cosmological simulations to both resolve physical processes down to small distance and temperature scales and to produce large volumes are generating complementary datasets to place the assembly of the Local Group in its proper cosmological context. There are myriad ways to leverage such data, which I shall discuss now in order of what I consider to be the most interesting prospects.

4.3.1 The detailed metal accumulation histories of EAGLE galaxies

Fig. 2.5 shows convincingly that the distribution of stellar particles in EAGLE galaxies on the α-Fe plane depends on the SFR. A promising follow-up for this work would be the explicit measurement of the history of metal mass loss from single slope and classical knee galaxies, especially given the consideration that the simulations explicitly track the mass of metals split into their contribution by SN II, SN Ia, and AGB stars. Cosmic evolution of metal mass loss rates is to be expected, given that at high z the potential wells of galaxies will not be as deep as at $z = 0$ due to the fact that they have not fully assembled yet. At early cosmic times, the mass loss of metals from both SN II and SN Ia should be comparable. There is a characteristic temperature at which SN II and SN Ia inject their metals into the ISM that is characteristically higher for SN II. Because

SN Ia release their metals at a lower temperature, they are more likely to be retained by a given galaxy. A more fundamental connection between the formation of α-knees and the distribution of stellar particles on the α-Fe plane could be made with the properties of the host haloes of galaxies by studying the preferential loss of metals depending on their source in the simulations.

The preferential ejection of metals from these SN species lends itself to an easy follow-up using the sample of galaxies analysed in Chapter 2. We can directly measure the metal accumulation history by computing the total amount of O (since it has no contribution from SN Ia), Fe from SN Ia, and Fe from SN II in star particles across the snapshots. In addition, we can measure the same but for a combination of gas and star particles. This will give us a direct measurement on the metal mass loading of outflows, as well as whether or not the outflows are preferentially loaded with ejecta from SN II, SN Ia, or both.

4.3.1.1 The effects of subgrid physics variations on the picture of knee formation

The EAGLE simulations were calibrated to broadly reproduce a set of observables seen in the $z = 0.1$ galaxy population, as described in Chapter 2 and Crain et al. (2015). Mackereth et al. (2018a) explored the effects of varying the parameters of the adopted exponential SN Ia DTD on their scenario for the formation of the α-bimodality in MW-massed disk galaxies in the flagship L100N1504 volume. The same experiment, varying the parameters ν (the number of SN Ias per unit stellar mass), $\tau_{\rm Ia}$ (the e-folding timescale), *and* $t_{\rm d,\ min}$ would be an important check regarding how generic knee formation is in EAGLE, rather than model-dependent.

4.3.2 Dwarf galaxies and knee formation in the current *and* next generation of cosmological numerical simulations

In their review, Crain & van de Voort (2023) demonstrated that markedly different implementations of subgrid physics can produce degenerate outcomes as far as the resemblance of simulated galaxies to the 'real' galaxy population goes. An interesting exercise, as a follow-up to Mason et al. (2023), would be to investigate the formation of α-knees in *other* suites of cosmological SPH simulations, for instance IllustrisTNG (Nelson et al., 2018; Pillepich et al., 2018; Springel et al., 2018). Alternatively, we

could resort to using zoom-in simulations (e.g. ARTEMIS or AURIGA Font et al., 2020; Grand et al., 2017). These are re-simulations of the haloes of Milky Way-analogues from collisionless (dark matter only) volumes at higher resolution. With a sufficient number of volumes to offer an opportunity to study lower-massed simulated dwarf satellites, it would be interesting to study the chemical evolution of these systems. Repeating the analyses described here in zooms has the advantage expanding the range of stellar masses that we can constrain the MKR for.

On a related note, the results we presented concerning the formation of α-knees were necessarily restricted to well-sampled ($M_\star > 10^{8.5}$ M$_\odot$) galaxies. Simulators are gradually pushing the envelope as far as resolution and baryon physics are concerned, and the field finds itself anticipating the release of several high-profile cosmological simulations. The chemical abundance data presented in Chapter 1 mainly comprised measurements in the satellites of the Milky Way, which span from dIrr to dSph galaxies. The analysis in 2 was conducted on a sample of galaxies from the EAGLE simulations that comprise only the former, through to galaxies with stellar masses above $M^\star$. As presented in Schaye et al. (2015), the EAGLE GSMF only agrees with that measured through observations down to $M_\star = 10^8$M$_\odot$. Simulations of sufficient resolution to produce realistic dwarf galaxies below this mass, with prescriptions of relevant physical processes thought to significantly influence their evolution more so than more massive systems, will surely produce a watershed moment for this field. The successor to EAGLE is on the horizon and adopt a more sophisticated chemodynamical model. It will be crucial to test our scenario for knee formation when these data become available, even in the same range of stellar masses, to see if our predictions are generic for a completely different treatment of the ISM.

4.3.3 The formation of ω Centauri - insights from cosmological hydrodynamical simulations

Recent cosmological simulations have included treatments for the formation of globular clusters as subgrid prescriptions, such as E-MOSAICS (Pfeffer et al., 2018; Bastian et al., 2020; Kruijssen et al., 2019a), which incorporates the semi-analytic MOSAICS Kruijssen et al. (2012) model. These simulations are useful for explaining the properties of the globular cluster systems of galaxies, but offer little insight into the chemical enrichment of individual populations within these clusters.

However, the EDGE simulations (Rey et al., 2019; Agertz et al., 2020; Rey et al., 2020; Pontzen et al., 2021; Orkney et al., 2021; Rey et al., 2022; Prgomet et al., 2022; Orkney et al., 2023; Goater et al., 2024; Rey et al., 2024) have presented novel results regarding the formation of globular and nuclear star clusters in ultra-faint ($10^3 < M_\star < 10^5\ M_\odot$) dwarfs (Orkney et al., 2022). The EDGE project has produced cosmological zoom-in simulations of these galaxies, modelled using the adaptive mesh refinement code RAMSES. Fascinatingly, Gray et al. (2024) studied the formation of nuclear star clusters in these galaxies at a gas and dark matter mass resolution of $M_g \simeq 161\ M_\odot$ and $M_{DM} \simeq 945\ M_\odot$, respectively. In a subset of dwarf galaxies with $M_{DM} \simeq 5 \times 10^9\ M_\odot$, they found that populations characterised by markedly different O-abundances emerge naturally. Prior to the epoch of reionisation, these systems are formed in a burst of star formation that forms the first generation of stars, characterised by significant α-enhancement as a function of [Fe/H]. Star formation is quenched by reionisation without loss of the star-forming gas reservoir. Subsequently, their host dwarfs undergo a major merger which excites gas cooling in the cluster, leading to another burst of star formation that consumes the gas reservoir and quenches star formation.

This is an entirely novel scenario, and the authors suggest observations that may lend it credence. While it is unlikely that ω Centauri originates from a UFD, the EDGE project aims to produce iterations of the simulations that modelling successively higher-massed systems. In the meantime, a study of ω Cen's kinematics is motivated - since we have chemically tagged populations that should correspond roughly to the pre and post-reionisation populations seen in Gray et al. (2024), we can test whether P2 is kinematically colder and more metal-rich than the P1 stars.

4.3.4 The evolution and assembly of the Local Group as probed by chemical abundances from upcoming spectroscopic surveys

As we discussed at length in Chapter 1, most spectroscopic observations of the Local Group dwarfs have been made by allocation of telescope time to research groups. APOGEE (Majewski et al., 2017a; Abdurro'uf et al., 2022) also targeted a number of fields in these galaxies, and thus we collectively have a sample of stars with measured chemical abundances in the LGDs that numbers of the order of 10^4.

A number of high profile stellar surveys are scheduled to make public data releases within the next decade, such as WEAVE (Jin et al., 2023), 4MOST (de Jong et al., 2019), and

MOONS (Cirasuolo et al., 2011; Gonzalez et al., 2020). The LGD component of 4MOST (4DWARFS; Skúladóttir et al., 2023) aims to raise the sample of stars in the LGDs with spectroscopic abundances measured by over an order of magnitude. With access to these data, I would pursue two lines of inquiry:

1. In Chapter 2, we showed the current observational MKR. With a larger sample of stellar abundances for the dwarfs comprising the Local Group, it could become feasible to greatly expand the sampling of this scaling relation and get a better handle of its scatter at fixed $M_\star$. 4DWARFS alone will be targetting stars in $\simeq$ 50 of the LGDs. Furthermore, the run of [α/Fe] as a function of [Fe/H] as well as other abundances will place invaluable constraints on their histories of star formation. It is well established that at fixed $M_\star$ dwarf galaxies can exhibit substantially different histories of star formation. In this regime of stellar masses, it will be interesting to see how impactful the star formation histories of these systems are on their detailed abundance patterns given their implicit inability to easily retain ejecta from SN Ia and SN II explosions.

2. In Chapter 3, we speculated that over the course of its interactions with the Milky Way ω Cen may have experienced significant stellar mass loss in its P2 stars. A sweeping search of these data for stars with P2-like abundances (i.e. the 'extreme' GC abundance pattern) would prove invaluable in estimating the total mass lost to the Milky Way from this population as a function of Galactocentric radius.

This thesis has presented novel results concerning the interpretation of so-called 'canonical' chemical abundance planes, which will greatly benefit from the upcoming deluge of chemical abundance data and the release of several high-profile simulations of galaxy formation and evolution. Understanding the assembly histories that lead to the abundance patterns that we observe in the Local Group will be crucial for our understanding of the formation of galaxies, across the GSMF.

Appendix A

Constructing the oMEGACat chromosome map

In Chapter 3, we discussed the behaviour of chemically tagged stars belonging to the multiple populations of ω Centauri from the APOGEE VAC of Galactic globular cluster stars. In this appendix, we present the full details of the procedure used to derive the chromosome map from the oMEGACat catalogues, described in Milone et al. (2017a) and Nitschai et al. (2024).

Fig. A.1 shows the CMD of ω Cen, represented by a 2d histogram of m_{F814W} as a function of the color $C_{\mathrm{F275W,\,F814W}}$. In mag bins in x and y, each pixel is coloured by the median oMEGACat [M/H] in that bin. Also shown are the fiducial lines for the metal-poor (MP; blue and red) population, the running median fiducial line for the intermediate (IM; green) population, and the running median fiducial line for the metal-rich (MR; orange) population.

We have already described how the fiducial lines on the $m_{\mathrm{F814W}} - c_{\mathrm{F275W,\,F814W}}$ and $m_{\mathrm{F814W}} - C_{\mathrm{F275W,\,F336W,\,F435W}}$ CMDs were derived. For the former, we compute the following weights:

$$W_{\mathrm{F275W,\,F814W_1}} = X_{\mathrm{fiducialRed}}(15.5\ \mathrm{mag}) - X_{\mathrm{fiducialBlue}}(15.5\ \mathrm{mag}), \tag{A.1}$$

$$W_{\mathrm{F275W,\,F814W_2}} = X_{\mathrm{fiducialOrange}}(15.5\ \mathrm{mag}) - X_{\mathrm{fiducialRed}}(15.5\ \mathrm{mag}), \tag{A.2}$$

$$W_{\mathrm{F275W,\,F814W_3}} = X_{\mathrm{fiducialGreen}}(15.5\ \mathrm{mag}) - X_{\mathrm{fiducialOrange}}(15.5\ \mathrm{mag}), \tag{A.3}$$

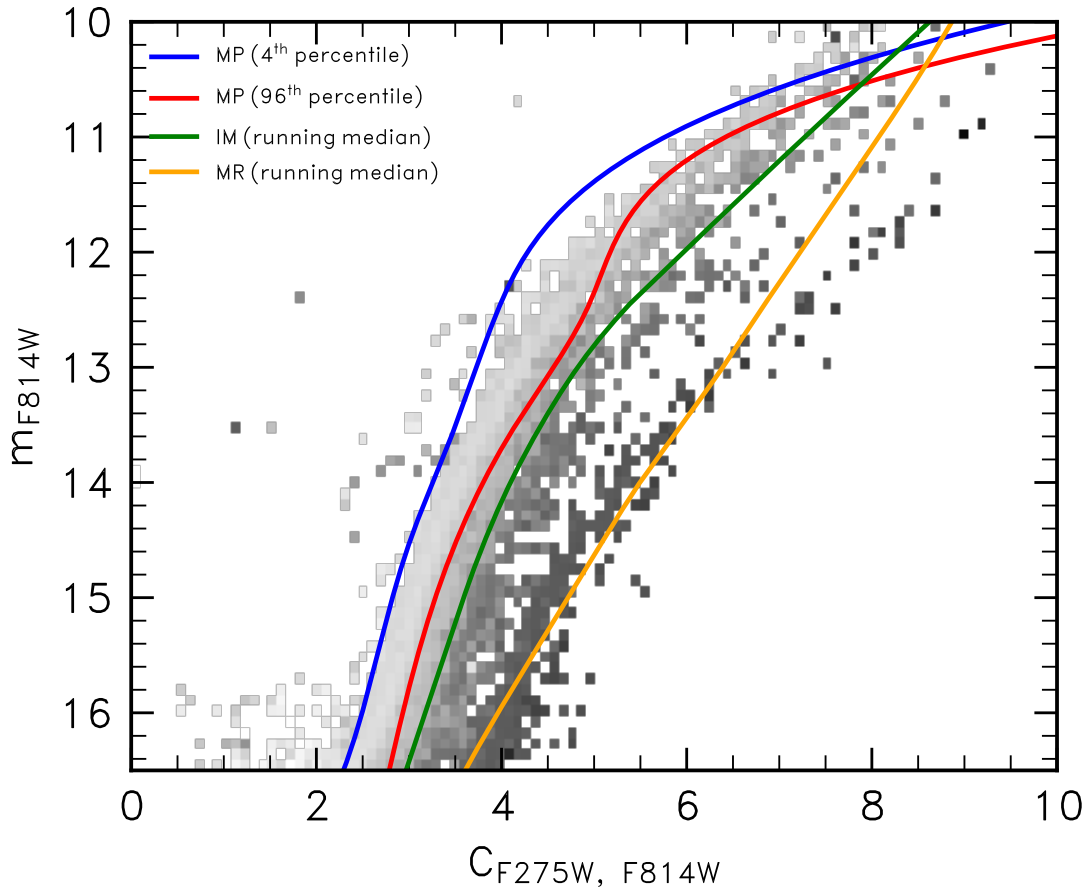

Figure A.1: CMD represented by the pseudocolor $C_{\mathrm{F275W,\ F814W}}$ plotted as a function of m_{F814W} for the MUSE-QC/HST-QC samples from Nitschai et al. (2023) and Häberle et al. (2024). Blue, red, green, and orange lines indicate fiducial lines representing the 4$^{\mathrm{th}}$ percentile values of the metal-poor stars, the 96$^{\mathrm{th}}$ percentile values of the metal-poor stars, the running median of the intermediate stars, and the running median of the metal-rich stars, respectively.

where $X_{fiducial}(15.5\ \mathrm{mag})$ denotes the colour of a given fiducial line at $m_{\mathrm{F814W}} = 15.5$. Using these weights, the $\Delta_{\mathrm{F275W,\ F814W}}$ can be computed as follows:

$$\Delta_{\mathrm{F275W,\ F814W_1}} = W_{\mathrm{F275W,\ F814W_1}} \frac{X - X_{\mathrm{fiducialRed}}}{X_{\mathrm{fiducialRed}} - X_{\mathrm{fiducialBlue}}}, \tag{A.4}$$

$$\Delta_{\mathrm{F275W,\ F814W_2}} = W_{\mathrm{F275W,\ F814W_2}} + W_{\mathrm{F275W,\ F814W_2}} \frac{X - X_{\mathrm{fiducialOrange}}}{X_{\mathrm{fiducialOrange}} - X_{\mathrm{fiducialRed}}}, \tag{A.5}$$

$$\Delta_{\mathrm{F275W,\ F814W_3}} = W_{\mathrm{F275W,\ F814W_2}} + W_{\mathrm{F275W,\ F814W_3}} + W_{\mathrm{F275W,\ F814W_3}} \frac{X - X_{\mathrm{fiducialGreen}}}{X_{\mathrm{fiducialGreen}} - X_{\mathrm{fiducialOrange}}}, \tag{A.6}$$

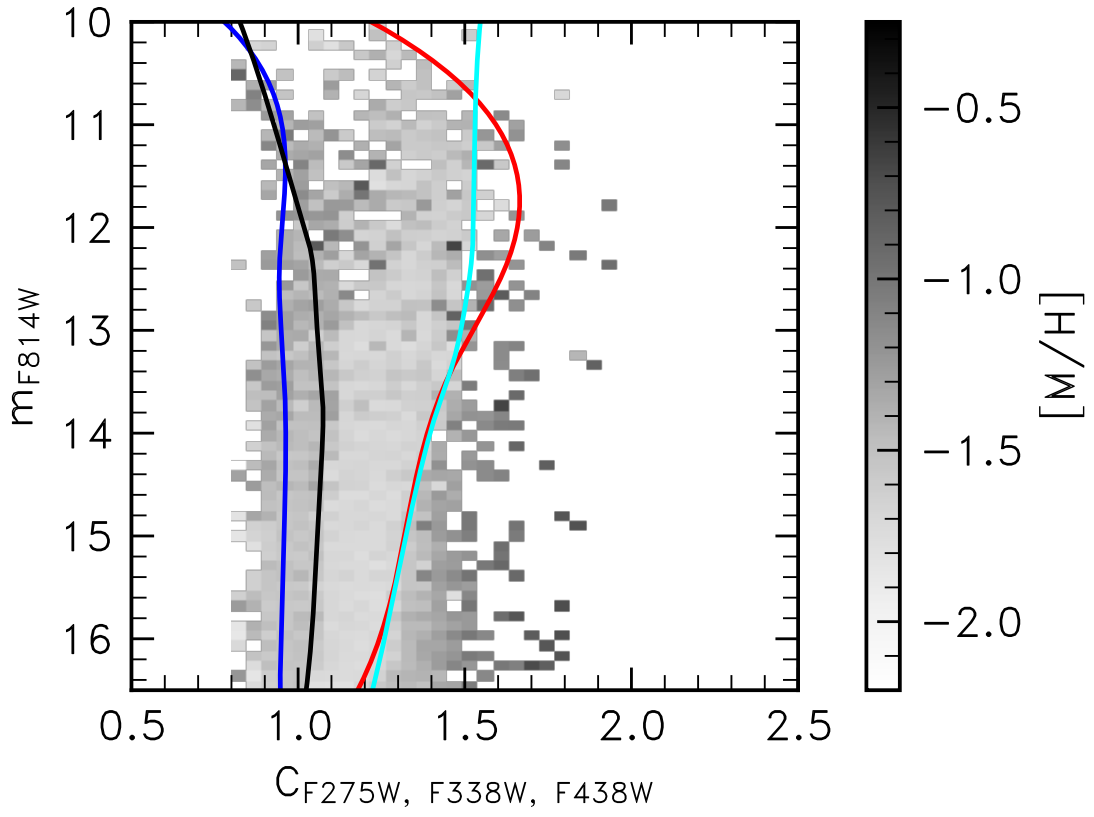

Figure A.2: CMD represented by the pseudocolor $C_{\mathrm{F275W,\ F338W,\ F435W}}$ plotted as a function of m_{F814W} for the MUSE-QC/HST-QC samples from Nitschai et al. (2023) and Häberle et al. (2024). Blue and red lines indicate fiducial lines for the 4$^{\mathrm{th}}$ and 96$^{\mathrm{th}}$ percentile values for a combination of the metal-poor and intermediate stars, respectively. Black and cyan represent the same kinds of fiducial lines, for the metal-rich stars only.

where X is the colour at a given m_{F814W}, and X_{fiducial} values are the interpolated values for each fiducial line at that magnitude.

Fig. A.2 shows the CMD of ω Cen, represented by a 2d histogram of m_{F814W} as a function of the color $C_{\mathrm{F275W,\ F336W,\ F435W}}$. In mag bins in x and y, each pixel is coloured by the median oMEGACat [M/H] in that bin. Also shown are the fiducial lines for the metal-poor (MP; blue and red) population, the running median fiducial line for the intermediate (IM; green) population, and the running median fiducial line for the metal-rich (MR; orange) population.

In the case of the $C_{\mathrm{F275W,\ F336W,\ F435W}}$-$m_{\mathrm{F814W}}$ CMD, the weights are as follows:

$$W_{\mathrm{F275W,\ F336W,\ F435W_1}} = X_{\mathrm{fiducialRed}}(15.5\ \mathrm{mag}) - X_{\mathrm{fiducialBlue}}(15.5\ \mathrm{mag}), \quad \text{(A.7)}$$

$$W_{\mathrm{F275W,\ F336W,\ F435W_2}} = X_{\mathrm{fiducialRed}}(15.5\ \mathrm{mag}) - X_{\mathrm{fiducialCyan}}(15.5\ \mathrm{mag}), \quad \text{(A.8)}$$

$$W_{\mathrm{F275W,\ F336W,\ F435W_3}} = X_{\mathrm{fiducialCyan}}(15.5\ \mathrm{mag}) - X_{\mathrm{fiducialBlack}}(15.5\ \mathrm{mag}), \tag{A.9}$$

$$\Delta_{\mathrm{F275W,\ F336W,\ F435W_1}} = W_{\mathrm{F275W,\ F336W,\ F435W_1}} \frac{Y_{\mathrm{fiducialRed}} - Y}{Y_{\mathrm{fiducialRed}} - X_{\mathrm{fiducialBlue}}}, \tag{A.10}$$

$$\begin{aligned} \Delta_{\mathrm{F275W,\ F336W,\ F435W_2}} &= W_{\mathrm{F275W,\ F336W,\ F435W_2}} \\ &+ W_{\mathrm{F275W,\ F336W,\ F435W_3}} \frac{Y_{\mathrm{fiducialCyan}} - Y}{Y_{\mathrm{fiducialCyan}} - X_{\mathrm{fiducialBlack}}}, \end{aligned} \tag{A.11}$$

Appendix B

Corner plots for GCE modelling of P1 and P2 stars

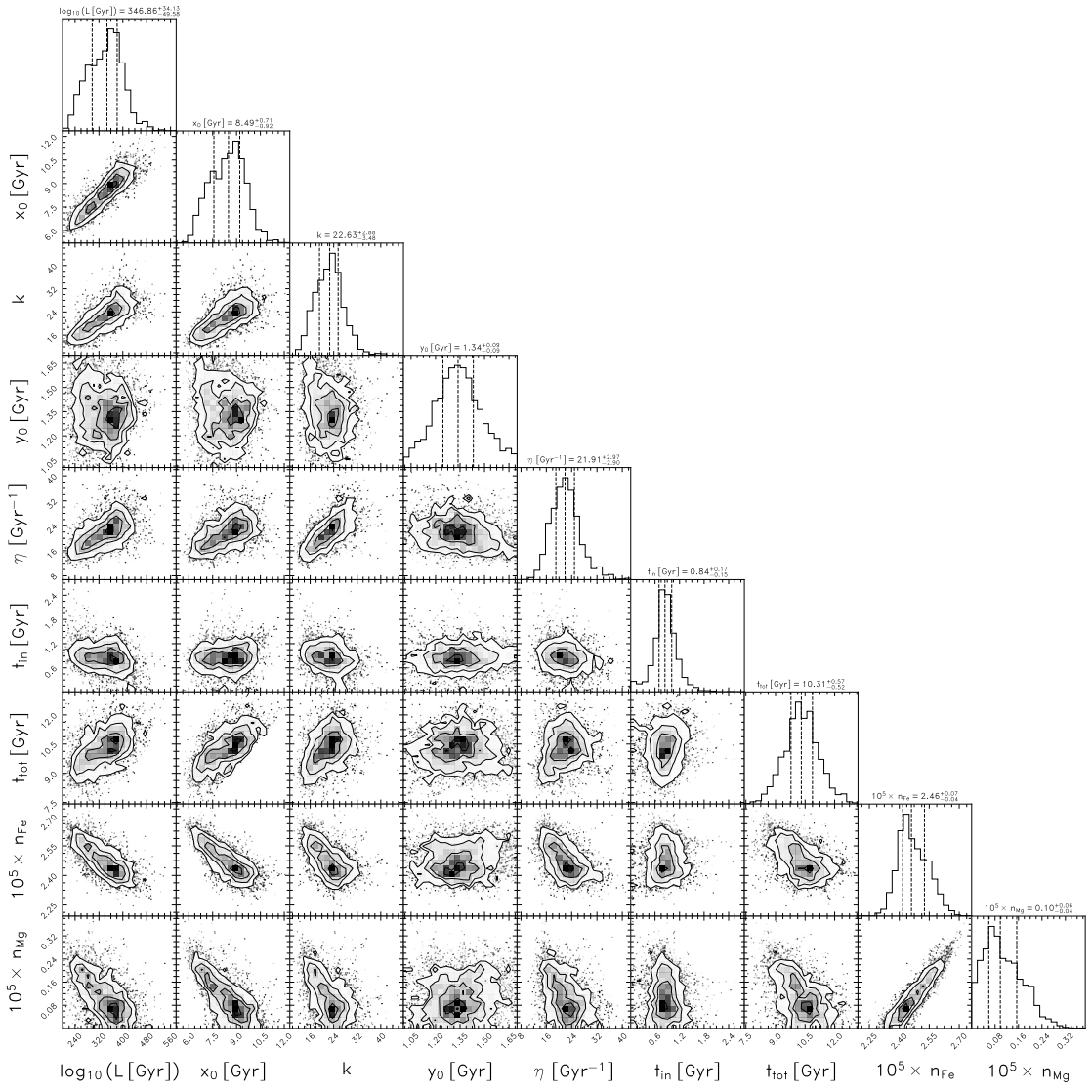

Figure B.1: A corner plot showing the posterior probability distributions for each parameter, given the constraints of the prescriptions for P1 described in §3.4. The model favours a star formation history characterised by initially *very* inefficient star formation ($t_{\rm g}$ = 617) Gyr with strong outflows (η = 60 Gyr^{-1}) as well as a gas inflow history that peaks at very early times ($t_{\rm in}$ = 0.4 Gyr). Subsequently, there is a burst of star formation whereby t_g drops precipitously to $t_{\rm g}$ = 1.25 Gyr.

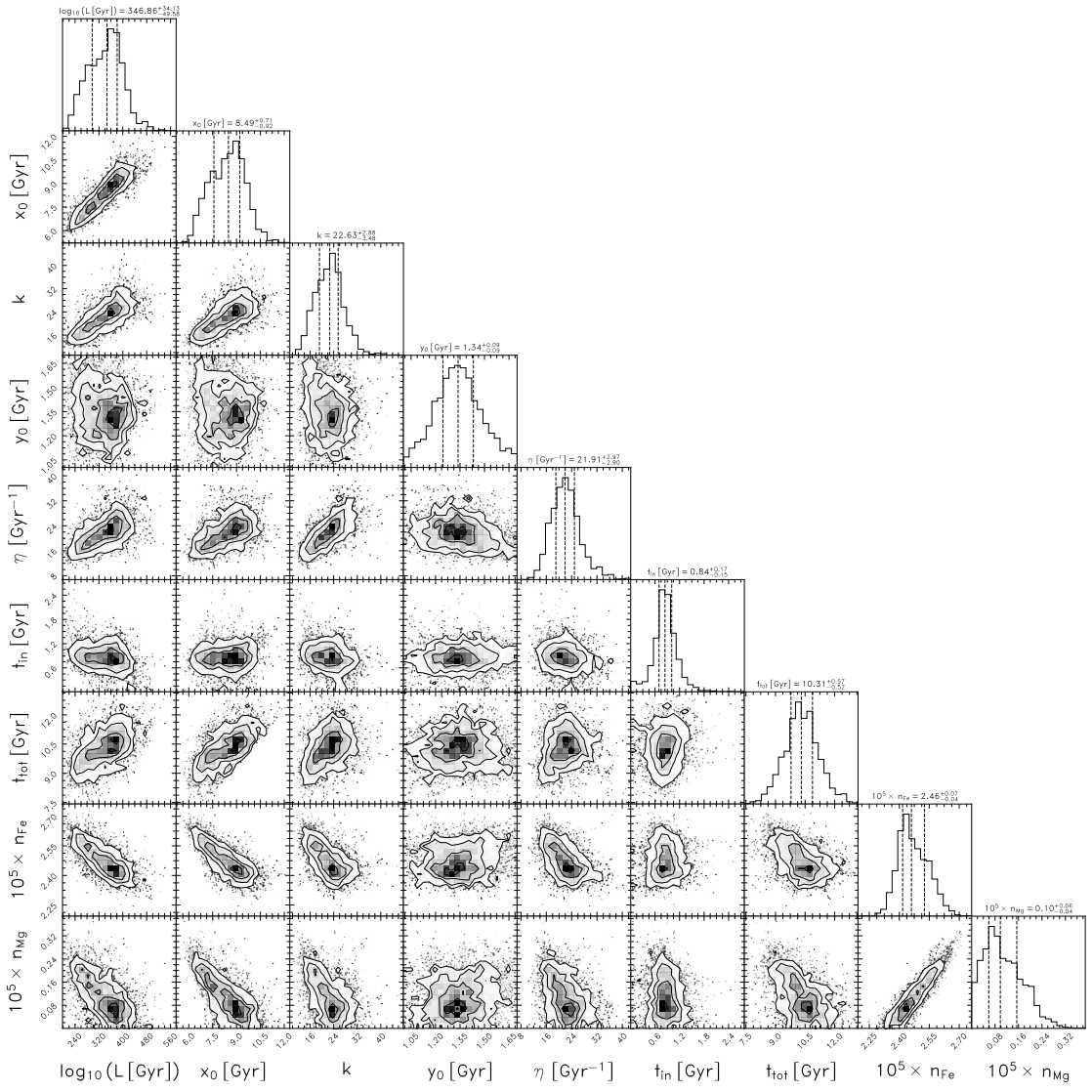

Figure B.2: A corner plot showing the posterior probability distributions for each parameter, given the constraints of the prescriptions for P2 described in §3.4. The model favours a star formation history characterised by initially inefficient star formation ($t_{\rm g}$ = 347) Gyr with strong outflows (η = 22 Gyr^{-1}) as well as a gas inflow history that peaks at very early times ($t_{\rm in}$ = 0.84 Gyr). Subsequently, there is a burst of star formation whereby t_g drops precipitously to $t_{\rm g}$ = 1.34 Gyr at t = 8.49 [Gyr].

Bibliography

Abdurro'uf et al., 2022, ApJS, 259, 35

Agertz O., et al., 2020, Monthly Notices of the Royal Astronomical Society, 491, 1656

Ahn C. P., et al., 2012, ApJS, 203, 21

Alvarez Garay D. A., Mucciarelli A., Bellazzini M., Lardo C., Ventura P., 2024, Astronomy & Astrophysics, 681, A54

Andrews B. H., Weinberg D. H., Schönrich R., Johnson J. A., 2017, The Astrophysical Journal, 835, 224

Arnould M., Goriely S., Jorissen A., 1999, Astronomy & Astrophysics, 347, 572

Asplund M., Grevesse N., Sauval A. J., Scott P., 2009, ARA&A, 47, 481

Bacon R., et al., 2010, in McLean I. S., Ramsay S. K., Takami H., eds, Society of Photo-Optical Instrumentation Engineers (SPIE) Conference Series Vol. 7735, Ground-based and Airborne Instrumentation for Astronomy III. p. 773508 (arXiv:2211.16795), doi:10.1117/12.856027

Bacon R., et al., 2014, The Messenger, 157, 13

Baldry I. K., Glazebrook K., Driver S. P., 2008, Monthly Notices of the Royal Astronomical Society, 388, 945

Baldry I. K., et al., 2012, Monthly Notices of the Royal Astronomical Society, 421, 621

Barbá R. H., Minniti D., Geisler D., Alonso-García J., Hempel M., Monachesi A., Arias J. I., Gómez F. A., 2019, ApJ, 870, L24

Bassino L. P., Muzzio J. C., Rabolli M., 1994, The Astrophysical Journal, 431, 634

Bastian N., Lardo C., 2018, ARA&A, 56, 83

Bastian N., Covey K. R., Meyer M. R., 2010, ARA&A, 48, 339

Bastian N., Pfeffer J., Kruijssen J. M. D., Crain R. A., Trujillo-Gomez S., Reina-Campos M., 2020, Monthly Notices of the Royal Astronomical Society, 498, 1050

Baumgardt H., Hilker M., 2018, Monthly Notices of the Royal Astronomical Society, 478, 1520

Bechtol K., et al., 2015, The Astrophysical Journal, 807, 50

Bekki K., Freeman K. C., 2003, Monthly Notices of the Royal Astronomical Society, 346, L11

Bellazzini M., et al., 2008, AJ, 136, 1147

Bellini A., Bedin L. R., Piotto G., Milone A. P., Marino A. F., Villanova S., 2010, AJ, 140, 631

Belokurov V., Kravtsov A., 2022, Monthly Notices of the Royal Astronomical Society, 514, 689

Belokurov V., Kravtsov A., 2023a, Monthly Notices of the Royal Astronomical Society, 525, 4456

Belokurov V., Kravtsov A., 2023b, Monthly Notices of the Royal Astronomical Society, 525, 4456

Belokurov V., Erkal D., Evans N. W., Koposov S. E., Deason A. J., 2018a, Monthly Notices of the Royal Astronomical Society, 478, 611

Belokurov V., Erkal D., Evans N. W., Koposov S. E., Deason A. J., 2018b, Monthly Notices of the Royal Astronomical Society, 478, 611

Belokurov V., Sanders J. L., Fattahi A., Smith M. C., Deason A. J., Evans N. W., Grand R. J. J., 2020, Monthly Notices of the Royal Astronomical Society, 494, 3880

Bensby T., Feltzing S., Lundström I., 2003, Astronomy & Astrophysics, 410, 527

Bensby T., Feltzing S., Lundström I., Ilyin I., 2005, Astronomy & Astrophysics, 433, 185

Bensby T., Feltzing S., Oey M. S., 2014, Astronomy & Astrophysics, 562, A71

Bertelli G., Mateo M., Chiosi C., Bressan A., 1992, The Astrophysical Journal, 388, 400

Binney J., Tremaine S., 2008, Galactic Dynamics: Second Edition. Princeton University Press

Bland-Hawthorn J., Gerhard O., 2016, ARA&A, 54, 529

Blanton M. R., et al., 2017, AJ, 154, 28

Boissier S., Prantzos N., 1999, Monthly Notices of the Royal Astronomical Society, 307, 857

Booth C. M., Schaye J., 2009, Monthly Notices of the Royal Astronomical Society, 398, 53

Bothwell M. S., Maiolino R., Kennicutt R., Cresci G., Mannucci F., Marconi A., Cicone C., 2013, Monthly Notices of the Royal Astronomical Society, 433, 1425

Bovy J., 2015, ApJS, 216, 29

Bowen I. S., Vaughan A. H. J., 1973, Appl. Opt., 12, 1430

Bower R. G., Schaye J., Frenk C. S., Theuns T., Schaller M., Crain R. A., McAlpine S., 2017, Monthly Notices of the Royal Astronomical Society, 465, 32

Brodie J. P., Strader J., 2006, ARA&A, 44, 193

Bullock J. S., Boylan-Kolchin M., 2017, ARA&A, 55, 343

Carlin J. L., Sheffield A. A., Cunha K., Smith V. V., 2018, ApJ, 859, L10

Carretta E., D'Orazi V., Gratton R. G., Lucatello S., 2012a, Astronomy & Astrophysics, 543, A117

Carretta E., Bragaglia A., Gratton R. G., Lucatello S., D'Orazi V., 2012b, ApJ, 750, L14

Carrillo A., Deason A. J., Fattahi A., Callingham T. M., Grand R. J. J., 2023, arXiv e-prints, p. arXiv:2306.00770

Cassisi S., Salaris M., 2013, Old Stellar Populations: How to Study the Fossil Record of Galaxy Formation. Wiley

Chabrier G., 2003, PASP, 115, 763

Chen B., Ting Y.-S., Hayden M., 2023a, arXiv e-prints, p. arXiv:2308.15976

Chen B., Ting Y.-S., Hayden M., 2023b, arXiv e-prints, p. arXiv:2308.15976

Chiappini C., Matteucci F., Gratton R., 1997, The Astrophysical Journal, 477, 765

Chieffi A., Limongi M., 2004, The Astrophysical Journal, 608, 405

Chiosi C., 1980, Astronomy & Astrophysics, 83, 206

Chiou Y. S., Naoz S., Burkhart B., Marinacci F., Vogelsberger M., 2019, ApJ, 878, L23

Chiti A., et al., 2022, arXiv e-prints, p. arXiv:2205.01740

Choksi N., Gnedin O. Y., Li H., 2018, Monthly Notices of the Royal Astronomical Society, 480, 2343

Cirasuolo M., Afonso J., Bender R., Bonifacio P., Evans C., Kaper L., Oliva E., Vanzi L., 2011, The Messenger, 145, 11

Cleveland W. S., 1979a, Journal of the American Statistical Association, 74, 829

Cleveland W. S., 1979b, Journal of the American statistical association, 74, 829

Conroy C., Graves G. J., van Dokkum P. G., 2014, The Astrophysical Journal, 780, 33

Conroy C., et al., 2019a, The Astrophysical Journal, 883, 107

Conroy C., et al., 2019b, The Astrophysical Journal, 883, 107

Conroy C., et al., 2022a, arXiv e-prints, p. arXiv:2204.02989

Conroy C., et al., 2022b, arXiv e-prints, p. arXiv:2204.02989

Cowie L. L., Songaila A., Hu E. M., Cohen J. G., 1996, AJ, 112, 839

Crain R. A., van de Voort F., 2023, ARA&A, 61, 473

Crain R. A., et al., 2015, Monthly Notices of the Royal Astronomical Society, 450, 1937

Cullen L., Dehnen W., 2010, Monthly Notices of the Royal Astronomical Society, 408, 669

Curti M., Mannucci F., Cresci G., Maiolino R., 2020, Monthly Notices of the Royal Astronomical Society, 491, 944

Dalcanton J. J., et al., 2012, ApJS, 200, 18

Dalla Vecchia C., Schaye J., 2012, Monthly Notices of the Royal Astronomical Society, 426, 140

Das P., Hawkins K., Jofré P., 2020, Monthly Notices of the Royal Astronomical Society, 493, 5195

Davies J. J., Crain R. A., McCarthy I. G., Oppenheimer B. D., Schaye J., Schaller M., McAlpine S., 2019, Monthly Notices of the Royal Astronomical Society, 485, 3783

Davies J. J., Crain R. A., Oppenheimer B. D., Schaye J., 2020, Monthly Notices of the Royal Astronomical Society, 491, 4462

De Rossi M. E., Bower R. G., Font A. S., Schaye J., Theuns T., 2017, Monthly Notices of the Royal Astronomical Society, 472, 3354

De Silva G. M., et al., 2015, Monthly Notices of the Royal Astronomical Society, 449, 2604

Deason A. J., Belokurov V., 2024, New Astron. Rev., 99, 101706

Deason A. J., Belokurov V., Koposov S. E., Lancaster L., 2018, ApJ, 862, L1

Dehnen W., McLaughlin D. E., Sachania J., 2006, Monthly Notices of the Royal Astronomical Society, 369, 1688

Deng L.-C., et al., 2012, Research in Astronomy and Astrophysics, 12, 735

Dolag K., Borgani S., Schindler S., Diaferio A., Bykov A. M., 2008, Space Sci. Rev., 134, 229

Drlica-Wagner A., et al., 2015, The Astrophysical Journal, 813, 109

Dunkley J., et al., 2009, ApJS, 180, 306

Durier F., Dalla Vecchia C., 2012, Monthly Notices of the Royal Astronomical Society, 419, 465

Edvardsson B., Andersen J., Gustafsson B., Lambert D. L., Nissen P. E., Tomkin J., 1993, Astronomy & Astrophysics, 275, 101

Eggen O. J., Lynden-Bell D., Sandage A. R., 1962, The Astrophysical Journal, 136, 748

Eisenstein D. J., et al., 2011, AJ, 142, 72

Ellison S. L., Patton D. R., Simard L., McConnachie A. W., 2008, ApJ, 672, L107

Elmegreen B. G., Efremov Y. N., 1997, The Astrophysical Journal, 480, 235

Emsellem E., van de Ven G., 2008, The Astrophysical Journal, 674, 653

Fahrion K., et al., 2021, Astronomy & Astrophysics, 650, A137

Fernandes L., et al., 2023a, Monthly Notices of the Royal Astronomical Society, 519, 3611

Fernandes L., et al., 2023b, Monthly Notices of the Royal Astronomical Society, 519, 3611

Fernández-Trincado J. G., Beers T. C., Tang B., Moreno E., Pérez-Villegas A., Ortigoza-Urdaneta M., 2019, Monthly Notices of the Royal Astronomical Society, 488, 2864

Font A. S., et al., 2020, Monthly Notices of the Royal Astronomical Society, 498, 1765

Forbes D. A., Bridges T., 2010, Monthly Notices of the Royal Astronomical Society, 404, 1203

Forbes D. A., et al., 2018, Proceedings of the Royal Society of London Series A, 474, 20170616

Frinchaboy P. M., et al., 2002, in van Leeuwen F., Hughes J. D., Piotto G., eds, Astronomical Society of the Pacific Conference Series Vol. 265, Omega Centauri, A Unique Window into Astrophysics. p. 143 (arXiv:astro-ph/0112169), doi:10.48550/arXiv.astro-ph/0112169

Fuhrmann K., 1998, Astronomy & Astrophysics, 338, 161

Gaia Collaboration et al., 2016, Astronomy & Astrophysics, 595, A1

Gaia Collaboration et al., 2018, Astronomy & Astrophysics, 616, A1

Gaia Collaboration et al., 2021, Astronomy & Astrophysics, 649, A1

Gallart C., et al., 2015, ApJ, 811, L18

Gallazzi A., Charlot S., Brinchmann J., White S. D. M., Tremonti C. A., 2005, Monthly Notices of the Royal Astronomical Society, 362, 41

García Pérez A. E., et al., 2016, AJ, 151, 144

Gebek A., Matthee J., 2022, The Astrophysical Journal, 924, 73

Gilmore G., Wyse R. F. G., 1991a, ApJ, 367, L55

Gilmore G., Wyse R. F. G., 1991b, ApJ, 367, L55

Gilmore G., et al., 2012, The Messenger, 147, 25

Goater A., et al., 2024, Monthly Notices of the Royal Astronomical Society, 527, 2403

Gonzalez O. A., et al., 2011, Astronomy & Astrophysics, 530, A54

Gonzalez O. A., et al., 2020, The Messenger, 180, 18

Grand R. J. J., et al., 2017, Monthly Notices of the Royal Astronomical Society, 467, 179

Grand R. J. J., et al., 2018, Monthly Notices of the Royal Astronomical Society, 474, 3629

Gratton R. G., Carretta E., Matteucci F., Sneden C., 2000, Astronomy & Astrophysics, 358, 671

Gratton R. G., Carretta E., Bragaglia A., 2012, A&ARv, 20, 50

Graur O., Maoz D., 2013, Monthly Notices of the Royal Astronomical Society, 430, 1746

Gray E. I., et al., 2024, arXiv e-prints, p. arXiv:2405.19286

Grebel E. K., 2001, Astrophysics and Space Science Supplement, 277, 231

Griffith E. J., Sukhbold T., Weinberg D. H., Johnson J. A., Johnson J. W., Vincenzo F., 2021, arXiv e-prints, p. arXiv:2103.09837

Grisoni V., Spitoni E., Matteucci F., Recio-Blanco A., de Laverny P., Hayden M., Mikolaitis Ŝ., Worley C. C., 2017, Monthly Notices of the Royal Astronomical Society, 472, 3637

Gronow S., Collins C. E., Sim S. A., Röpke F. K., 2021a, Astronomy & Astrophysics, 649, A155

Gronow S., Côté B., Lach F., Seitenzahl I. R., Collins C. E., Sim S. A., Röpke F. K., 2021b, Astronomy & Astrophysics, 656, A94

Gunn J. E., et al., 2006, AJ, 131, 2332

Guth A. H., 1981, Phys. Rev. D, 23, 347

Häberle M., et al., 2024, arXiv e-prints, p. arXiv:2404.03722

Harris W. E., 2010, arXiv e-prints, p. arXiv:1012.3224

Hasselquist S., et al., 2017, The Astrophysical Journal, 845, 162

Hasselquist S., et al., 2021a, The Astrophysical Journal, 923, 172

Hasselquist S., et al., 2021b, The Astrophysical Journal, 923, 172

Hawkins K., Jofré P., Masseron T., Gilmore G., 2015, Monthly Notices of the Royal Astronomical Society, 453, 758

Hayden M. R., et al., 2015, The Astrophysical Journal, 808, 132

Haywood M., Di Matteo P., Lehnert M. D., Snaith O., Khoperskov S., Gómez A., 2018, The Astrophysical Journal, 863, 113

Helmi A., de Zeeuw P. T., 2000, Monthly Notices of the Royal Astronomical Society, 319, 657

Helmi A., White S. D. M., de Zeeuw P. T., Zhao H., 1999, Nature, 402, 53

Helmi A., Babusiaux C., Koppelman H. H., Massari D., Veljanoski J., Brown A. G. A., 2018, Nature, 563, 85

Hendricks B., Koch A., Lanfranchi G. A., Boeche C., Walker M., Johnson C. I., Peñarrubia J., Gilmore G., 2014, The Astrophysical Journal, 785, 102

Henon M., Heiles C., 1964, AJ, 69, 73

Herwig F., 2005, ARA&A, 43, 435

Hodge P. W., 1983, PASP, 95, 721

Hoffman M. D., Gelman A., et al., 2014, J. Mach. Learn. Res., 15, 1593

Hogg D. W., Bovy J., Lang D., 2010, arXiv e-prints, p. arXiv:1008.4686

Holtzman J. A., et al., 2018, AJ, 156, 125

Hopkins P. F., 2013, Monthly Notices of the Royal Astronomical Society, 428, 2840

Horta D., et al., 2021a, Monthly Notices of the Royal Astronomical Society, 500, 1385

Horta D., et al., 2021b, Monthly Notices of the Royal Astronomical Society, 500, 1385

Horta D., et al., 2021c, Monthly Notices of the Royal Astronomical Society, 500, 5462

Horta D., et al., 2021d, Monthly Notices of the Royal Astronomical Society, 500, 5462

Horta D., et al., 2023a, Monthly Notices of the Royal Astronomical Society, 520, 5671

Horta D., et al., 2023b, Monthly Notices of the Royal Astronomical Society, 520, 5671

Hubble E. P., 1936, Realm of the Nebulae. Yale University Press

Hughes M. E., Pfeffer J. L., Martig M., Reina-Campos M., Bastian N., Crain R. A., Kruijssen J. M. D., 2020, Monthly Notices of the Royal Astronomical Society, 491, 4012

Hunter J. D., 2007, Computing in Science & Engineering, 9, 90

Ibata R. A., Gilmore G., Irwin M. J., 1994a, Nature, 370, 194

Ibata R. A., Gilmore G., Irwin M. J., 1994b, Nature, 370, 194

Ibata R. A., Bellazzini M., Malhan K., Martin N., Bianchini P., 2019, Nature Astronomy, 3, 667

Iwamoto K., Brachwitz F., Nomoto K., Kishimoto N., Umeda H., Hix W. R., Thielemann F.-K., 1999, ApJS, 125, 439

Jin S., et al., 2023, Monthly Notices of the Royal Astronomical Society,

Johansson J., et al., 2013, Monthly Notices of the Royal Astronomical Society, 435, 1680

Johnson C. I., Pilachowski C. A., 2010, The Astrophysical Journal, 722, 1373

Johnson J. W., Weinberg D. H., 2020, Monthly Notices of the Royal Astronomical Society, 498, 1364

Johnson J. W., et al., 2021a, arXiv e-prints, p. arXiv:2103.09838

Johnson J. W., et al., 2021b, Monthly Notices of the Royal Astronomical Society, 508, 4484

Johnson J. W., et al., 2023, Monthly Notices of the Royal Astronomical Society, 526, 5084

Jönsson H., et al., 2020, AJ, 160, 120

Kacprzak G. G., et al., 2016, ApJ, 826, L11

Karakas A. I., 2010, Monthly Notices of the Royal Astronomical Society, 403, 1413

Karakas A. I., Lugaro M., 2016, The Astrophysical Journal, 825, 26

Katz H., Ricotti M., 2014, Monthly Notices of the Royal Astronomical Society, 444, 2377

Kawata D., Gibson B. K., 2003, Monthly Notices of the Royal Astronomical Society, 340, 908

Keller B. W., Wadsley J., Benincasa S. M., Couchman H. M. P., 2014, Monthly Notices of the Royal Astronomical Society, 442, 3013

Kennicutt Robert C. J., 1998a, ARA&A, 36, 189

Kennicutt Robert C. J., 1998b, The Astrophysical Journal, 498, 541

Khoperskov S., Haywood M., Snaith O., Di Matteo P., Lehnert M., Vasiliev E., Naroenkov S., Berczik P., 2021, Monthly Notices of the Royal Astronomical Society, 501, 5176

Kirby E. N., Cohen J. G., Guhathakurta P., Cheng L., Bullock J. S., Gallazzi A., 2013, The Astrophysical Journal, 779, 102

Kisku S., et al., 2021, Monthly Notices of the Royal Astronomical Society, 504, 1657

Kobayashi C., Umeda H., Nomoto K., Tominaga N., Ohkubo T., 2006a, The Astrophysical Journal, 653, 1145

Kobayashi C., Umeda H., Nomoto K., Tominaga N., Ohkubo T., 2006b, The Astrophysical Journal, 653, 1145

Kobayashi C., Bhattacharya S., Arnaboldi M., Gerhard O., 2023, ApJ, 956, L14

Kormendy J., Bender R., 1996, ApJ, 464, L119

Kormendy J., Kennicutt Robert C. J., 2004, ARA&A, 42, 603

Kormendy J., Fisher D. B., Cornell M. E., Bender R., 2009, ApJS, 182, 216

Kroupa P., 2001, Monthly Notices of the Royal Astronomical Society, 322, 231

Kruijssen J. M. D., 2015, Monthly Notices of the Royal Astronomical Society, 454, 1658

Kruijssen J. M. D., Pelupessy F. I., Lamers H. J. G. L. M., Portegies Zwart S. F., Bastian N., Icke V., 2012, Monthly Notices of the Royal Astronomical Society, 421, 1927

Kruijssen J. M. D., Pfeffer J. L., Crain R. A., Bastian N., 2019a, Monthly Notices of the Royal Astronomical Society, 486, 3134

Kruijssen J. M. D., Pfeffer J. L., Reina-Campos M., Crain R. A., Bastian N., 2019b, Monthly Notices of the Royal Astronomical Society, 486, 3180

Larson R. B., 1974, Monthly Notices of the Royal Astronomical Society, 169, 229

Larson R. B., 1976, Monthly Notices of the Royal Astronomical Society, 176, 31

Leaman R., VandenBerg D. A., Mendel J. T., 2013, Monthly Notices of the Royal Astronomical Society, 436, 122

Leroy A. K., Walter F., Brinks E., Bigiel F., de Blok W. J. G., Madore B., Thornley M. D., 2008, AJ, 136, 2782

Leroy A. K., et al., 2013, AJ, 146, 19

Li C., White S. D. M., 2009, Monthly Notices of the Royal Astronomical Society, 398, 2177

Lilly S. J., Le Fevre O., Hammer F., Crampton D., 1996, ApJ, 460, L1

Limberg G., Souza S. O., Pérez-Villegas A., Rossi S., Perottoni H. D., Santucci R. M., 2022, The Astrophysical Journal, 935, 109

Mac Low M.-M., Ferrara A., 1999, The Astrophysical Journal, 513, 142

Mackereth J. T., et al., 2017, Monthly Notices of the Royal Astronomical Society, 471, 3057

Mackereth J. T., Crain R. A., Schiavon R. P., Schaye J., Theuns T., Schaller M., 2018a, Monthly Notices of the Royal Astronomical Society, 477, 5072

Mackereth J. T., Crain R. A., Schiavon R. P., Schaye J., Theuns T., Schaller M., 2018b, Monthly Notices of the Royal Astronomical Society, 477, 5072

Mackereth J. T., et al., 2019a, Monthly Notices of the Royal Astronomical Society, 482, 3426

Mackereth J. T., et al., 2019b, Monthly Notices of the Royal Astronomical Society, 482, 3426

Madau P., Fragos T., 2017, The Astrophysical Journal, 840, 39

Madau P., Ferguson H. C., Dickinson M. E., Giavalisco M., Steidel C. C., Fruchter A., 1996, Monthly Notices of the Royal Astronomical Society, 283, 1388

Magnier E. A., et al., 2013, ApJS, 205, 20

Majewski S. R., Patterson R. J., Dinescu D. I., Johnson W. Y., Ostheimer J. C., Kunkel W. E., Palma C., 2000, in Noels A., Magain P., Caro D., Jehin E., Parmentier G., Thoul A. A., eds, Liege International Astrophysical Colloquia Vol. 35, Liege International Astrophysical Colloquia. p. 619 (arXiv:astro-ph/9910278), doi:10.48550/arXiv.astro-ph/9910278

Majewski S. R., et al., 2017a, AJ, 154, 94

Majewski S. R., et al., 2017b, AJ, 154, 94

Mannucci F., Cresci G., Maiolino R., Marconi A., Gnerucci A., 2010, Monthly Notices of the Royal Astronomical Society, 408, 2115

Maoz D., Graur O., 2017, The Astrophysical Journal, 848, 25

Marcelina Gountanis N., Weinberg D. H., Beverage A. G., Sandford N. R., Conroy C., Kriek M., 2024, arXiv e-prints, p. arXiv:2407.07971

Marigo P., 2001, Astronomy & Astrophysics, 370, 194

Marino A. F., et al., 2011, The Astrophysical Journal, 731, 64

Marino A. F., et al., 2019, Monthly Notices of the Royal Astronomical Society, 487, 3815

Martell S. L., et al., 2017, Monthly Notices of the Royal Astronomical Society, 465, 3203

Mason A. C., Crain R. A., Schiavon R. P., Weinberg D. H., Pfeffer J., Schaye J., Schaller M., Theuns T., 2023, arXiv e-prints, p. arXiv:2311.00041

Massari D., Koppelman H. H., Helmi A., 2019, Astronomy & Astrophysics, 630, L4

Masseron T., et al., 2019, Astronomy & Astrophysics, 622, A191

Mateo M. L., 1998, ARA&A, 36, 435

Matteucci F., Brocato E., 1990, The Astrophysical Journal, 365, 539

Matteucci F., Francois P., 1989, Monthly Notices of the Royal Astronomical Society, 239, 885

Matteucci F., Spitoni E., Recchi S., Valiante R., 2009, Astronomy & Astrophysics, 501, 531

Matthee J., Schaye J., Crain R. A., Schaller M., Bower R., Theuns T., 2017, Monthly Notices of the Royal Astronomical Society, 465, 2381

McAlpine S., et al., 2016, Astronomy and Computing, 15, 72

McConnachie A. W., 2012, AJ, 144, 4

McKee C. F., Ostriker J. P., 1977, The Astrophysical Journal, 218, 148

McMillan P. J., 2017, Monthly Notices of the Royal Astronomical Society, 465, 76

McWilliam A., 1997, ARA&A, 35, 503

Mészáros S., et al., 2015, AJ, 149, 153

Mészáros S., et al., 2020, Monthly Notices of the Royal Astronomical Society, 492, 1641

Mészáros S., et al., 2021a, Monthly Notices of the Royal Astronomical Society, 505, 1645

Mészáros S., et al., 2021b, Monthly Notices of the Royal Astronomical Society, 505, 1645

Milone A. P., et al., 2017a, Monthly Notices of the Royal Astronomical Society, 464, 3636

Milone A. P., et al., 2017b, Monthly Notices of the Royal Astronomical Society, 469, 800

Mitchell P. D., Schaye J., Bower R. G., Crain R. A., 2020, Monthly Notices of the Royal Astronomical Society, 494, 3971

Mo H., van den Bosch F. C., White S., 2010, Galaxy Formation and Evolution. Cambridge University Press

Muratov A. L., Gnedin O. Y., 2010, The Astrophysical Journal, 718, 1266

Myeong G. C., Vasiliev E., Iorio G., Evans N. W., Belokurov V., 2019, Monthly Notices of the Royal Astronomical Society, 488, 1235

Myeong G. C., Belokurov V., Aguado D. S., Evans N. W., Caldwell N., Bradley J., 2022, The Astrophysical Journal, 938, 21

Nataf D. M., et al., 2019, AJ, 158, 14

Nelson D., et al., 2018, Monthly Notices of the Royal Astronomical Society, 475, 624

Neumayer N., Seth A., Böker T., 2020, A&ARv, 28, 4

Newton O., Cautun M., Jenkins A., Frenk C. S., Helly J. C., 2018, Monthly Notices of the Royal Astronomical Society, 479, 2853

Nidever D. L., et al., 2014, The Astrophysical Journal, 796, 38

Nidever D. L., et al., 2015, AJ, 150, 173

Nidever D. L., et al., 2020a, The Astrophysical Journal, 895, 88

Nidever D. L., et al., 2020b, The Astrophysical Journal, 895, 88

Nidever D. L., et al., 2021, AJ, 161, 74

Nidever D., et al., 2024, in American Astronomical Society Meeting Abstracts. p. 428.05

Nissen P. E., Schuster W. J., 2010, Astronomy & Astrophysics, 511, L10

Nissen P. E., Schuster W. J., 2011, Astronomy & Astrophysics, 530, A15

Nissen P. E., Gustafsson B., Edvardsson B., Gilmore G., 1994, Astronomy & Astrophysics, 285, 440

Nitschai M. S., et al., 2023, The Astrophysical Journal, 958, 8

Nitschai M. S., et al., 2024, arXiv e-prints, p. arXiv:2406.01688

Nomoto K., Kobayashi C., Tominaga N., 2013, ARA&A, 51, 457

Norris J. E., Da Costa G. S., 1995, ApJ, 441, L81

Ollongren A., 1965, ARA&A, 3, 113

Orkney M. D. A., et al., 2021, Monthly Notices of the Royal Astronomical Society, 504, 3509

Orkney M. D. A., et al., 2022, Monthly Notices of the Royal Astronomical Society, 515, 185

Orkney M. D. A., Taylor E., Read J. I., Rey M. P., Pontzen A., Agertz O., Kim S. Y., Delorme M., 2023, Monthly Notices of the Royal Astronomical Society, 525, 3516

Pagel B. E. J., 2009, Nucleosynthesis and Chemical Evolution of Galaxies. Cambridge University Press

Pancino E., Ferraro F. R., Bellazzini M., Piotto G., Zoccali M., 2000, ApJ, 534, L83

Pearson W. J., et al., 2019, Astronomy & Astrophysics, 631, A51

Peebles P. J. E., 1984, The Astrophysical Journal, 277, 470

Perez F., Granger B. E., 2007, Computing in Science & Engineering, 9, 21

Pfeffer J., Baumgardt H., 2013, Monthly Notices of the Royal Astronomical Society, 433, 1997

Pfeffer J., Kruijssen J. M. D., Crain R. A., Bastian N., 2018, Monthly Notices of the Royal Astronomical Society, 475, 4309

Philcox O. H. E., Rybizki J., 2019, The Astrophysical Journal, 887, 9

Phillips S. G., et al., 2022, Monthly Notices of the Royal Astronomical Society, 510, 3727

Pillepich A., et al., 2018, Monthly Notices of the Royal Astronomical Society, 473, 4077

Planck Collaboration et al., 2014, Astronomy & Astrophysics, 571, A1

Planck Collaboration et al., 2016, Astronomy & Astrophysics, 594, A13

Planck Collaboration et al., 2020a, Astronomy & Astrophysics, 641, A6

Planck Collaboration et al., 2020b, Astronomy & Astrophysics, 641, A6

Pontzen A., Rey M. P., Cadiou C., Agertz O., Teyssier R., Read J., Orkney M. D. A., 2021, Monthly Notices of the Royal Astronomical Society, 501, 1755

Portinari L., Chiosi C., Bressan A., 1998a, Astronomy & Astrophysics, 334, 505

Portinari L., Chiosi C., Bressan A., 1998b, Astronomy & Astrophysics, 334, 505

Prantzos N., Aubert O., 1995, Astronomy & Astrophysics, 302, 69

Prgomet M., Rey M. P., Andersson E. P., Segovia Otero A., Agertz O., Renaud F., Pontzen A., Read J. I., 2022, Monthly Notices of the Royal Astronomical Society, 513, 2326

Price D. J., 2010, Monthly Notices of the Royal Astronomical Society, 401, 1475

Prochaska J. X., Naumov S. O., Carney B. W., McWilliam A., Wolfe A. M., 2000, AJ, 120, 2513

Qu Y., et al., 2017, Monthly Notices of the Royal Astronomical Society, 464, 1659

Randich S., Gilmore G., Gaia-ESO Consortium 2013, The Messenger, 154, 47

Renzini A., et al., 2015, Monthly Notices of the Royal Astronomical Society, 454, 4197

Rey M. P., Pontzen A., Agertz O., Orkney M. D. A., Read J. I., Saintonge A., Pedersen C., 2019, ApJ, 886, L3

Rey M. P., Pontzen A., Agertz O., Orkney M. D. A., Read J. I., Rosdahl J., 2020, Monthly Notices of the Royal Astronomical Society, 497, 1508

Rey M. P., Pontzen A., Agertz O., Orkney M. D. A., Read J. I., Saintonge A., Kim S. Y., Das P., 2022, Monthly Notices of the Royal Astronomical Society, 511, 5672

Rey M. P., et al., 2024, Monthly Notices of the Royal Astronomical Society, 529, 2379

Rix H.-W., et al., 2022, The Astrophysical Journal, 941, 45

Rosas-Guevara Y. M., et al., 2015, Monthly Notices of the Royal Astronomical Society, 454, 1038

Salim S., Lee J. C., Ly C., Brinchmann J., Davé R., Dickinson M., Salzer J. J., Charlot S., 2014, The Astrophysical Journal, 797, 126

Salpeter E. E., 1955, The Astrophysical Journal, 121, 161

Salvatier J., Wiecki T. V., Fonnesbeck C., 2016, PeerJ Computer Science, 2, e55

Samland M., Hensler G., Theis C., 1997, The Astrophysical Journal, 476, 544

Schaye J., 2004, The Astrophysical Journal, 609, 667

Schaye J., Dalla Vecchia C., 2008, Monthly Notices of the Royal Astronomical Society, 383, 1210

Schaye J., et al., 2015, Monthly Notices of the Royal Astronomical Society, 446, 521

Schaye J., et al., 2023, Monthly Notices of the Royal Astronomical Society, 526, 4978

Schechter P., 1976, The Astrophysical Journal, 203, 297

Schiavon R. P., 2007, ApJS, 171, 146

Schiavon R. P., et al., 2017a, Monthly Notices of the Royal Astronomical Society, 465, 501

Schiavon R. P., et al., 2017b, Monthly Notices of the Royal Astronomical Society, 466, 1010

Schiavon R. P., Mackereth J. T., Pfeffer J., Crain R. A., Bovy J., 2020, in Bragaglia A., Davies M., Sills A., Vesperini E., eds, Star Clusters: From the Milky Way to the Early Universe. 351. pp 170–173 (arXiv:2002.08380), doi:10.1017/S1743921319007889

Schiavon R. P., et al., 2024, Monthly Notices of the Royal Astronomical Society, 528, 1393

Schmidt M., 1959, The Astrophysical Journal, 129, 243

Schmidt M., 1963, The Astrophysical Journal, 137, 758

Schönrich R., Binney J., 2009a, Monthly Notices of the Royal Astronomical Society, 396, 203

Schönrich R., Binney J., 2009b, Monthly Notices of the Royal Astronomical Society, 399, 1145

Schönrich R., Binney J., Dehnen W., 2010, Monthly Notices of the Royal Astronomical Society, 403, 1829

Seabold S., Perktold J., 2010, in 9th Python in Science Conference.

Searle L., Sargent W. L. W., 1972, The Astrophysical Journal, 173, 25

Searle L., Zinn R., 1978a, The Astrophysical Journal, 225, 357

Searle L., Zinn R., 1978b, The Astrophysical Journal, 225, 357

Segers M. C., Schaye J., Bower R. G., Crain R. A., Schaller M., Theuns T., 2016, Monthly Notices of the Royal Astronomical Society, 461, L102

Seitenzahl I. R., et al., 2013, Monthly Notices of the Royal Astronomical Society, 429, 1156

Simpson J. D., et al., 2020, Monthly Notices of the Royal Astronomical Society, 491, 3374

Skillman E. D., et al., 2017, The Astrophysical Journal, 837, 102

Skrutskie M. F., et al., 2006, AJ, 131, 1163

Skúladóttir Á., et al., 2023, The Messenger, 190, 19

Smith R. J., 2020, ARA&A, 58, 577

Sollima A., Ferraro F. R., Pancino E., Bellazzini M., 2005, Monthly Notices of the Royal Astronomical Society, 357, 265

Springel V., 2005, Monthly Notices of the Royal Astronomical Society, 364, 1105

Springel V., White S. D. M., Tormen G., Kauffmann G., 2001, Monthly Notices of the Royal Astronomical Society, 328, 726

Springel V., et al., 2018, Monthly Notices of the Royal Astronomical Society, 475, 676

Steinmetz M., et al., 2006, AJ, 132, 1645

Sun F., et al., 2023, The Astrophysical Journal, 953, 53

Tacconi L. J., et al., 2018, The Astrophysical Journal, 853, 179

Talbot Raymond J. J., Arnett W. D., 1971, The Astrophysical Journal, 170, 409

Thielemann F. K., et al., 2003, in Hillebrandt W., Leibundgut B., eds, From Twilight to Highlight: The Physics of Supernovae. p. 331, doi:10.1007/10828549_46

Thomas D., Greggio L., Bender R., 1998, Monthly Notices of the Royal Astronomical Society, 296, 119

Tinsley B. M., 1979, The Astrophysical Journal, 229, 1046

Tinsley B. M., Larson R. B., 1978, The Astrophysical Journal, 221, 554

Tissera P. B., Rosas-Guevara Y., Bower R. G., Crain R. A., del P Lagos C., Schaller M., Schaye J., Theuns T., 2019, Monthly Notices of the Royal Astronomical Society, 482, 2208

Tolstoy E., Hill V., Tosi M., 2009, ARA&A, 47, 371

Tosi M., Greggio L., Marconi G., Focardi P., 1991, AJ, 102, 951

Trager S. C., Faber S. M., Worthey G., González J. J., 2000, AJ, 120, 165

Tremonti C. A., et al., 2004, The Astrophysical Journal, 613, 898

Trenti M., Padoan P., Jimenez R., 2015, ApJ, 808, L35

Tully R. B., Fisher J. R., 1977, Astronomy & Astrophysics, 54, 661

Usher C., Brodie J. P., Forbes D. A., Romanowsky A. J., Strader J., Pfeffer J., Bastian N., 2019, Monthly Notices of the Royal Astronomical Society, 490, 491

Vargas L. C., Geha M., Kirby E. N., Simon J. D., 2013, The Astrophysical Journal, 767, 134

Vargas L. C., Geha M. C., Tollerud E. J., 2014, The Astrophysical Journal, 790, 73

Vasini A., Matteucci F., Spitoni E., Siegert T., 2023, Monthly Notices of the Royal Astronomical Society, 523, 1153

Vasini A., Spitoni E., Matteucci F., 2024, Astronomy & Astrophysics, 683, A121

Venn K. A., Irwin M., Shetrone M. D., Tout C. A., Hill V., Tolstoy E., 2004, AJ, 128, 1177

Ventura P., Di Criscienzo M., Carini R., D'Antona F., 2013, Monthly Notices of the Royal Astronomical Society, 431, 3642

Villanova S., Geisler D., Gratton R. G., Cassisi S., 2014, The Astrophysical Journal, 791, 107

Virtanen P., et al., 2020, Nature Methods, 17, 261

Wallerstein G., 1962, ApJS, 6, 407

Weinberg D. H., Andrews B. H., Freudenburg J., 2017a, The Astrophysical Journal, 837, 183

Weinberg D. H., Andrews B. H., Freudenburg J., 2017b, The Astrophysical Journal, 837, 183

Weinberg D. H., et al., 2019, The Astrophysical Journal, 874, 102

Weinberg D. H., et al., 2022, ApJS, 260, 32

Weinberger R., et al., 2017, Monthly Notices of the Royal Astronomical Society, 465, 3291

Weisz D. R., et al., 2011, The Astrophysical Journal, 739, 5

Weisz D. R., Dolphin A. E., Skillman E. D., Holtzman J., Gilbert K. M., Dalcanton J. J., Williams B. F., 2014, The Astrophysical Journal, 789, 147

White S. D. M., Rees M. J., 1978, Monthly Notices of the Royal Astronomical Society, 183, 341

Wiersma R. P. C., Schaye J., Smith B. D., 2009a, Monthly Notices of the Royal Astronomical Society, 393, 99

Wiersma R. P. C., Schaye J., Theuns T., Dalla Vecchia C., Tornatore L., 2009b, Monthly Notices of the Royal Astronomical Society, 399, 574

Willman B., Strader J., 2012, AJ, 144, 76

Wilson J. C., et al., 2019, PASP, 131, 055001

Woosley S. E., Weaver T. A., 1994, The Astrophysical Journal, 423, 371

Woosley S. E., Weaver T. A., 1995, ApJS, 101, 181

Worthey G., Faber S. M., Gonzalez J. J., 1992, The Astrophysical Journal, 398, 69

Wyse R. F. G., Silk J., 1989, The Astrophysical Journal, 339, 700

Yanny B., et al., 2009, AJ, 137, 4377

de Boer T. J. L., Belokurov V., Beers T. C., Lee Y. S., 2014, Monthly Notices of the Royal Astronomical Society, 443, 658

de Jong R. S., et al., 2019, The Messenger, 175, 3

de Vaucouleurs G., 1948, Annales d'Astrophysique, 11, 247

van Dokkum P. G., Conroy C., 2010, Nature, 468, 940

van den Bergh S., 1962, AJ, 67, 486

van der Walt S., Colbert S. C., Varoquaux G., 2011, Computing in Science & Engineering, 13, 22